EXPERIMENTAL AND NUMERICAL STUDY OF DUAL-CHAMBER THERMOSYPHON

A Thesis
Presented to
The Academic Faculty

by

Aniruddha Pal

In Partial Fulfillment
of the Requirements for the Degree
Doctor of Philosophy in the
G. W. Woodruff School of Mechanical Engineering

Georgia Institute of Technology
August 2007

EXPERIMENTAL AND NUMERICAL STUDY OF DUAL-CHAMBER THERMOSYPHON

Approved by:

Professor Yogendra Joshi,
Committee Chair
G. W. Woodruff School of Mechanical Engineering
Georgia Institute of Technology

Professor Larry J. Forney
School of Chemical and Biomolecular Engineering
Georgia Institute of Technology

Professor Samuel V. Shelton
G. W. Woodruff School of Mechanical Engineering
Georgia Institute of Technology

Professor Sushil Bhavnani
Department of Mechanical Engineering
Auburn University

Professor Seyed Mostafa Ghiaasiaan
G. W. Woodruff School of Mechanical Engineering
Georgia Institute of Technology

Date Approved: 16 May 2007

To my Parents, my brother and my wife, who have given me constant love and support to pursue my dreams.

ACKNOWLEDGEMENTS

This thesis is the end of a long journey for me towards getting my Ph.D. degree in Mechanical Engineering. The journey has been made worthwhile due to the help and support of many individuals, who have to put up with me during all these years.

First of all, I would like to express my sincere gratitude to Dr. Yogendra Joshi, who has been a constant source of inspiration and encouragement throughout my career as a graduate student at University of Maryland and at Georgia Institute of Technology. I greatly appreciate his participation in our long discussions on various aspects of my research, his advice towards my choices in academic and professional career, and the opportunities he offered to present my work at international conferences and to work with the advanced facilities at the Microelectronics and Emerging Technologies Thermal Laboratory. He continually stimulated my critical thinking ability and greatly helped in improving my scientific writing and presentation skills.

I would like to thank the members of my dissertation committee, Dr. Seyed Mostafa Ghiaasiaan, Dr. Samuel V. Shelton, Dr. Larry J. Forney and Dr. Sushil Bhavnani, who have given their valuable time to review my research proposal and the final dissertation, and given their valuable suggestions towards making my research work more valuable to the engineering and scientific community.

My sincere thanks go to Monem Beitelmal and Dr. Chandrakant Patel of Hewlett Packard, who have worked with us towards making the thermosyphon prototype a reality. Thanks also goes to Todd Wenger of Thermacore International Inc. (now Modine Manufacturing Company), for helping us in fabricating the prototype.

My special thanks goes to Ms. Regina Neequaye, whose prompt processing of purchase requests and smooth handling of administrative affairs greatly helped in

accelerating my work and keeping the time commitments.

I would also like to thank the Packaging Research Center (PRC) at Georgia Tech, for providing financial support during my research and for providing me opportunities to interact with industrial representatives through the research work being done at the PRC.

I extend many thanks to my colleagues and friends for keeping the atmosphere in the laboratory and office conducive for critical thinking and stimulating discussions, as well as helping in relieving work-related stresses and rejuvenating our minds. Special thanks goes to Camil-Daniel Ghiu, Xiaojin Wei, Sunil Murthy, Siva Gurrum, Shivesh Suman, Robert Kaczorowski, Robert Wadell, Scott Williams, Jeff Welsh, Nathan Rolander, Jeff Rambo, Adya Ali, Ashish Sinha, Dr. David Gerlach, Dr. Stephane Launay and Qihong Nie for being such nice colleagues and helping me in many aspects during my stay at Georgia Tech. I couldn't have asked for a better team.

My special thanks goes to my parents and my brother, who have been my greatest source of inspiration. Without their constant encouragement, I wouldn't have reached this far. I owe my thanks to my family-in-law, who have also given me encouragement and support in my educational endeavors. Finally, my loving and heartfelt thanks goes to my dear wife, Suchismita, for bearing with me all these years, especially on all those holidays and weekends, when I was working on my thesis and for giving me all the support, encouragement and companionship.

TABLE OF CONTENTS

LIST OF TABLES

LIST OF FIGURES

LIST OF SYMBOLS OR ABBREVIATIONS

A	Area of boiling surface, m^2.
A_s	Heater surface area, m^2.
A_{ch}	Area of the channel, m^2.
$A_{lc,j}$	Area of the j^{th} corner liquid zone, j = 2 and 4, m^2.
$A_{lf,j}$	Area of the j^{th} liquid film zone, j = 1, 3 and 5, m^2.
A_v	Area of the vapor core, m^2.
D_h	Hydraulic diameter of the channel, m.
$D_{h,v}$	Hydraulic diameter of the vapor core, m.
$D_{lc,k}$	Hydraulic diameter of the k^{th} corner liquid zone (k = 2, 4), m.
f_l	Friction coefficient of the liquid flow.
f_v	Friction coefficient of the vapor flow.
g	Acceleration due to gravity, m/s^2.
$\bar{h}_{lf}(z)$	Average heat transfer coefficient for the thin film zone, $W/m^2 - K$.
$h(z)$	Cross-sectional average heat transfer coefficient along Z axis, $W/m^2 - K$.
$h(z)$	Average heat transfer coefficient of the channel along the axial direction, $W/m^2 - K$.
$h_{ave,ex}$	Average heat transfer coefficient of the exposed surfaces of enhanced structure, $W/m^2 - K$.
h_{fg}	Latent heat of vaporization, J/kg.
h_{lc}	Mean heat transfer coefficient of the corner zone, $W/m^2 - K$.
$h_{lf}(y, z)$	Local heat transfer coefficient of the liquid film zone, $W/m^2 - K$.
H	Height, m.
k_l	Thermal conductivity of the liquid, $W/m - K$.
L_j	Length of the j^{th} thin film zone (j = 1, 3, 5), m.
$\dot{m}''_{con}$	Mass flow rate due to condensation, $kg/m^2 - s$.
$\dot{m}''_{hor}$	Mass flow rate from the horizontal liquid film zone, $kg/m^2 - s$.

$\dot{m}''_{lf}$	Mass flow rate from the liquid film zones, $kg/m^2 - s$.
$\dot{m}''_{ver}$	Mass flow rate from the vertical liquid film zone, $kg/m^2 - s$.
$\dot{m}_i$	Mass flow rate at the liquid-vapor interface , $kg/m^2 - s$.
$\dot{m}_v$	Mass flow rate of the vapor core, kg/s.
p_c	Capillary pressure, Pa.
p_v	Pressure in the vapor core, Pa.
p_{lc}	Pressure in the corner liquid zone, Pa.
p_{lf}	Pressure in the liquid film, Pa.
p_{sat}	Saturation pressure, Pa.
P_i	Perimeter at the liquid-vapor interface, m.
P_v	Perimeter of the vapor core, m.
P_{ch}	Perimeter of the channel, m.
$P_{lc,k}$	Wetted perimeter of the k^{th} corner liquid zone (k = 2, 4), m.
P_{lw}	Wetted perimeter at the liquid-wall interface, m.
Pr_l	Prandtl number of the liquid.
Q'	Input power to the system/heat dissipation, W.
q''	Boiling surface heat flux, W/m^2.
$q''_c(y,z)$	Local condensation heat flux at liquid-vapor interface, W/m^2.
R	Resistance, Ω.
R_g	Universal gas constant, $J/kg - K$.
R_t	Thermal resistance, $^oC/W$.
$r_{c,i}$	Radius of curvature of the i^{th} corner zone (i = 2, 4), m.
Re_v	Reynolds number of the vapor core flow.
Re_{ls}	Superficial Reynolds number of the condensate flow.
T_{lf}	Temperature in the liquid film, ^oC.
T_{li}	Local interfacial liquid temperature, ^oC.
T_{sat}	Saturation temperature, ^oC.

T_s	Surface temperature, ^oC.
T_{vi}	Local interfacial vapor temperature, ^oC.
T_w	Wall temperature, ^oC.
u	Velocity of the liquid along x axis, m/s.
v	Velocity of the liquid along y axis, m/s.
V	Voltage, V.
w	Velocity of the liquid along z axis, m/s.
$\bar{w}$	Mean velocity of the vapor along z axis, m/s.
$\bar{w}_{lc}$	Mean velocity of the corner liquid zone along z axis, m/s.
$\bar{w}_{ls}$	Mean superficial velocity of the liquid, m/s.
W	Width of channel, m.
X	X axis of the fixed XYZ co-ordinate.
Y	Y axis of the fixed XYZ co-ordinate.
β	Dispersion coefficient.
χ	Vapor quality.
Δp_{lv}	Pressure drop of the two-phase flow, Pa.
Δp_l	Pressure drop of the liquid flowing alone in a channel, Pa.
δ	Thickness of the condensate in the thin film zones, m.
κ	Curvature of the liquid-vapor interface, $1/m$.
μ_l	Coefficient of dynamic viscosity, $N - s/m^2$.
ν	Accommodation coefficient.
$\phi_{l,vt}$	Two-phase multiplier.
ρ_l	Density of the liquid, kg/m^3.
ρ_v	Density of the vapor, kg/m^3.
σ_l	Surface tension of the liquid, N/m.
τ_i	Interfacial shear stress, N/m^2.
τ_{lw}	Shear stress at the liquid-wall interface, N/m^2.

SUMMARY

An experimental investigation was conducted to study the thermal performance of boiling of water in a compact two-phase dual chamber thermosyphon for localized high heat flux applications. The thermosyphon had a three-dimensional porous boiling structure integrated in the evaporator, where each layer of the structure was of dimensions 12.7 × 12.7 × 1 mm (length × breadth × thickness). The effects of sub-atmospheric pressures on thermal performance were investigated at 9.7 kPa, 15 kPa and 21 kPa. Sub-atmospheric pressure boiling of water achieved heat fluxes in excess of 100 W/cm^2 with negligible incipience superheat, while keeping boiling surface temperatures below 85 ^{o}C. Reduced pressures also resulted in reduction of heat transfer coefficient with decrease in saturation pressure. Four different geometries of the structure were used, each having 1, 2, 4 and 6 layers respectively. The boiling curves from the enhancement structures were compared to sub-atmospheric pressure boiling from plain surface. The boiling enhancement structure showed considerable heat transfer enhancement compared to boiling from plain surface and also increased the critical heat flux (CHF). Increased height of the structure decreased the heat transfer coefficient and suggested the existence of an optimum structure height for a particular saturation pressure. A numerical simulation was performed to compare the heat transfer from the structures with respect to experimental results. The surface heat fluxes obtained from the numerical model matched closely with the experimental results. A parametric study was conducted to understand the effect of evaporator liquid-fill level on thermal performance. A reduction in liquid level of water increased the CHF for boiling with plain surfaces. In case of enhanced structures, the results suggested the existence of an optimum liquid level for maximum heat transfer. The

optimum liquid level increased with increase in the height of the enhanced structure.

A numerical model has been developed to study condensation of water in horizontal rectangular microchannels. The model incorporated surface tension, axial pressure gradient, liquid film curvature, liquid film thermal resistance, gravity and interfacial shear stress, and implemented successive solution of mass, momentum and energy balance equations for both liquid and vapor phases. The study is done for rectangular channels of sidewalls varying between 100-500 μm (corresponding to D_h = 150-375 μm) and mass flow rates of 70-110 kg/m^2s with a fixed wall temperature. The results showed that significantly higher heat transfer coefficient can be achieved from a rectangular microchannel compared to a circular channel of similar hydraulic diameter. Increasing the inlet mass flow rate leads to higher heat transfer coefficient, while increasing the inlet temperature difference between wall and vapor also leads to a thicker film and a gradually decreasing heat transfer coefficient. Increasing the channel dimensions leads to higher heat transfer coefficient, with a reduction in the vapor pressure drop along the axial direction of the channel.

The unique contributions of the study are: extending the knowledge base and contributing unique results on the effects of sub-atmospheric pressures, enhancement structure geometry and liquid-fill volume on the thermal performance of thermosyphons with water as the working fluid and development of a unique model for condensation of water in rectangular microchannels and identifying the system parameters that affects the flow and thermal performance during condensation.

CHAPTER I

INTRODUCTION

Micro-electronic parts are the heart of most of the electronic systems which are used in our daily life. The current trend in micro-electronic part design is to increase the level of integration, miniaturize the microprocessor size, increase the clock speed and thus provide low cost solutions. The design topology has increased the functionality of the devices significantly, however, numerous issues have also appeared regarding electrical performance, interconnect reliability and thermal performance. These issues need to be addressed for designing a reliable and functionally efficient final product.

The continuous advancement in design for higher performance microelectronic chip is responsible for generating higher transistor switching speeds and reduction in the chip size, which has resulted in an increase in total power dissipation as well as the the heat flux from the silicon device, typically in the range of 100 W/cm^2. According to the predictions of the *International Technology Roadmap for Semiconductors, 2006* [1], the power dissipation from chips for high performance desktop applications will cross 190 W by 2007 and is expected to reach 200 W in the next five years. The predictions follow a general trend observed over the years - with increase in the performance of chips, there has been a steady escalation in the power dissipation, as seen in Figure 1. This growing heat dissipation from the chips raises various design issues, as chip performance is dependent on the operating temperature. It is well-known that with reduction in chip operating temperature, the reliability of the chip increases exponentially. Apart from that, lower operating temperatures induces higher switching speeds in the semiconductor gates and also is responsible for lower leakage power. So a lower thermal budget will provide better yield in reliability and

performance. As a result, design of thermal solutions capable of dissipating large surface heat fluxes and volumetric heat generation rates from electronic parts has become an important issue. Novel ways of heat dissipation are required which can keep chips well below the acceptable temperature, typically in the range 85 ^{o}C.

Thermal management of electronics can be achieved by passive or active means, by employing either air or liquid coolants. Air cooling through forced convection by fans has been the most popular way of thermal management for electronics applications. Fans are generally attached to the electronic devices and their popularity is due to their cost, reliability, efficiency and ease of implementation. However, air cooling has the inherent limitations of noise, bulky size and inefficient cooling performance. Liquid cooling on the other hand is a very attractive alternative solution for heat dissipation from electronics and it achieves very high heat transfer coefficients. Liquid cooling can be achieved through direct or indirect contact of liquid with the electronic equipments, either through single-phase or two-phase heat transfer. In direct-contact liquid cooling, the electronic device is immersed in the working fluid and as such, the cooling system is designed to be integral with the device. On the other hand, in indirect-contact liquid cooling, heat transfer takes place by conduction (through an interface) from the electronics to the working fluid and this process introduces higher thermal resistance to heat flow between electronics and working fluid. However, proper choice of highly conducting working fluid and use of thermally-conductive interface material in the electronics-cooling system junction may mitigate the thermal resistance. On the other hand, choice of two-phase heat transfer over single-phase can also be beneficial in achieving very high heat transfer coefficients, typically in the range of 10^6 W/m^2, as the latent heat component is responsible for bulk of the heat transfer during phase change.

Clearly, there is a need to design highly efficient and compact thermal solutions to address the issues of high heat dissipation, size, placement and reliability with the

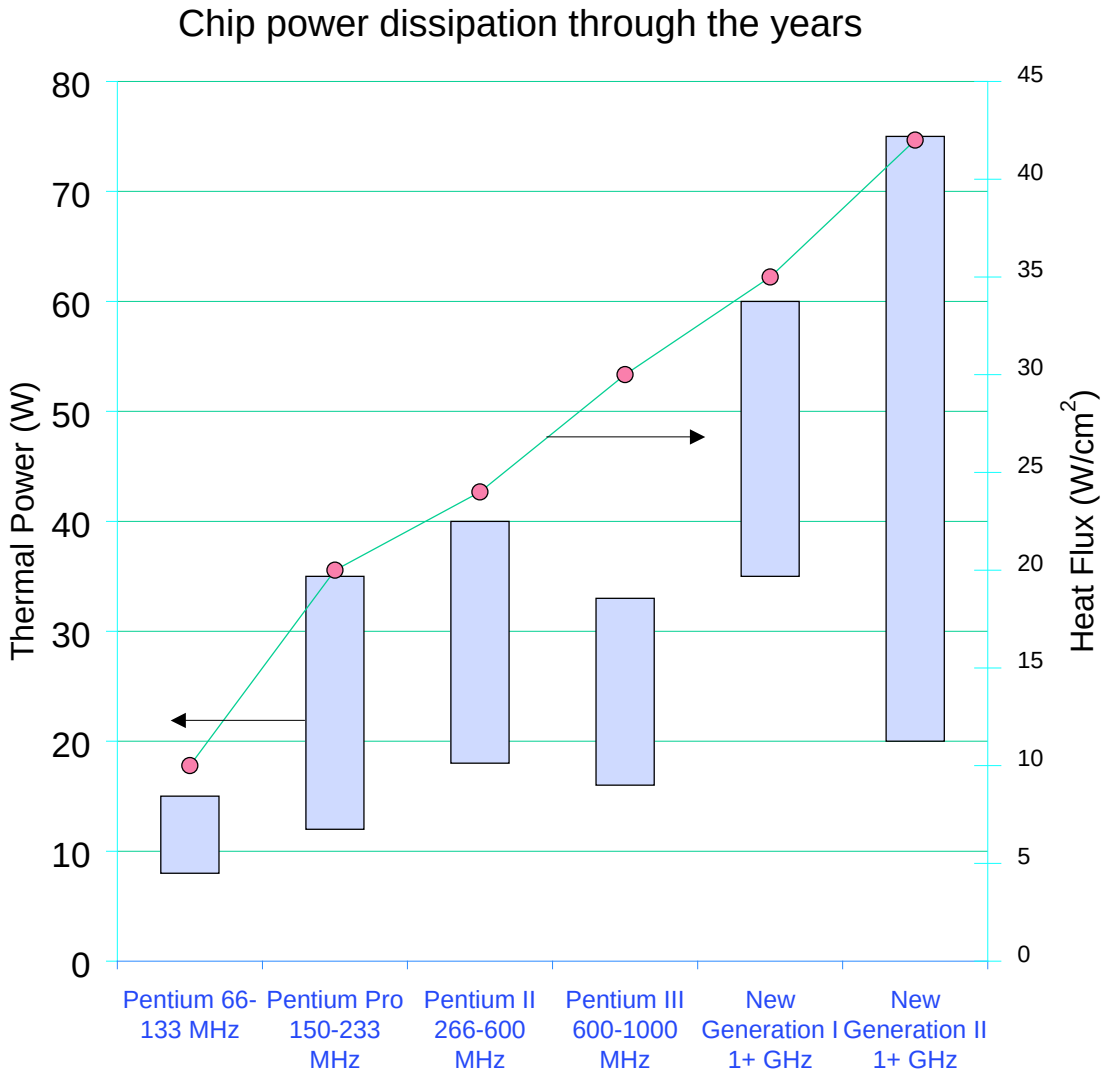

Figure 1: Chip power dissipation through the years (Source: Intel Quarterly Journal Q3, 2000 [2])

exciting prospect of using two-phase heat transfer.

1.1 Motivation for the Current Study

As we have seen in the previous section, the increase in the heat dissipation from newer generation of electronics and the decrease in the overall system size is making thermal management of electronics an important issue in the overall design of the system. Highly efficient and compact thermal solutions will be needed to address the issues of heat dissipation, size, placement and reliability. In this respect, a two-phase liquid cooling system provides an exciting thermal solution through combination of the various categories described in the previous chapter.

A thermosyphon is a device, which implements two-phase heat transfer through successive evaporation and condensation of the working fluid in a closed loop system. Thermosyphon consists of two separate chambers - an evaporator and a condenser connected to each other in a closed loop. The two most common configurations of thermosyphons are single chamber and dual chamber thermosyphons. In the single chamber configuration, the direction of vapor flow is opposite to the direction of condensate flow, which may create a dry-out situation in the evaporator at high heat fluxes (¿ 30 W/cm^2). As a result, single chamber configurations are not suitable for high heat flux applications. The dual chamber thermosyphon, as shown in Figure 2, has the inherent advantage of handling liquid and vapor in two separate chambers and thus addresses the disadvantageous issue of the single chamber thermosyphon. Moreover, there is flexibility in the placement of the two chambers, which helps in designing a configuration for tackling space constraints in modern compact electronic systems. The evaporator is placed in direct contact with the heat source. The absorbed heat from the source helps in vaporizing the working fluid. An internal pressure head, generated due to difference in density of liquid and vapor (the condenser is placed above the evaporator in this configuration) is

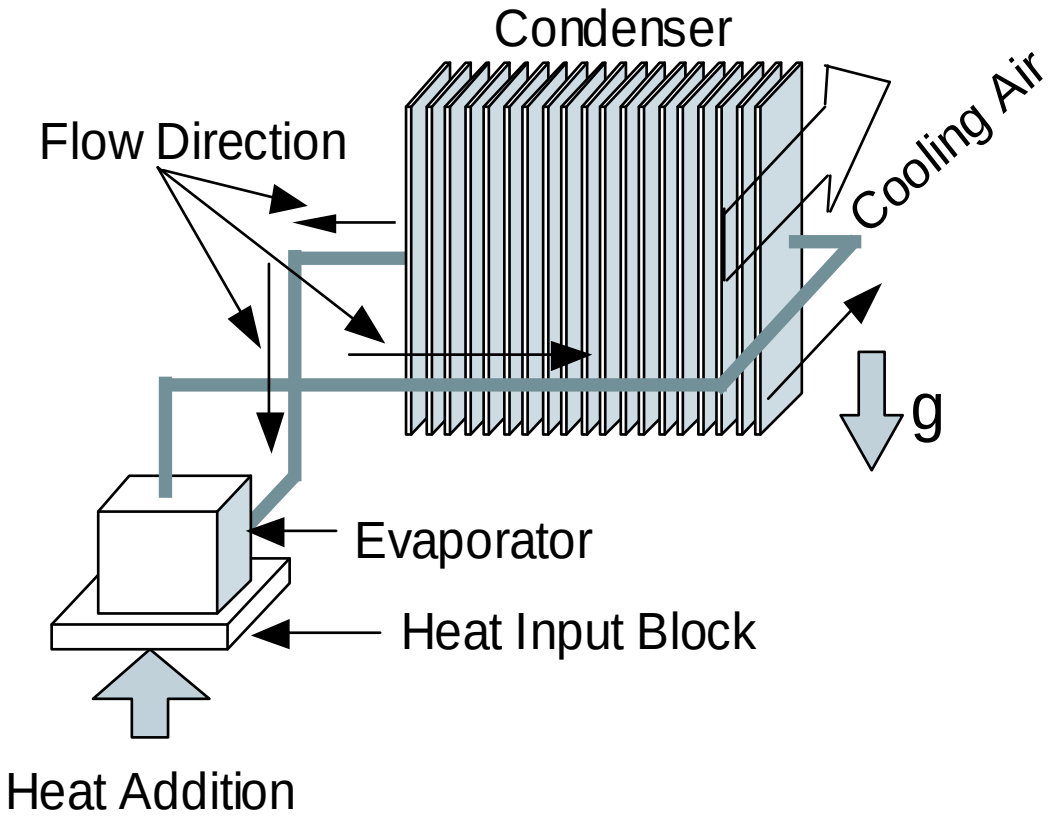

Figure 2: Typical arrangement of a dual chamber thermosyphon

responsible for the transport of the vapor from the evaporator to the condenser. The vapor gets condensed back to the liquid in the condenser by releasing the absorbed heat to the ambient. The condensed liquid then returns back to the evaporator through the connecting tubing and the cycle continues. The density driven pressure head makes the thermosyphon an attractive thermal management solution as a passively run system. Considerable research has been done on the suitability of using thermosyphon as a thermal management solution. Research done under laboratory setting has shown the importance and prospect of thermosyphon as a compact, high performance thermal management device, both in terms of flexibility afforded through the independent placement of the evaporator and the condenser and cooling capacity range. Proper design considerations of the thermosyphon needs to incorporate the

fundamental understanding of boiling and condensation, which will help in designing the two most important chambers of the thermosyphon - evaporator and condenser.

Over the years two distinct type of studies have emerged on boiling - boiling with enhanced structures and boiling at sub-atmospheric pressures. Extensive research has been done to understand the boiling phenomena with enhancement structures. The studies have involved boiling enhancement structure of various configurations - surface enhancements, stacked porous structures, commercial enhancement structures like Gewa-T, Hitachi Thermoexcel etc. The studies have highlighted the reduction of incipience overshoot and higher heat flux capability as the beneficial aspects of using boiling enhancement structures (one of the studies is highlighted in Figure 3). Moreover, some studies have shown that the use of boiling enhancement structure may lead to a reduction in the size of the evaporator. Most of the studies done on enhancement structures used dielectric liquids like PF5060, FC72 as the working fluid. Water on the other hand, has been shown to possess better thermal properties with respect to dielectric liquids. Moreover, with respect to electronics cooling applications, low temperature initiation of boiling is desired. This will necessitate the creation of sub-atmospheric conditions in the evaporator, which will lower the saturation temperature of water and thus aid in low temperature initiation of boiling. Pal et al. [3] demonstrated a thermosyphon prototype implemented in a commercial desktop PC, incorporating boiling enhancement structures with water as the working fluid. Their study showed that water at reduced pressures performed as a better working fluid than PF5060 (Figure 4). However, few works exist in the area of sub-atmospheric boiling of water with enhancement structure, so there is a definite need for thorough understanding in this area. Moreover, the operational characteristics of thermosyphon at reduced pressures are poorly understood. As a result, a closer look into the fundamentals of boiling of water at reduced pressures is required, which will provide considerable knowledge base for optimizing the performance of

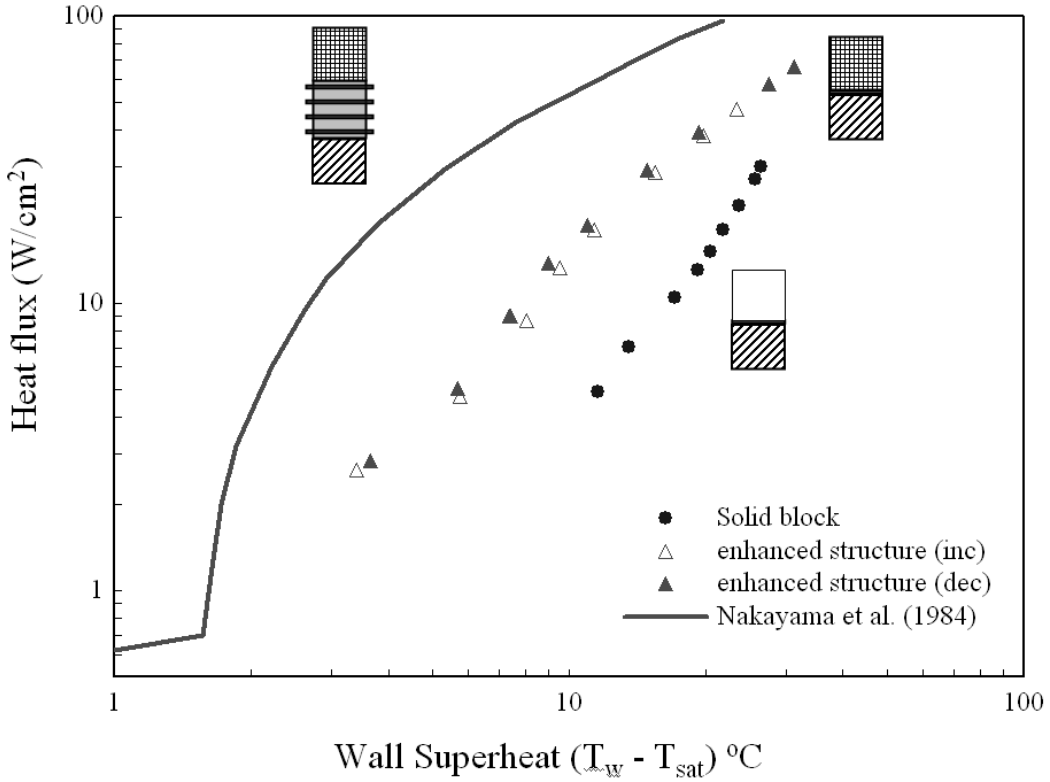

Figure 3: Comparison of heat transfer between enhanced and plain polished surface with FC-72 as working fluid (Adapted from Ph.D. thesis of C. Ramaswamy, *A compact two-phase thermosyphon employing microfabricated boiling enhancement structures, University of Maryland, College Park, 1999*)

the thermosyphon under varying conditions of internal temperature and pressure, enhancement structure geometry and external heat loads.

Apart from the operating pressure and geometry of the boiling structure, the liquid-fill volume is also an important criteria for the design of closed loop thermal solutions like the thermosyphon. Previous studies on boiling of liquids at atmospheric pressures have shown that the liquid-fill volume should be sufficient to keep the boiling structure completely immersed. However, in a closed system at sub-atmospheric pressures, the liquid-fill volume also affects the pressure inside the system. The volume of the liquid will affect the volume of the vapor space available and depending on the rate of vapor generation, the vapor pressure inside the system will vary accordingly. However, the effects of the liquid-fill levels on the thermal performance

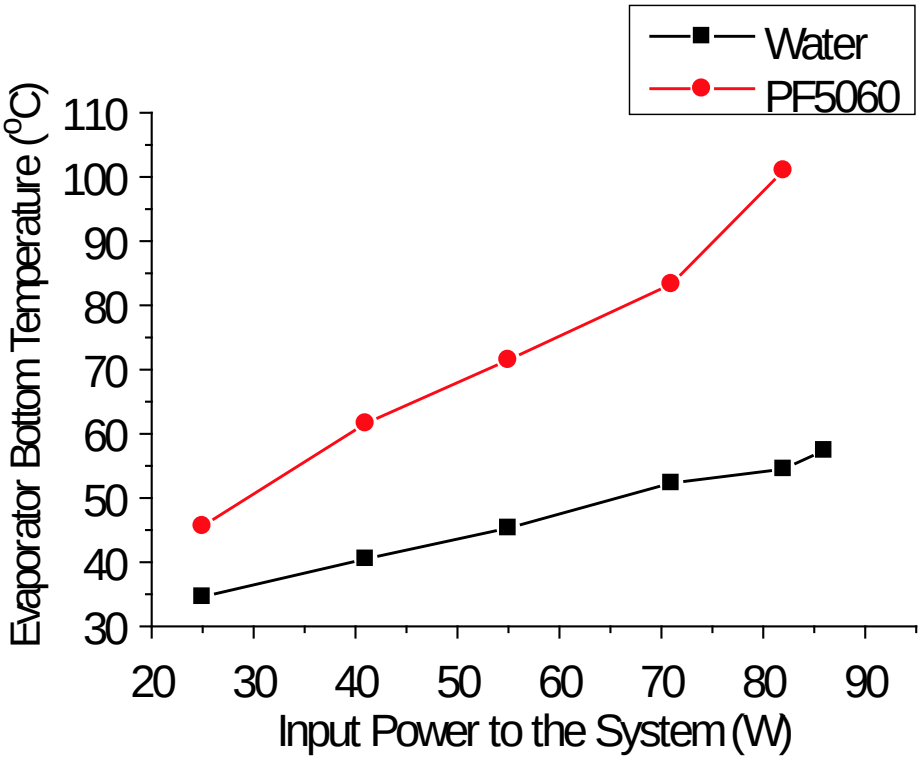

Figure 4: Comparison of heat transfer performance of Water vs. PF5060

of thermosyphons have largely been overlooked. So a detailed parametric study on the thermal performance at various liquid-fill levels will help in understanding the optimum liquid volume with respect to pressure and enhancement structure geometry and thus aid in designing a compact evaporator.

While a proper design of the evaporator will address the heat transfer issues from the source to the sink, a proper design of the condenser would address the issue of dissipating the heat from the heat sink to the ambient atmosphere. Countering the thermal resistance in the air-side of the condenser is a major issue in the design of heat sinks. However, for in-tube condensation, the heat transfer coefficient has a substantial effect on the overall heat transfer characteristics of the condenser. Use of micro-channels for the transport of working fluid would certainly increase the surface area of heat transfer. Moreover, for non-circular channels, an additional heat transfer enhancement mechanism, the "Gregorig Effect" [4] comes into play because of surface tension in small length scales. Some recent modeling studies have shown that condensation heat transfer can be improved with the use of micro-configured channels of non-circular cross-section. The studies are preliminary in nature and do not present an integrated approach in accounting for the combined effects liquid and vapor transport. As such, more detailed studies are required to validate the previous studies and also provide new insights into the condensation phenomenon.

1.2 Literature Review

1.2.1 Thermosyphon as a thermal management solution

Considerable prior work exists on the use of thermosyphon as a cooling device. Studies on the operation of thermosyphons have targeted both experimental and theoretical fronts. The experimental research were conducted for studying the effect of the various operational parameters like liquid-fill volume, inclination, geometric dimensions, and working fluids for obtaining optimum thermal performance. The modeling studies, on

the other hand, have focussed on gaining an understanding of the interaction between the flow parameters and heat transfer.

Palm and Tengblad [5] reviewed simple and advanced thermosyphon loops and also thermosyphons involving cooling by immersion boiling and by use of an external thermosyphon. A thermosyphon design with multiple evaporators was proposed by Tengblad and Palm [6]. The thermosyphon was used for cooling of hot components on vertical printed circuit boards (PCB) and utilized R142b and R22 as working fluids flowing through copper evaporators and copper sheet condensers, which were either air-cooled or water-cooled. Later, Ramaswamy et al. [7] investigated the thermal performance of a dual-chamber thermosyphon with respect to evaporator inclination, liquid fill volume and contact resistance. In their design, they used boiling enhancement structure, similar to the design proposed by Nakayama et al. [9]. Using a similar thermosyphon setup, Ramaswamy et al. [10] studied the effect of evaporator confinement and transient loads on the performance of a enhanced structure based thermosyphon. Later, Ramaswamy et al. [11] also studied the combined effects of subcooling and operating pressure (40-350 kPa) on the performance of the thermosyphon. Webb and Yamauchi [12] proposed a different design of a thermosyphon, which utilized automotive type condenser. Their condenser design had an aluminum construction and used R143a as the working fluid. Under laboratory conditions, their system was able to dissipate 100 W for a maximum boiling surface temperature of 70 ^{o}C. While the previous studies looked into the fundamental principles of thermosyphon operation, Garner and Patel [13] concentrated on the applicability of thermosyphons in high density packaging. They showed that thermosyphons are capable of removing high heat fluxes, with minimal volume requirement at the evaporator and can remove heat effectively from core electronics module while being flexible in its arrangement. Later Yuan et al. [15] used a thermosyphon configuration, similar to Ramaswamy et al. [8] and looked into the

evaporator and condenser location-specific design issues for the thermosyphon. All the studies mentioned so far were laboratory implementations of various thermosyphon configurations. Pal et al. [3] were the first in implementing a thermosyphon configuration in a commercial desktop PC. Their design used water as the working fluid and incorporated boiling enhancement structure in the evaporator. Their system was capable of dissipating 85 W while keeping chip temperature below 85 ^{o}C. The studies mentioned above shows that the operating principle of a thermosyphon can be utilized in designing high heat flux thermal management solutions. However, a detailed understanding of the operating principles will require the fundamental studies of evaporation and condensation. A listing of the previous research on thermosyphons is shown in Table 1.

Table 1: Research on Dual-Chamber Thermosyphons in Electronics Cooling

Investigators	**Working Fluid**	**Maximum Heat Flux**	**Key Features of Study**
Tengblad and Palm [6]	R142b and R-22	150 W/cm^2	Use of multiple evaporators in series to cool different components.
Palm and Tengblad [5]	-	-	Reviewed simple and advanced thermosyphon loops.
Ramaswamy et al. [7]	FC-72	100 W/cm^2 @ 27.8^{o}C wall superheat	Effect of evaporator inclination, liquid fill volume and contact resistance on performance.
Ramaswamy et al. [8]	FC-72	42 W/cm^2	Use of boiling enhancement structure to enhance thermal performance.
Ramaswamy et al. [10]	FC-72	100 W/cm^2	Study of evaporator confinement and transient loads on performance.
Ramaswamy et al. [11]	FC-72	100 W/cm^2	Effects of subcooling and operating pressure on performance.
Webb and Yamauchi [12]	R-134a	67 W/cm^2	Thermosyphon concept using automotive type louver fins in the condenser.
Garner and Patel [13]	-	-	Use of thermosyphons in high density packaging.
Yuan et al. [14]	PF-5060	32.5 W/cm^2	Placement of condenser and evaporator.
Haider et al. [16]	PF-5060	-	Analytical approach to model the thermosyphon performance and obtain saturation temperature.
Pal et al. [3]	Water	56 W/cm^2	Performance evaluation of a desktop implementation of thermosyphon using boiling enhancement structure.

1.2.2 Review of boiling under sub-atmospheric conditions

Boiling of water at sub-atmospheric pressures has been investigated in the past by researchers. The studies have been done mostly on plain surfaces or wires and in some cases on machine roughened surfaces and were focused mainly on the effects of reduced pressures on the bubble generation process, the critical heat flux, the incipient superheat and surface temperature. One of the early works on boiling at sub-atmospheric pressures was by Van Stralen [17], who studied boiling of water and a mixture of methylethylketone on an electrically heated platinum wire within a pressure range of 13-101 kPa. His observations pointed to reduced heat transfer characteristics during boiling at sub-atmospheric pressures. He observed that the transition period to the onset of nucleate boiling decreased with increasing pressure. Decrease in pressure led to increase in the bubble sizes, while reducing the maximum heat flux attained. All these characteristics, depicted a general shift in the boiling curve towards lower heat transfer with reduction in pressure. Ponter and Haigh [18] visualized boiling of water for the pressure range of 13-101 kPa with a tubular stainless steel heater in a stainless steel cylinder. Similar to Van Stralen [17], they also observed a reduction in potentially active bubble nucleation sites. Their observations confirmed that bubble formation at low pressures differ markedly from that at atmospheric pressure. Further, they also observed that the increase in pressure led to an increase in the critical heat flux. Another notable study on the mechanism of nucleate boiling at atmospheric and sub-atmospheric pressures was by Miyauchi and Yokura [19], who suggested that a rapidly growing bubble would accelerate the liquid surrounding the bubble, which will increase the pressure inside the bubble with respect to the outside pressure. They believed that the process would induce a higher saturation pressure inside the bubble, leading to a higher wall superheat, which will suppress the bubble growth rate. Later, Van Stralen et al. [20]

experimentally investigated the growth rate of vapor bubbles in water using a nickel-plated copper-heating surface for a pressure range of 2-26.7 kPa. They observed that the bubble departure time and departure radius increased substantially with decrease in operating pressure. Joudi and James [21] focused on a pressure range of 25-101.3 kPa for boiling in water, R-113 and methanol, and observed fluctuations in the surface temperature during incipience. They noted that decreasing pressure lowered the incipience superheat. They also observed that the number of incipient bubbles greatly reduced with deceasing pressure. The incipient bubbles become intermittent in generation, unpredictable in location and duration and deformed in shape. Temperature fluctuations were also noticed with reduction in pressures at sub-atmospheric pressures where bubble population greatly reduced. Fath and Judd [22] investigated micro-layer evaporation and found higher wall superheats with decrease in operating pressure. With increase in surface heat flux, they found an increase in the bubble generation site density, which facilitated transfer of additional heat. With increase in surface heat flux, they found an increase in the site density in bubble generation, which facilitated transfer of additional heat. The frequency of bubble varies with heat flux, however, decreases with pressure. Moreover, bubble flux density increases with increasing system pressure. Latsch et al. [23] investigated subcooled boiling in turbulent annular flow within a pressure range of 0.25-4 bar. They observed that the ability of water to absorb air decreases rapidly at sub-atmospheric conditions, so the difference between degassed and saturated water becomes considerably small. They also observed that there is no difference between saturated and degassed water as regards the initial boiling point. However, influence of pressure was not noted beyond 80 kPa. Tewary et al. [24] observed that the heat transfer coefficient decreases with a decrease in saturation pressure in the nucleate boiling regime, within a pressure range of 60-100 kPa. They studied nucleate boiling on a horizontal tube at atmospheric and sub-atmospheric pressure with water and NaCl solution. McGillis et al. [25]

investigated the boiling of water in a thermosyphon configuration at sub-atmospheric pressures using a plain surface with surface enhancements. They observed that lower pressure generated larger nucleation bubbles, which impeded growth of active nucleation sites, resulting in larger wall superheats. However, surface enhancements improved the heat transfer with lower wall superheat and increased the critical heat flux. More recently, Rainey et al. [26] did experiments with FC-72 at reduced pressures from microporous structures in the pressure range of 30-150 kPa for liquid subcooling range of 0-50 ^{o}C and observed that increase in pressure brings an increase in CHF with a decrease in boiling incipience.

A selective listing of the previous research on boiling at sub-atmospheric pressures is shown in Table 2.

Table 2: Research on Boiling at Sub-atmospheric Pressures

Boiling Surface	**Working Fluid**	**Pressure Range**	**Heat Flux and Operating Constraints**	**Investigators**
Electrically heated horizontal Pt wire	Water and methylethylketone	76-10 cm of Hg	10 W/cm^2 at superheat of 40^{o}C @ 10 cm of Hg	Van Stralen [17]
Tubular stainless steel heater	Water	760-100 torr	100 W/cm^2 at a superheat of 40^{o}C @ 100 torr	Ponter and Haigh [18]
Nickel plated copper	Water	26.7-2.0 kPa		Van Stralen et al. [20]
Flat stainless steel horizontal surface	Water, R-113 and methanol	1.0-0.25 atm	115 kW/m^2 at a superheat of 15^{o}C for water	Joudi and James [21]
Inner surface of smooth concentric annular tube	Water	0.25-6.0 bar	120-130 W/cm^2 at a velocity of 1 m/s	Latsch et al. [23]
Horizontal tube	Water and NaCl solutions	60-100 kPa	100-200 kW/m^2 at superheats of 5-16 K	Tewari et al. [24]
Horizontal surface with studded fins, copper beads and surface finishes	Water	4, 9 and 101 kPa	175 W/cm^2 at a superheat of 40^{o}C @ 9KPa	McGillis et al. [25]
Microporous enhanced surface	FC-72	30-150 kPa	2×10^5 W/m^2 at a superheat of 14K @ 30 kPa 2.67×10^5 W/m^2 at a superheat of 11K @ 100 kPa	Rainey et al. [26]
Machine roughened surface	FC-72	30-150 kPa	1.15×10^5 W/m^2 @ 30 kPa & 23K wall superheat 1.60×10^5 W/m^2 @ 100 kPa & 17K wall superheat	Rainey et al. [26]

1.2.3 Review of boiling with enhancement structures

The high heat flux capability of enhanced structures for boiling with dielectric liquids and refrigerants makes them excellent candidates for integrating in the evaporator of compact thermosyphons. Surface microstructures have been shown to enhance the boiling heat transfer in liquid cooling of miniature heat sources by reducing the incipience excursion and increasing the critical heat flux. Boiling enhancement structures may employ microroughness, or porous and re-entrant cavities to increase the number of active nucleation sites and also increase the effective heat transfer area. However, heat flux capability of enhanced structures for boiling with water is not fully understood. Existing literature on boiling with enhancement structures shows that the enhancement varied from machine-induced roughness to more complex structure of interconnected pores and channels. Most of these studies were done at atmospheric pressure. A list of some of the research employing boiling enhancement structures for electronics cooling is provided in Table 3.

Nakayama et al. [27] studied boiling from enhanced structures at atmospheric pressures with R-11, water and liquid nitrogen. The boiling enhancement structure was made of interconnected internal cavities in the form of tunnels and small pores, connecting the pool liquid and the tunnels. They did their experiments at decreasing heat fluxes, and found that hysteretic behavior was less pronounced than that observed in boiling from plain surfaces. For enhanced surfaces, the wall superheat remained much lower than for plain surfaces for the range of heat flux applied for the experiments. Bergles and Chyu [29] investigated pool boiling of water and R-113 from surfaces with porous metallic coatings. Their observations revealed hysteresis in the boiling process; however, surface enhancements improved the heat transfer. They also found that surface aging, surface sub-cooling and changes in heat flux affect temperature overshoot and the resultant boiling curve hysteresis. Experiments on boiling with commercial enhanced surfaces, Gewa-T and Thermoexcel-E, were

done by Marto and Lepere [30]. The enhanced surfaces always produced higher heat transfer coefficients than plain surfaces, though they noticed some variation in the level of the performance among the various surfaces at low and high heat fluxes. They also found that the surface, which was allowed to cool for the maximum amount of time between successive boiling experiments, required the largest superheat prior to bubble nucleation. Later, Nakayama et al. [9] experimented on enhancement of boiling heat transfer using a stud, which has fine surface structures and was attached to the back of the heat-dissipating device. Their experiments were done at atmospheric pressure with both flourinert (FC-72) and refrigerant (R-11). They observed that the boiling curve has a steeper slope prior to established nucleation than is expected in natural convection. Anderson and Mudawar [31] used FC-72 as a working fluid and found that boiling incipience increased with more non-boiling time (idle time between successive boiling experiments). They found that their microstructures significantly shifted the boiling curves toward lower superheats, while increasing the incipience excursion. However, increasing roughness of the boiling surface initiated incipience earlier and reduced the excursion.

Table 3: Research on Boiling with Enhanced Surfaces

Enhanced Structure or Surface	**Working Fluid**	**Heat Flux and Operating Constraints**	**Investigators**
Structured surfaces with interconnected tunnels	Water, R-11 and liquid Nitrogen	10-100 W/cm^2	Nakayama et al. [27]
Dendritic structures at back of chip	FC-86	60 W/cm^2 at 85^{o}C junction temperature	Oktay [28]
Commercial porous metallic matrix	Water and R-11	Water 10^3-10^5 W/m^2	Bergles and Chyu [29]
Union Carbide High Flux Surface, Hitachi Thermoexcel-E, Weiland Gewa-T	R-113 and FC-72	100-200,000 W/m^2	Marto and Lepere [30]
Microfins	FC-72	33 W/cm^2 at a superheat of 42^{o}C	Nakayama et al. [9]
Porous structure on heat sink stud	FC-72	16-17 W/cm^2 at a superheat of 21^{o}C	Nakayama et al. [9]
Microfin	FC-72	35 W/cm^2 at a superheat of 41^{o}C	Anderson and Mudawar [31]
Microstud	FC-72	50 W/cm^2 at a superheat of 52^{o}C	Anderson and Mudawar [31]
Channels of small widths	FC-72	30 W/cm^2 at a superheat of 20^{o}C	Nowell et al. [32]
Microporous, coated test heater	FC-72	2.67×10^5 W/m^2 at a superheat of 10^{o}K	Rainey et al. [26]
Stacked porous structure of copper	FC-72	80 W/cm^2 at a superheat of 25^{o}C	Ramaswamy et al. [33]

1.2.4 Review of boiling with various liquid-fill levels

For closed-loop systems, the liquid-fill ratio (defined as the volume of the working fluid in the evaporator to the total volume of the evaporator) of the working fluid in the evaporator is also an important design parameter. In a closed system like the thermosyphon, the fill ratio of the working fluid will affect the volume of the vapor space available and depending on the rate of vapor generation it will also affect the vapor pressure inside the system. Moreover, optimizing the liquid-fill ratio will also aid in the design of a compact boiling chamber. However, studies on the effects of the liquid-fill ratio (or liquid-fill level) on the thermal performance of a thermosyphon are very few and they are mostly concentrated on a particular internal pressure condition with plain boiling surface.

Abou-Ziyan et al. [34] studied a two-phase closed loop thermosyphon with water and R134a as working fluids for fill ratios of 0.4-0.8 (defined with respect to evaporator volume). For water, they found that a fill ratio of 0.5 gave the highest heat output flux. They found that the thermosyphon was sensitive to over-filling and under-filling for variable input heat fluxes with respect to a fill ratio of 0.5. As a consequence, the temperature of the adiabatic section was the lowest for the fill ratio of 0.5. Zuo et al. [35] studied a pulsating heat pipe mechanism, which utilized thermally driven movement of water in a serpentine loop. Their system achieved the highest heat flux of 220 W/cm^2 at fill-ratio of 0.7. A numerical model was proposed, which closely predicted the optimum fill ratio, however, detailed thermal characterization of the heat pipe with respect to the fill ratio was not provided. Ong and Haider-E-Alahi [36] also studied heat pipes with R134a as the working fluid for fill ratios of 0.35 to 0.8. The overall heat transfer coefficient of the thermosyphon increased with increase in fill ratio. Beyond a fill ratio of 0.4, the heat transfer coefficient showed the greatest increase. They found that the overall heat transfer coefficient increased monotonically with respect to the overall temperature difference of liquid bath temperature and

condenser temperature at a particular fill ratio. However, beyond a fill ratio of 0.5, the heat transfer coefficient was almost invariant with respect to bulk temperature difference. Park et al. [37] studied two-phase closed thermosyphon with FC-72 as the working fluid for fill ratios of 0.1-0.7. They found that the effect of fill charge ratio on the heat transfer coefficient in the evaporator was negligible. The fill charge ratio had influence on the heat transfer coefficient in the condenser, where the fill charge ratio was directly proportional to the condensation heat transfer coefficient.

The influence of fill levels, however, was quite different for dual chamber thermosyphons. Previous studies [6, 7] on dual chamber thermosyphons have shown that the thermal performance is independent of the liquid fill volume, as long as the boiling structure remains completely immersed. Tengblad and Palm [6] conducted experiments using refrigerants R142b and R22, in a closed loop two-phase thermosyphon at 11 W of input power. They found that beyond an optimum fill-ratio, the temperature in the evaporator was insensitive to the amount of liquid-fill. However, they observed a sharp increase in the evaporator temperature at very low fill-ratios, which they attributed to inadequate liquid supply to the evaporator. Contrary to the behavior observed in the evaporator, the authors observed a decline in performance of the condenser, even after increasing the liquid-fill beyond the optimum level. They noted that at higher fill ratios, more liquid reached the condenser and thus lined the walls of the condenser, which deteriorated its performance and increased its temperature. Ramaswamy et al. [7] studied boiling heat transfer from a dual-chamber thermosyphon, using PF5060 as the working fluid in the heat flux range 2-68 W/cm^2. They used four different liquid-fill levels, in which the boiling structure was kept either fully-submerged or partially-submerged. Their observations were similar to the observations of Tengblad and Palm [6]. They observed that the thermal performance of the thermosyphon was largely unaffected by the liquid-fill levels, as long as the structure was fully immersed in the working fluid. At very high heat fluxes, due to

vigorous boiling, the bubbles near the surface might block the liquid from reaching the surface, which resulted in a lower effective liquid-fill level, in which the structure stays immersed.

1.2.5 Review of modeling approaches on in-tube condensation

Microchannel devices are an attractive solution for high heat flux thermal management, because of their compact size and high heat transfer capability. Recent experimental works on small-scale channels and capillary pumped loops have shown that microchannel based condensers can achieve very high heat transfer coefficients. Interfacial tension at small scales is considered to be the primary factor for the enhancement of condensation heat transfer through the *Gregorig effect* [4], as discussed by Carey [38] and Rose [39]. Analytical studies on condensation have been mostly confined to the annular flow model in circular channels in horizontal and vertical configurations. While the most common approach is the Nusselt type analysis, studies have also incorporated interfacial and wall shear stress [40, 41, 42, 43], no liquid entrainment in the vapor core [44], surface tension [45], surface curvature, surface waviness [46], condensate subcooling [43] and change in momentum between vapor and fluid flow [47]. Moreover, gravity [48] creates an important difference between the treatment of condensation in horizontal and vertical channels.

Compared to circular channels, condensation in non-circular channels/microchannels has been much less studied. Chiou et al. [49] studied condensation in a horizontal elliptical tube and showed that surface tension plays an important part in controlling condensate thickness and provides better performance than circular channels. Guo and Anand [50] presented one of the first studies on condensation in horizontal rectangular channels by incorporating vapor shear force and gravity in the model. The authors used Nusselt's approach to obtain the condensate profile for the vertical walls only, while the condensation on the horizontal walls were treated through

correlations and mass balance. As a result, the liquid-vapor interface profiles were not obtained for the top and bottom horizontal walls. Riehl et al. [51] considered convective condensation in horizontal parallel rectangular microchannels having a porous boundary on one vertical side. Their investigation concluded that the inertial forces impart negligible influence on the Nusselt number. A detailed model for condensation in vertical triangular mini channels (D_h = 0.58-1.16 mm) was proposed by Zhao and Liao [52] taking surface tension into account. They divided the cross-section of the channel into six symmetrical parts and solved for the condensation. The condensate layer was divided They analyzed the liquid and vapor layers separately and considered mass, momentum and energy conservation between them. Their model predicted a gradual increase in the thickness of the liquid layer at the corner of the channel, while thinning of the condensate layer occurred along the walls. The vertical orientation of the channel led to a simplified model because of six-fold symmetry of the triangular channel. With a horizontal rectangular/triangular channel, only two-fold symmetry can be achieved, which was studied by Wang and co-workers [53, 54] following a similar line of approach as Zhao and Liao [52]. Their model predicted a thicker liquid zone at the corners of the channel compared to the channel walls (similar to [52]), while showing a gradual increase in the thickness of the condensate pool at the bottom of the channel. Using a similar modeling approach, Wang and Rose [55] found that gravity has an effect on the condensate distribution along the vertical and horizontal walls of a channel. They found that for rectangular channels with aspect ratio (height/length) < 1, the condensate tends to accumulate along the bottom wall of the channel, with thin films in the top and vertical walls, while for aspect ratio > 1, thin condensate film tends to adhere to the vertical wall, while the top and bottom walls are "flooded" with condensate. The model of Wang and co-workers [53, 54, 55] however, did not solve the energy equation for the vapor core and also did not mention how the coupling between the liquid and vapor phases was

achieved. Moreover, their numerical analysis of the liquid in the corners of the channel lead to a discontinuous profile of the condensate and heat transfer coefficient, which might influence interfacial tension and ultimately, the profile of the condensate.

1.3 Objectives

The previous studies on enhanced structures were mainly performed at atmospheric pressures, however the effect of sub-atmospheric pressures on enhanced structures are not properly understood. Moreover, there is also a lack of understanding on the effects of enhanced structure and sub-atmospheric pressures in a compact system like dual-chamber thermosyphon. One of the main objectives of the current study is to perform a comprehensive characterization of boiling of water at reduced pressures in a compact thermosyphon loop using boiling enhancement structures. Since water possesses better thermal properties than dielectric liquids, the thermal performance of a thermosyphon using water is explored experimentally for various system pressures, enhancement structure geometries and external heat loads and is part of the objective. A part of the objective is also to compare the thermal performance of the boiling from enhanced structures to boiling from a plain surface.

The previous experiments on the effect of fill ratio were mostly performed at atmospheric pressures, and as such the effects of pressure were ignored. Moreover, the effect of boiling enhancement structure in presence of different liquid-fill levels is not fully understood. In this regard, another main objective of the current study is to understand the influence of liquid-fill levels on the heat transfer in a thermosyphon utilizing boiling enhancement structures at sub-atmospheric pressures. In a two-phase system with heat exchange between the evaporator and condenser, volume of the two phases will affect the condensation heat transfer, which will in turn affect the surface heat flux conditions and vice versa. In that respect, the current study will incorporate varying saturation conditions inside the thermosyphon at different heat

fluxes at different liquid volumes.

So the main objectives of the experimental study on boiling will be to:

1. Investigate the boiling process from enhanced structures at varying system pressures.

2. Investigate effect of the boiling enhancement structure geometry.

3. Investigate effect of liquid fill on the thermal performance.

The literature survey shows that the present state-of-the-art in modeling of condensation in rectangular microchannels lacks an integrated approach in combining the transport behavior of fluid and vapor phases and needs further validation with new modeling approaches. In this regard, the main objective of the numerical study will be to develop a detailed model of condensation in rectangular channels through simultaneous solving of the mass, momentum and energy equations and by incorporating gravity, surface tension, interfacial shear stress, axial pressure gradient, saturation temperatures and interfacial thermal resistance. As a whole, the numerical work will focus on the following objectives:

1. Characterization of heat transfer performance during condensation in microchannels.

2. Development of a model to simulate the condensation in rectangular microchannel.

1.4 Summary and Organization of the Current Study

The trend in increasing heat flux from high performance microelectronic parts has motivated the development of efficient two-phase thermal management devices through more detailed studies on two-phase heat transfer. Dual-chamber thermosyphons are very attractive solutions for implementing two-phase heat transfer.

The proper design of thermosyphon would need detailed understanding of the mechanism of boiling and condensation in the thermosyphon. Existing literature shows a lack in the understanding of boiling at sub-atmospheric pressures with water. Moreover, condensation in microchannels requires a detailed understanding for designing compact condensers with high in-tube heat transfer coefficient. The current study attempts to address the above issues through detailed studies on the boiling of water at sub-atmospheric pressures with enhanced structures and also on condensation in microchannels. A brief literature review is also presented to give a perspective on the existing state-of-the-art on boiling and condensation studies and the areas in which improvements are sought. All the issues mentioned above are discussed in the present chapter.

In chapter 2, the details of the experimental setup designed to carry out the boiling experiments are discussed. The fabrication of the experimental setup, the experimental procedures, the data acquisition system and the uncertainty in the measured data are discussed.

In chapter 3, the results of the experimental study on the effects of pressure and enhanced structure on thermal performance are discussed. The details of a baseline study on boiling of water from a plain surface at sub-atmospheric pressures are also discussed. In this chapter, the discussions are done with respect to boiling curves at the pressures of interest.

In chapter 4, the effects of liquid-fill volume on the thermal performance of the thermosyphon are discussed. The boiling curves and the thermal resistance data are discussed to study the effects of three liquid-fill levels for all the boiling structures and saturation pressures under consideration.

In chapter 5, the detailed numerical model for studying condensation in rectangular microchannels is discussed. The assumptions made for the numerical model are discussed, the governing equations for mass, momentum and energy transport are

derived from the conservation equations, the discretization steps are discussed and finally the solution procedure is also discussed.

In chapter 6, the results of the numerical simulation of condensation in a rectangular microchannel is discussed. The transport and heat transfer phenomena in a rectangular microchannel are discussed with respect to the profiles of the liquid-vapor interface profile along the channel and also with spatial variation of various flow and thermal parameters like heat transfer coefficient, quality, void fraction, liquid and vapor phase velocities, pressure drop etc.

In chapter 7, final conclusions are drawn from the present study and an overall summary is given for the study. The unique contributions of the study are highlighted and the recommendations for future work to improve upon the present work are also discussed in this chapter.

CHAPTER II

EXPERIMENTAL SETUP AND PROCEDURES

Boiling experiments were conducted in a thermosyphon prototype, which was designed to accommodate a wide range of external heat flux and simultaneously allow measurement of pressure and temperature at various locations in the system. The evaporator was the main focus of the experimental study. An important component of the evaporator was the boiling enhancement structure. Different geometries of the structure were considered to assess their effect on the boiling heat transfer. Another important design parameter for the evaporator was the volume of working fluid, which was studied by subjecting the evaporator to various amounts of liquid charge. Moreover, the operating pressure was also changed to find the optimum operating envelope. In the following sections detailed descriptions are provided of the components, the data acquisition process and the measurement uncertainty in the parameters.

2.1 Experimental Setup

The test setup, seen in Figure 5, consisted of the evaporator and the condenser connected through flexible copper tubing (external diameter 6.35 mm). A full view of the experimental setup is shown in Figure 6. This arrangement created a thermosyphon loop with the condenser placed at a higher elevation than the evaporator, which helped in gravity-assisted draining of the condensed liquid from the condenser to the evaporator. The experimental setup was designed to monitor and control the various process parameters through a data acquisition system.

A detailed sketch of the evaporator along with the heat-generating unit is shown in Figure 7. A fully assembled heater block housing is shown in Figure 8. The evaporator

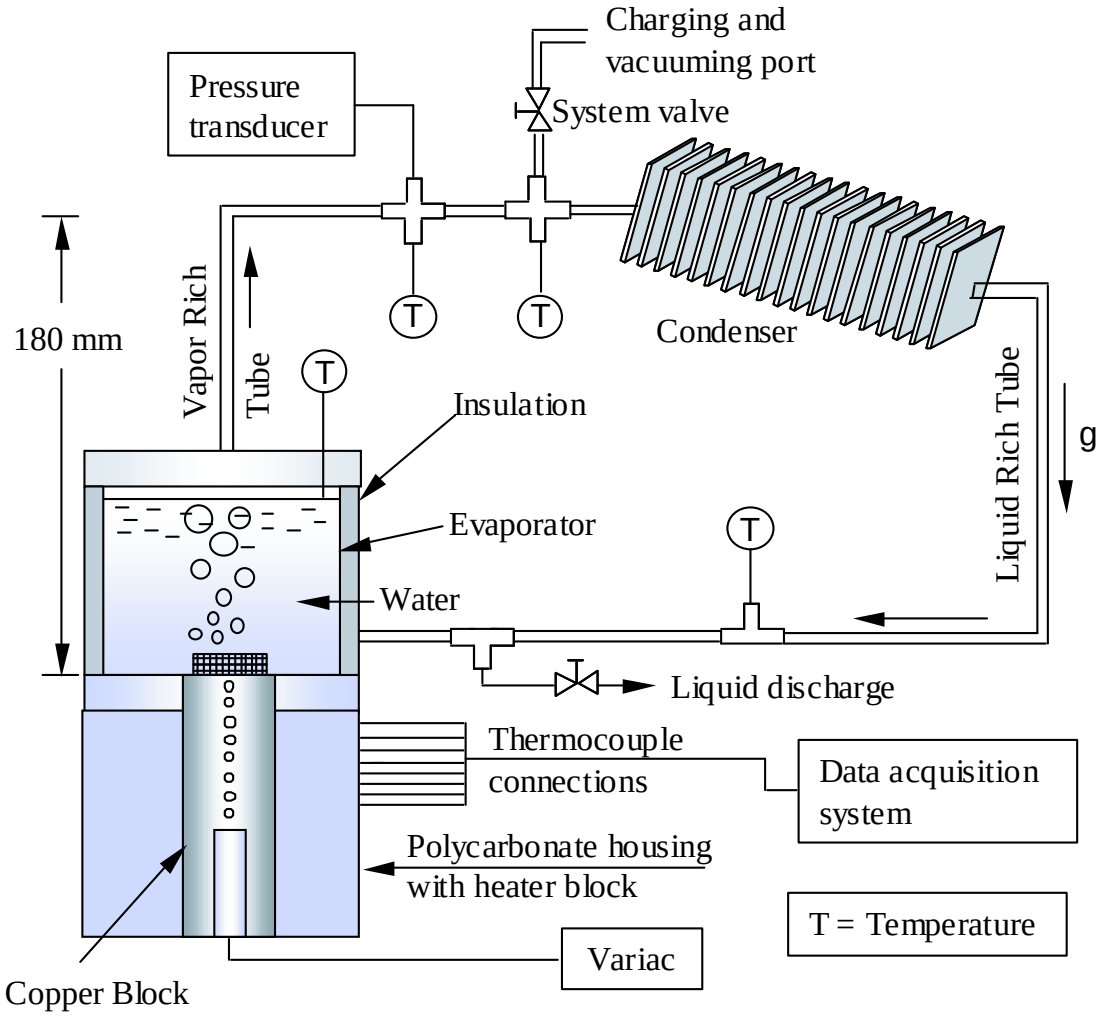

Figure 5: Schematic of the experimental setup

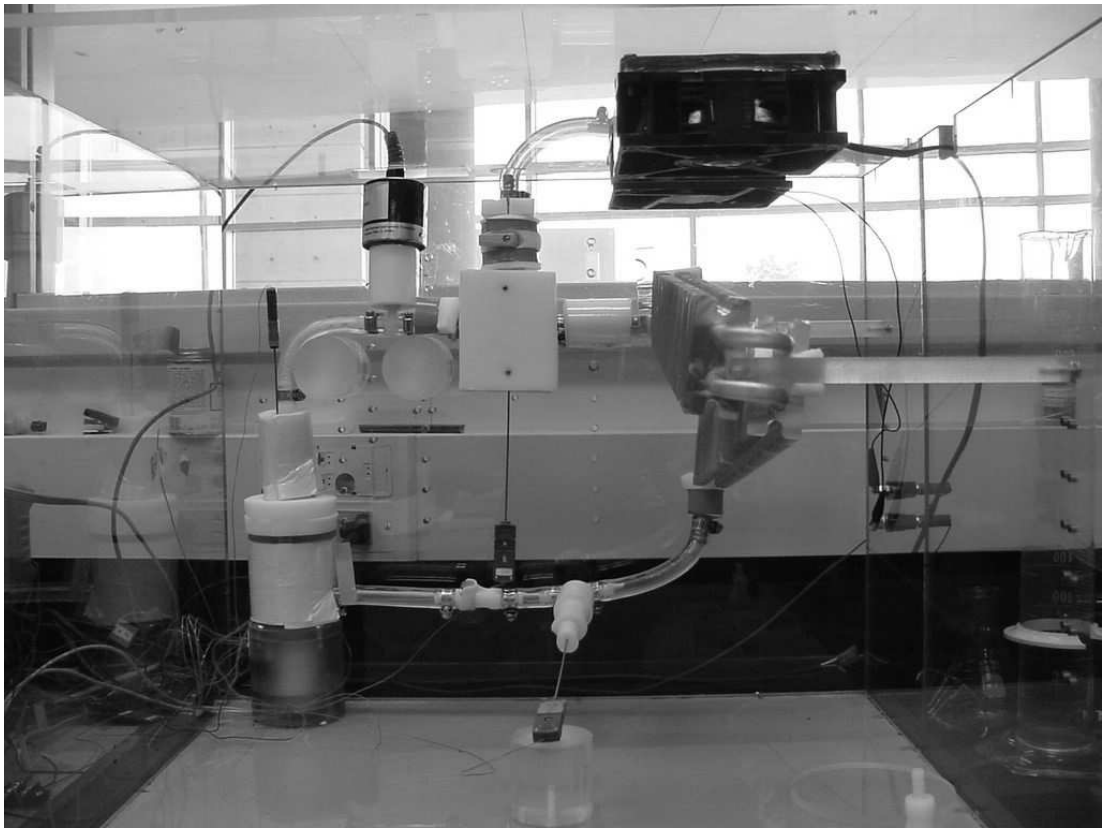

Figure 6: Full view of experimental Setup

was an annular cylindrical chamber, 65 mm in height (height of the cavity inside was $\sim$ 42 mm) and 38 mm in inner diameter, made of translucent polycarbonate, which allowed the viewing of the liquid level inside the chamber and the initiation of bubble generation. The top and bottom of the evaporator chamber were enclosed by two polycarbonate caps, each one press-fitted with two Buna-n o-rings. The top cap allowed passing of the vapor to the condenser, while the bottom cap was press-fitted to the heat input block and allowed the introduction of the enhancement structure into the evaporator chamber. The heat input block was a cylindrical copper rod, 20 mm in diameter and 82 mm in length, press-fitted to the bottom cap with double o-rings. One end of the block was machined to a 12.7 mm square cross-section of around 2 mm height. After fitting the copper rod in the bottom cap (through a square shaped hole $\sim$ 12.7 mm), the square surface was flush with the top surface of the bottom cap. The exposed square surface was used as the boiling surface in the baseline study. Boiling enhancement structures were soldered to the square surface for the rest of the experiments. The other end of the block had a drilled-hole for accommodating the heat source. A cartridge heater (maximum power of 200 W) was used as the heat source. A high thermal conductivity paste (k = 2.3 W/m-k, temperature resistant up to 200 ^{o}C) was used between the cartridge heater surface and the drilled-hole surface to reduce thermal contact-resistance between them.

For the present study, de-ionized water was chosen as the working fluid and for all the experimental runs the evaporator was charged almost to its full capacity with approximately 0.06 kg of water. The power to the cartridge heater was supplied from a variac (0-140 V), connected in series to a 1 Ω precision resistor. The voltage drops across the cartridge heater and the precision resistor were measured separately to obtain the power input to the heater. Temperatures at various points in the system were measured with type-T (Copper-Constantan) sheathed thermocouples (diameter $\sim$ 0.08 mm). The temperature gradient along the copper block was calculated from

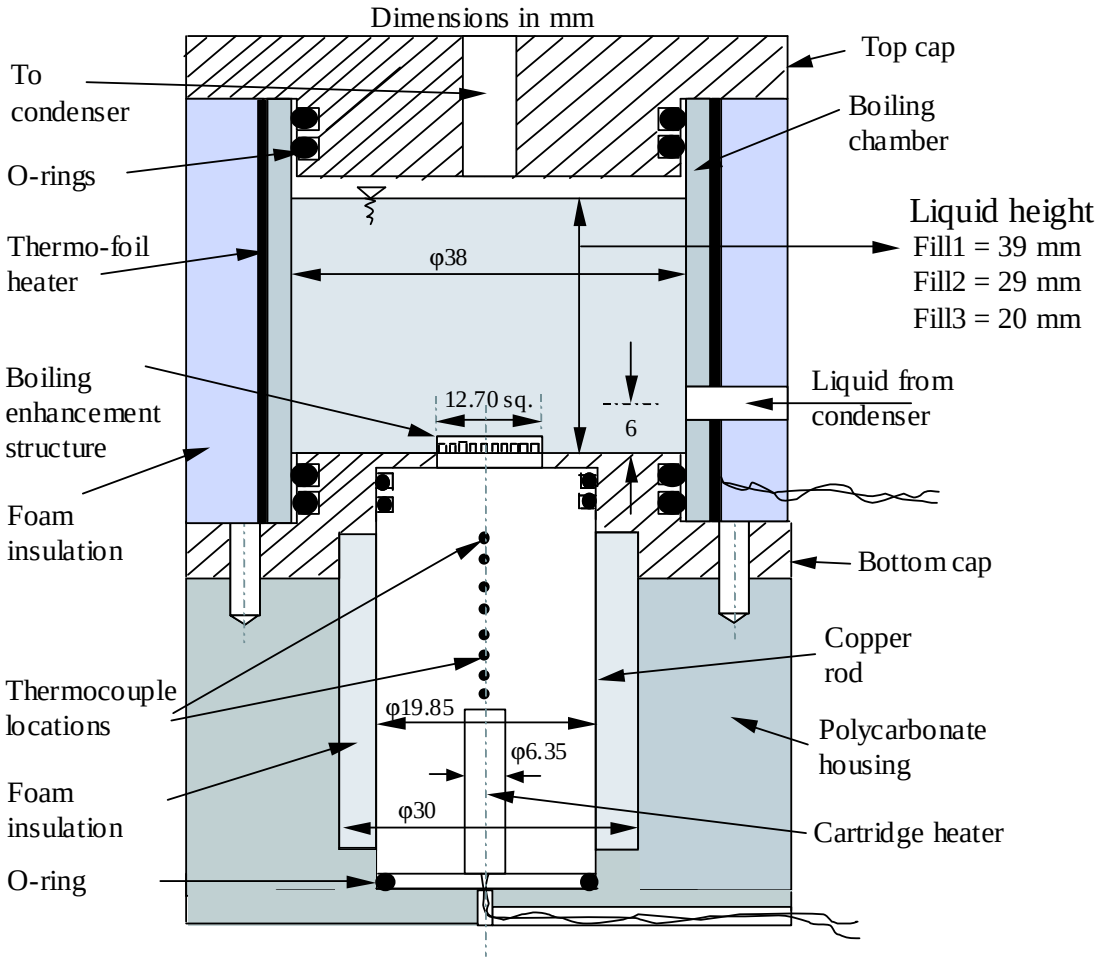

Figure 7: Detailed sketch of the evaporator assembly

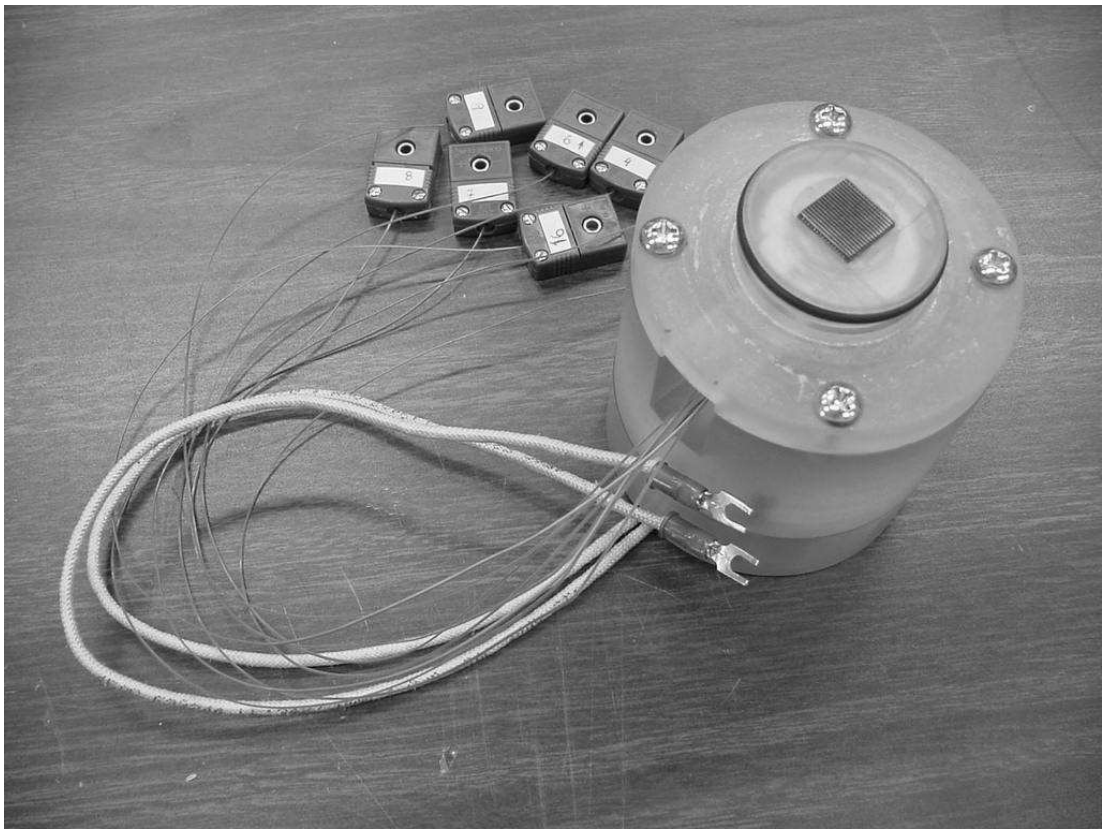

Figure 8: Fully assembled view of the heater block housing

the temperatures measured by 8 thermocouples, which were fitted inside small grooves along the length of the copper block at varying distances from the boiling surface. Grounded type-T thermocouple probes were placed at following points inside the system: evaporator chamber, in the flow path between evaporator and condenser, condenser entry and condenser exit. The pressure inside the system was measured by a high precision current output (4-20 mA) pressure transmitter (0-200 kPa absolute), which was accurate up to 0.13% of the full scale.

2.1.1 Boiling Enhancement Structure

A principal focus of the study was to investigate the effect of enhancement structure on boiling at sub-atmospheric pressures. The structure used in the present study is similar in construction to the ones used by Nakayama et al. [9], Ramaswamy et al. [33] and Launay et al. [56]. A detailed sketch of the enhancement structure used in the present study is shown in Figure 9. The basic component of the structure was a single layer of copper (12.7 $\times$ 12.7 $\times$ 1 mm), in which an array of rectangular channels (width 0.35 mm) was cut in mutually perpendicular directions (pointed in Figure 9 as "channel", which is cut on one side of the copper layer and "cross-cut" channel, which is cut on the other side of the copper layer) on both sides. The depth of each channel is more than half the thickness of the copper layer, resulting in the intersection of channels from both sides, forming an array of square pores.

The copper structure layers were fabricated using the wire EDM (electro discharge machining) method. The individual copper layers were stacked on the square surface of the copper block with a layer of 63Pb-37Sn ribbon-solder in between them. The stacked structure was bonded to the copper block by achieving a junction temperature greater than 200 ^{o}C. The enhancement structure thus formed (Figure 9), resulted in geometrical features that are different from the geometries of surface enhancements used in previous studies on sub-atmospheric pressure boiling. For the present study,

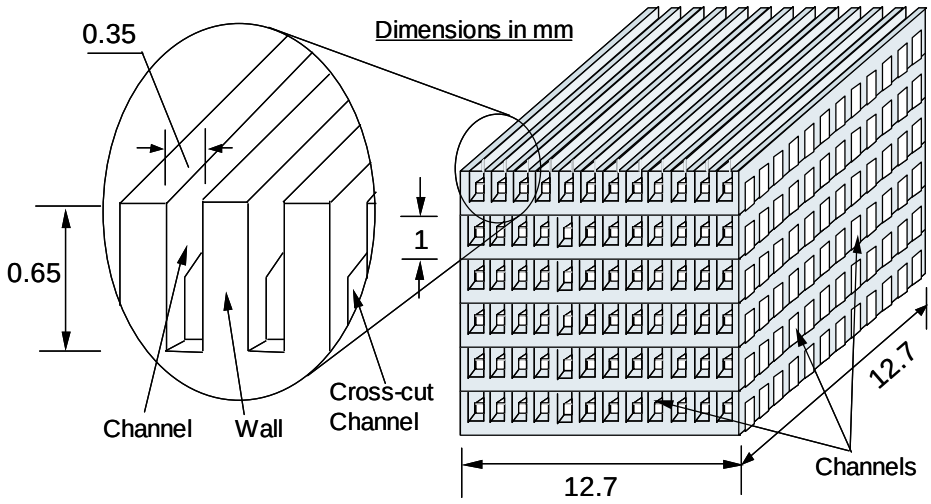

Figure 9: Detailed sketch of the enhanced structure with stacked multiple layers (6 layers shown)

four different geometries of the structure were considered - 1 layer, 2 layers, 4 layers and 6 layers.

2.1.2 Condenser Section

The evaporator and the heating block assembly were connected to a aluminum fin-tube single-pass condenser (140 fins) with copper tubing. Figure 10 shows the condenser location in the experimental setup, with transparent tubing (used during trial experiments). The fins were 50 mm × 25 mm (height × width) in dimension, with a gap of approximately 5 mm between a pair of fins. The inner diameter of the condenser tube was 4.25 mm and the wall thickness was 1 mm. The condenser was kept above the evaporator and the height between the plain boiling surface (flush with the bottom of the evaporator cavity) and the centerline of the inlet to the condenser was approximately 180 mm. The condenser tube is slanted downwards from the inlet to the outlet to allow gravity-assisted drainage of the condensate. The size of the condenser was sufficient for rejecting heat loads in excess of 180 W (the highest heat load tested). The heat transfer from the condenser to the ambient was controlled

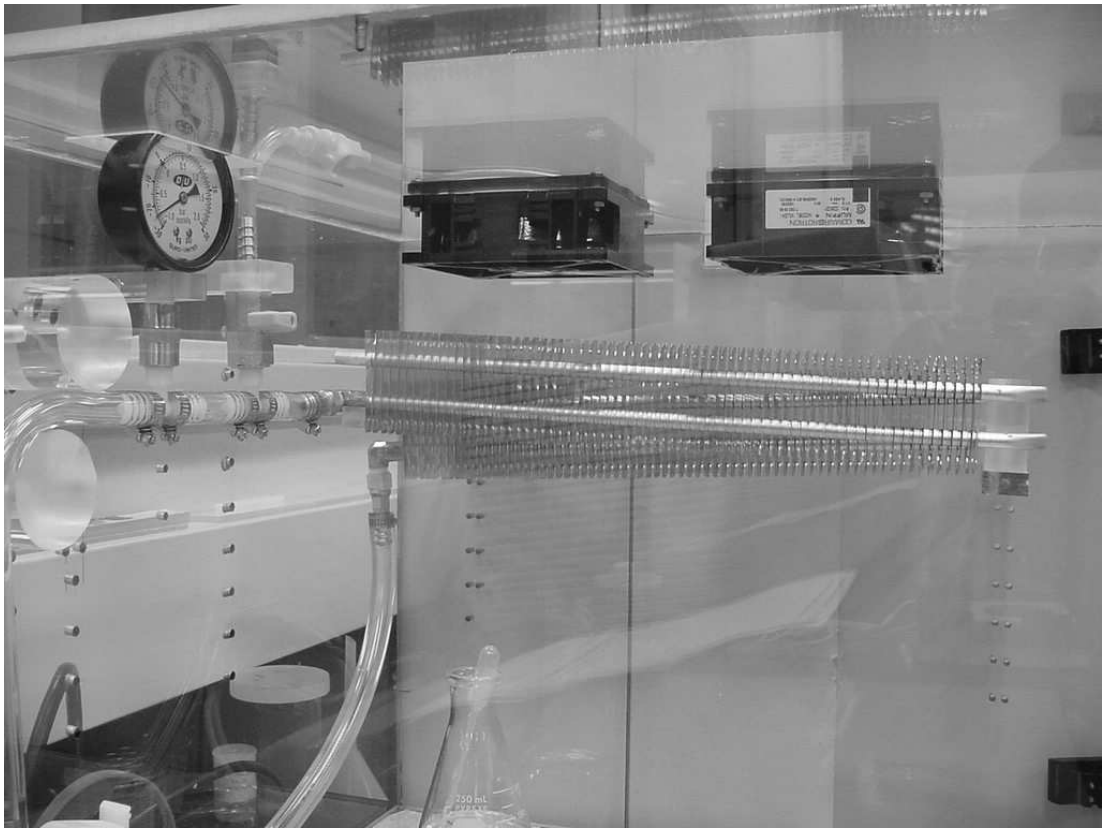

Figure 10: Location of condenser in the experimental setup

throughout each experimental run for maintaining a constant saturation condition inside the evaporator. At low heat fluxes, the condenser was kept covered with foam insulation. With increase in heat flux, the covered area was decreased and beyond 100 W, the condenser was totally exposed. Forced air cooling (using two fans, as shown in Figure 10) was sufficient to cool the condenser till 150 W. Beyond 150 W, evaporative cooling was employed (water droplets dripping on the condenser tube with air blown from the fans, not shown in Figure 10). The combination of foam insulation, forced air and evaporative cooling helped in maintaining a constant saturation temperature in the evaporator throughout the entire heat flux range for each experimental run.

2.2 Experimental Procedure

Great care was taken to ensure that the setup was leak proof over a long period of time. Leakage test was done by evacuating the thermosyphon to 2 kPa pressure, then closing the system valve and leaving the setup at idle condition at room temperature for a 24 hour period. After one day, the system pressure increase was found to be negligible ($\sim$0.1-0.2 kPa), which was considered as an acceptable amount of pressure loss, as the running time for all the experimental runs for a particular set of pressure-structure geometry was typically 2-3 hours. After each experimental run, the system was allowed to cool down for 2 hours; after that time, the pressure inside the system returned back to the initial pressure at the beginning of the experiment, which also showed that the setup was leak-proof.

Repeatability of measured data was checked for boiling with single-layer structure at 9.7, 15 and 21 kPa. The experimental data was found to be within a maximum variation of 5% of the baseline data. It was observed that leak-proof setup achieved excellent repeatability of data from experiment to experiment with same set of parameters.

Every experimental run was preceded by a degassing operation of the working

fluid. The degassing was done in a separate setup. The evaporator chamber for the degassing operation was similar in construction to the one used in the experimental runs and was connected to a spiral tube reflux condenser through a quick coupling (valved) connection. Vigorous boiling was initiated in the degassing chamber by supplying a heat input of around 80 W for about 1 hour. During boiling, the reflux condenser was cooled by ice-cold water to trap the vapor from the expelled gas mixture. The condensed liquid returned back to the evaporator due to gravity. After completion of boiling, the degassing chamber was disconnected from the reflux condenser by releasing the quick coupling. The liquid was allowed to cool for more than 2 hours. The degassed liquid reached room temperature by that time.

After the degassing procedure, the thermosyphon was evacuated to 2 kPa pressure (traces of water inside the system didn't allow the pressure to go lower than 2 kPa), followed by closing of the system valve. Next, the chamber containing the degassed liquid was connected to the system valve of the thermosyphon. Then the system valve of the setup was opened and the thermosyphon was charged with water till the chamber was filled to the desired liquid level corresponding to the experiment. The pressure difference (99 kPa) between the degassing chamber (atmospheric pressure) and the thermosyphon allowed the degassed water to flow from the degassing chamber to the thermosyphon. Because of pressure equalization during the charging procedure, the pressure inside the thermosyphon increased slightly during charging. After charging, the system valve was closed and the degassing chamber was disconnected from the valve. Then the vacuum pump was connected to the system valve and by opening the valve, the thermosyphon was evacuated again to a pressure of 2.5 kPa. After the evacuation, the system valve was closed and thermosyphon was ready for the start of experiments. Foam insulation was applied over the evaporator, the condenser and the tubing before starting the heat input to the system.

Before the start of the experiments, the desired saturation temperature in the

evaporator was attained by raising the liquid temperature with the help of a thermo-foil heater, wrapped around the evaporator chamber. The existence of saturation condition inside the system was checked with the correspondence between the temperature and pressure measured at a particular point in the loop (Figure 5). After the saturation temperature was reached in the evaporator, the experiments were started with initial heat input of 2 W and incremented in steps of 2 W till 10 W, then 10-20 W in steps of 5 W, 20-50 W in steps of 10 W, 50-150 W in steps of 20 W, and beyond 150 W in steps of 10 W to a maximum of 180 W. Around 15-17 runs were performed during boiling at each system pressure, unless critical heat flux (CHF) was encountered or the highest temperature recorded in the copper block reached 140 ^oC. The CHF condition was defined by a temperature rise of 20 ^{o}C in 20 s of the top-most thermocouple in the heater block. The choice of 140 ^{o}C was dictated by the thermal property of the polycarbonate in the heater block housing, parts of which began to melt around 140 ^{o}C. After reaching the limiting condition, the power input to the system was slowly decreased to 0 V and the system was allowed to cool down and the system was allowed to cool down till system pressure reached an equilibrium condition with the ambient temperature. The heat flux at the onset of CHF was noted for each case.

Temperatures were recorded every 3 s throughout the running time of each experimental run. Steady state at a particular heat flux was defined by a variation of less than ± 0.3 ^{o}C of the heater block temperatures about a steady mean value. After the system had reached steady state, the parameters were recorded and the analysis was done with the data recorded in the last 120 s.

A listing of the system parameters for the experiments is given in Table 4.

Table 4: System Operating and Geometrical Parameters

Parameter	Values
Vapor pressure	9.7 kPa, 15 kPa, 21 kPa
Liquid fill height	20 mm, 29 mm, 39 mm
Structure height	0 mm, 1 mm, 2 mm, 4 mm and 6 mm

2.3 Data Acquisition

Data acquisition consisted of monitoring the temperature and pressure inside the thermosyphon and power input to the heater. The measurements were carried out using a computerized data acquisition system. The system consisted of an Agilent 34970A Data Acquisition switch unit, which can house up to three individual Agilent 34901A 20 channel multiplexer modules. The thermocouples and the electrical wires were fed into a multiplexer module. The switch unit converts the multiplexed analog signal from the module to a digital signal and sent the signal through a GPIB cable to a Agilent 82350A PCI-GPIB interface card housed in a PCI port of a Pentium 2.8 GHz PC.

The signal received from the switch unit was displayed in the computer with the help of Agilent Benchlink software. The sampling rate for the temperature readings was 300 per second, per channel and 900 samples were averaged per channel for one temperature reading. This resulted in one averaged temperature reading every three seconds per thermocouple. A 20 Hz filter is used on the channels measuring AC voltage to optimize the AC measurement accuracy corresponding to the frequency of the supplied voltage.

The voltage and current input to the system were measured with the data acquisition system. The current input to the heater was obtained by measuring the voltage drop across a precision resistor (1 $\Omega \pm 0.01\ \Omega$) placed in series with the heater. The output from the pressure gauge was in mA, which was converted to

absolute pressure using a linear scale for the full range of the gauge output.

2.4 Uncertainty Analysis

The maximum uncertainty in the electrical heat input was ±1%. The precision resistor used to measure the current in the circuit was accurate to 1%. The thermocouples and the data acquisition system were calibrated with respect to a resistance temperature device (RTD) probe calibration system at five different temperatures (20 ^{o}C, 40 ^{o}C, 60 ^{o}C, 80 ^{o}C and 100 ^{o}C) to a maximum uncertainty of 0.1 ^{o}C. Heat flux through the test surface was determined through a combination of electrical and thermal measurements. Eight type-T thermocouples were spaced at distances of 7 mm, 9.9 mm, 13 mm, 16 mm, 19.5 mm, 23 mm, 27 mm and 31 mm from the test surface to measure the temperatures and help in calculating the heat flux through the surface. The tip of the thermocouple probes were kept in contact with the bottom of the probe holes before epoxy was applied to attach the probes to the holes, to reduce the thermal contact resistance at probe contact points. A numerical heat conduction model showed that the heat flow through the copper rod could be assumed to be one-dimensional with reasonable accuracy. So, the heat flux at the test surface was obtained by calculating the slope of a fitted line through the thermocouple measurements. The power input to the system was obtained by the product of the voltage drop across the cartridge heater and the current flow through the precision resistor. The difference between the heat flux calculated from temperature measurements and the electrical heat input was less than 5% at higher heat fluxes (> 20 W/cm^2). This was largely attributed to the uncertainty in the location of the thermocouples. The measurements at very low heat fluxes (< 5 W/cm^2) showed a larger scatter (maximum of 20%), which produced slightly higher uncertainty in the heat flux measurement. The uncertainty in the heat flux measured from the electrical data was ±10.0% (see Appendix A). The corresponding uncertainty

in the wall temperature measurement was about ± 0.5 ^{o}C. The vapor pressure in the evaporator was obtained from NIST data, corresponding to the temperature in the vapor zone. The variation in the temperature of the vapor zone was less than 0.5 ^{o}C, while the pressure measured by the transmitter showed a variation of less than 10%, based on the theoretically predicted saturation temperature compared to the measured temperature at that location.

2.5 Summary

In this chapter, the details of the experimental setup were discussed. The important components of the experimental setup were identified and their fabrication and assembly details were described. This was followed by a description of the data acquisition system, in which the arrangement of the various components of the system along with the specific settings required for measuring some of the parameters were discussed. A step-by-step procedure for the execution of the experiments followed next, which was succeeded by a tabular representation of the different values of the thermosyphon design parameters investigated in the present study. Finally, the measurement techniques employed for monitoring the various parameters was discussed.

CHAPTER III

EFFECT OF PRESSURE AND ENHANCEMENT STRUCTURE ON THERMOSYPHON PERFORMANCE

The effect of pressure and enhancement structure on the thermosyphon performance will be discussed in the present chapter. All the experiments were done by increasing heat flux until either the inception of CHF condition or the highest temperature recorded by the thermocouples embedded in the copper heater exceeding 140 ^{o}C. The air-side thermal resistance of the condenser also limited the system heat rejection, and the maximum heat flux that could be applied to the structure. The liquid level was kept at 39 mm from the boiling surface in all the runs, which represented a full-fill condition of the evaporator. The boiling curves are shown on linear scale as the variation of heat flux with respect to the wall superheat.

All the experiments were done at increasing heat flux conditions. Trial runs were performed with decreasing heat fluxes for some pressure-structure geometry combination, which produced similar boiling curves with respect to increasing heat flux cases, with a a maximum variation of 5% for heat fluxes greater than 20 W/cm^2. Similar to the present study, Nakayama et al. [27] found that hysteretic behavior is less pronounced for boiling with enhancement structures.

3.1 Baseline Study

Boiling at sub-atmospheric pressures was first studied with an emery polished plain copper surface of dimension 12.7 mm $\times$ 12.7 mm at pressures of 9.7 kPa, 15 kPa and 21 kPa, with a full-fill (liquid height = 39 mm) condition. From visual observation, it was found that intermittent bubbles were generating from the surface at long intervals

during the initial stages of power input (2-6 W/cm^2), which changed to fully developed boiling at approximately 12 W/cm^2. By that time, the liquid pool was fully agitated from large sized bubbles generating from the plain surface. Beyond 55 W/cm^2, the power input was gradually increased in steps of 3 W/cm^2, until it reached the desired power, at which temperatures were recorded. This was done to closely monitor the point at which CHF was initiated.

Figure 11 shows the resulting boiling curves at the pressures of 9.7 kPa, 15 kPa and 21 kPa. Data from McGillis et al. [25] and Latsch et al. [23], as well as the boiling curve of FC-72 (nucleate boiling zone only) derived from the correlation developed by Rainey et al. [26] are also shown for comparison. The improvement in heat transfer obtained with boiling of water with respect to FC-72 is clearly evident. At 80 W/cm^2 the wall superheat for water was around 20 ^{o}C compared to 55 ^{o}C for FC-72. Existence of incipience superheat is a common phenomenon in boiling of dielectric liquids before the start of nucleate boiling (Rainey et al. [26], Anderson and Mudawar [31], Ramaswamy et al. [33]), and is found to depend on the saturation pressure. However, the present study shows that saturation pressure has negligible effect on the incipience superheat in boiling of water. Gebhart and Wright [57, 58] noticed a similar absence of incipience in boiling of water with micro-configured surfaces and suggested the existence of early incipience and micro-boiling from the observations. Moreover, water is less wetting on copper surfaces compared to dielectric liquids, which also led to negligible incipience superheat noticed in the current study. However, McGillis et al. [25] noticed wall superheats in excess of 5 ^{o}C in their study on boiling of water from a plain surface of dimensions 12.7 mm $\times$ 12.7 mm (the results at 9 kPa are shown in Figure 11). It is to be noted that the evaporator chamber of McGillis et al. [25] was not insulated. Due to heat loss from the evaporator wall, a large wall superheat was required to reach saturated conditions at 9 kPa. This is markedly different from the present study, where the heat loss from the evaporator

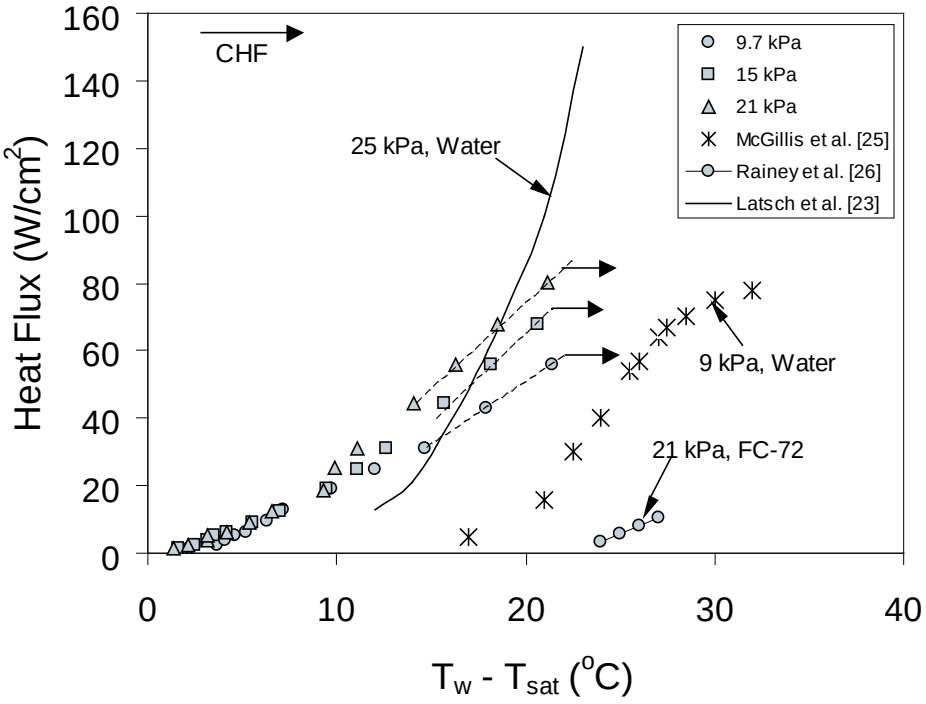

Figure 11: Boiling curve for water on a plain surface at full-fill level in the evaporator

wall was compensated with a guard heater, which kept the bulk liquid temperature close to the saturation temperature. As a result, the wall superheat was very low during the initial stages of boiling (compared to McGillis et al. [25]). The effect of pressure is clearly evident, as the heat flux capability is considerably decreased with a reduction in saturation pressure. However, the effect of pressure is not noticed below 20 W/cm^2. Beyond 20 W/cm^2, the boiling curves show linear behavior until CHF is reached. Van Stralen [17] observed a similar decrease in the maximum heat flux with decrease in pressure, which was attributed to the larger size of bubbles generating from the heating surface. Joudi and James [21] observed a reduction in the number of bubbles generated from the boiling surface at reduced pressures. Fath and Judd [22] observed similar increase in heat flux with increase in system pressure, though their experiments were with dichloromethane. Bubble generation frequency increased with increase in pressure. Other studies, which corroborate the above observations, are of Tewary et al. [24], Latsch et al. [23] and Gorodov et al. [59]. However, the decrease in

the heat flux is offset by the reduction in saturation temperature inside the evaporator chamber with decrease in saturation pressure. This is particularly interesting for electronics cooling applications, as very low surface temperature can be obtained in these conditions. The maximum wall temperature recorded for the pressures of 9.7 kPa, 15 kPa and 21 kPa were 68 ^{o}C, 76 ^{o}C and 83 ^{o}C respectively.

Critical heat flux (CHF) was reached for all the cases under consideration. For 9.7 kPa, the CHF was 62 W/cm^2, while for 15 kPa and 21 kPa it was 78 W/cm^2 and 87 W/cm^2 respectively. However, McGillis et al. [25] obtained a higher CHF ($>$ 80 W/cm^2) at 9 kPa from a plain copper surface. As discussed above, the absence of insulation in the evaporator chamber can explain the high CHF obtained with respect to the present study. Because of heat transfer through the evaporator wall, the effective heat transfer coefficient in the evaporator was much higher in their case, which resulted in higher CHF than that observed in the present study. In this respect, it is believed that the current study documents a more controlled investigation of boiling at sub-atmospheric pressures. A recent study by Pal and Joshi [60] has shown that the CHF can be increased in sub-atmospheric pressure boiling of water by lowering the effective liquid level in the evaporator. The liquid level in the case of McGillis et al. [25] was much lower than the present study, which might also explain the higher CHF obtained by them.

In Figure 12 a comparison of the CHF values with respect to existing correlations is shown. The experimental results of Ponter and Haigh [18] match the predictions of the Lienhard and Dhir [61] correlation very closely. The CHF values of the present study are higher by a factor in the range of 1.1-1.3 with respect to the CHF values obtained from Lienhard and Dhir's correlation [61]. However, the CHF values of the present study are within 20-25% of the correlation values, which is close to range of scatter ($\pm$20%) as suggested by Carey [38]. The correlation of Lienhard and Dhir [61] applies to boiling from plain surfaces in motionless liquid. The current results are for

experiments in which liquid from the condenser was swept over the boiling surface, which might be responsible for the improvement of CHF values. Moreover, the high liquid column height (76 mm) used by Ponter and Haigh [18] might also lead to lower CHF values, following the observations of Pal and Joshi [60].

With decrease in the operating pressure, the density of the vapor decreases. As a result, the bubble sizes during boiling at low pressure are larger compared to boiling at atmospheric pressures. Visual observation during degassing showed that the bubbles are dislodged from the surface at a slower rate than boiling from a plain surface at atmospheric pressure. Miyauchi and Yokura [19] observed similar suppressed bubble growth rates at sub-atmospheric pressures. According to them, a rapidly growing bubble will accelerate the liquid surrounding it, which will induce a pressure increase inside the bubble. It was hypothesized that the increase in pressure will increase the saturation temperature and will lead to higher wall superheats, leading to suppressed bubble growth rates. Moreover, the larger size of the bubbles might also inhibit the growth of bubbles from neighboring sites, leading to bubble generation from some preferred sites. This might lead to fluctuations in temperature in the boiling surface. An interesting finding in this respect was by Joudi and James [21], which focused on the surface temperature during the initial boiling stages. They found that the surface temperature was not uniform across the boiling surface or steady at a particular location. In the current experiments, surface temperature fluctuations were not recorded, instead average surface temperatures obtained from the linear fit of the copper block temperature measurements were used to report the boiling data.

3.2 Effect of Pressure

The present section will describe the study on various enhancement structures at the pressures of 9.7 kPa, 15 kPa and 21 kPa and compare the results with the baseline study reported earlier. Four boiling enhancement structures were used, which have

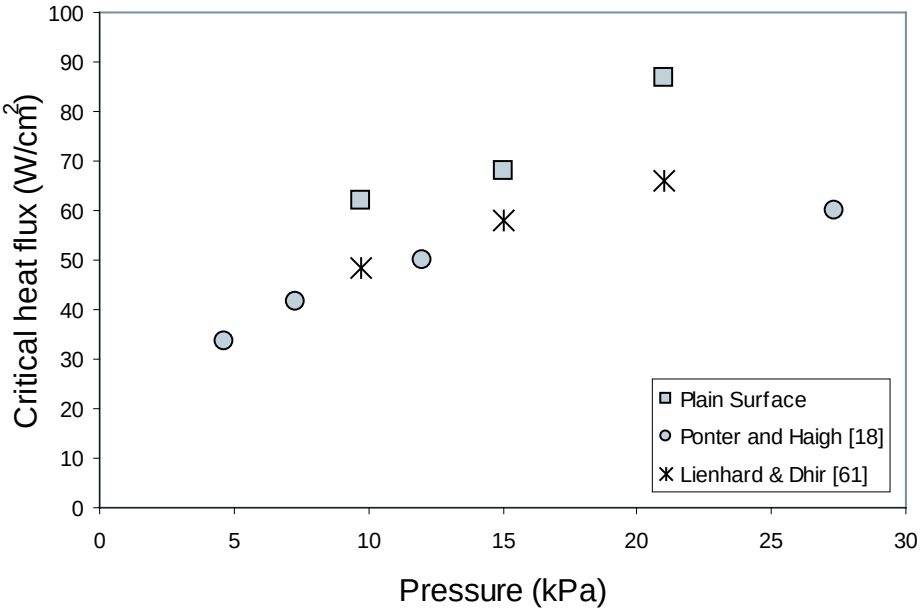

Figure 12: Comparison of CHF values for boiling with plain surface

different numbers of stacked layers - 1, 2, 4 and 6, with geometries as described earlier. The experiments described in this section were done at full-fill level for all the pressures and the different enhancement structure geometries.

In Figure 13, the effect of pressure on the saturated nucleate boiling curves is compared between the single layer enhanced structure and the plain surface. The results from McGillis et al. [25] at 9 kPa are also shown for comparison. Both the studies employed the footprint area of the boiling structure (stacked porous structure of the present study and finned-structure of McGillis et al. [25]) as the base area in obtaining the heat flux. McGillis et al. [25] performed their experiments with finned structures, where the lowest gap between the fins was kept at 0.3 mm. This result is included for comparison, as the fin gap of 0.3 mm closely resembles the gap (0.35 mm) of the channels in the enhancement structure used in the present study. They found better performance with the lowest fin gap. As noticed in case of the plain surface, incipient superheat is not noted for the enhanced structure in the present study. This observation corroborates the results of Gebhart and Wright [57] mentioned previously. The wall superheat of 4 ^{o}C at 9 W/cm^2 observed by McGillis

et al. [25] agrees roughly with the wall superheat of 6.2 ^{o}C at 9.3 W/cm^2 observed in the present study. However, a significant difference is noted in the wall superheat at higher heat fluxes. Whereas, CHF was not reached in both the studies, a difference of approximately 13 ^{o}C was noted in the wall superheat at around 90 W/cm^2, with McGillis et al. [25] showing the lowest wall superheat. A possible explanation can be the configuration of the thermosyphon used in the two studies. McGillis et al. [25] used a single chamber thermosyphon, or "wickless heat pipe" configuration, where the condenser was placed directly above the evaporator and was an integral part with the evaporator cylinder. This allowed easy draining of the condensed liquid directly to the evaporator. In the present study, a dual chamber configuration of the thermosyphon was used, in which the condenser tube was inclined with respect to the horizontal. Condensed liquid drained from the condenser only when enough pressure gradient was generated in the condenser. As a result, the condenser was lined with liquid most of the time, which reduced the condensation heat transfer coefficient. Though a vertically oriented condenser will aid in draining the liquid quickly, its added size may be undesirable in compact microsystems.

The nucleate boiling curves for the 2, 4 and 6 layer enhancement structures are shown in Figure 14, 15 and 16 respectively. As for the single layer case, incipient superheat was absent in all the cases. An increase in the saturation pressure led to a corresponding increase in the saturation temperature, which was responsible for an increase in the wall temperature. This behavior was found to be consistent for all the structures tested. Moreover, for a particular structure, with increase in the wall heat flux, the wall temperature increased at a greater rate for 9.7 kPa compared to 21 kPa. This behavior is more apparent at higher heat fluxes ($>$ 60 W/cm^2). For the single layer structure at 9.7 kPa, the wall temperature increased by 15 ^{o}C (24%) as the heat flux increased from 60 W/cm^2 to 100 W/cm^2, while the increase was 8 ^{o}C (12%) and 6 ^{o}C (8%) for 15 kPa and 21 kPa respectively. The effect of pressure at a

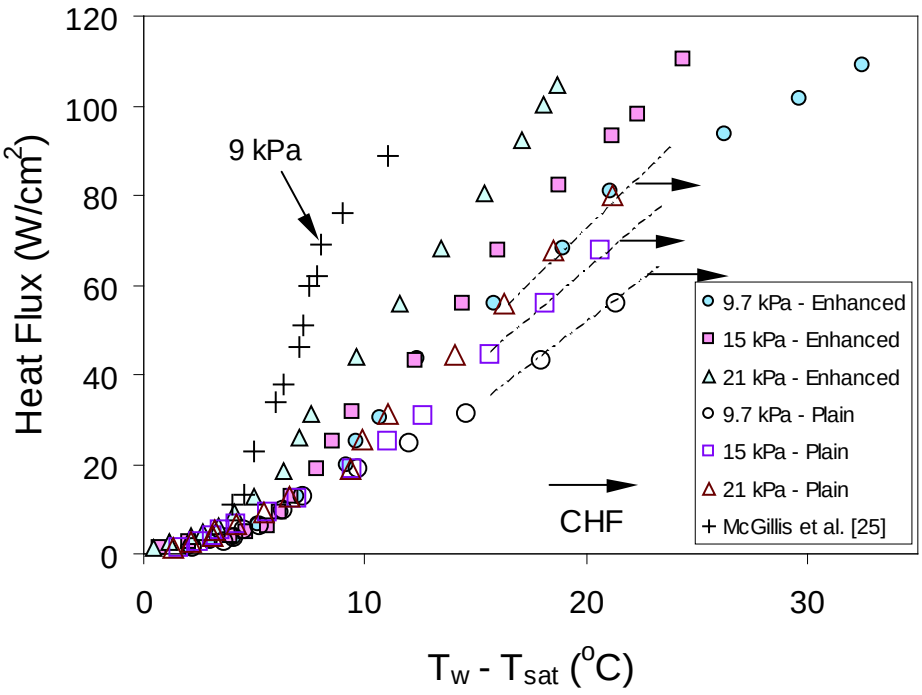

Figure 13: Effect of pressure on enhanced single layer structure and plain surface

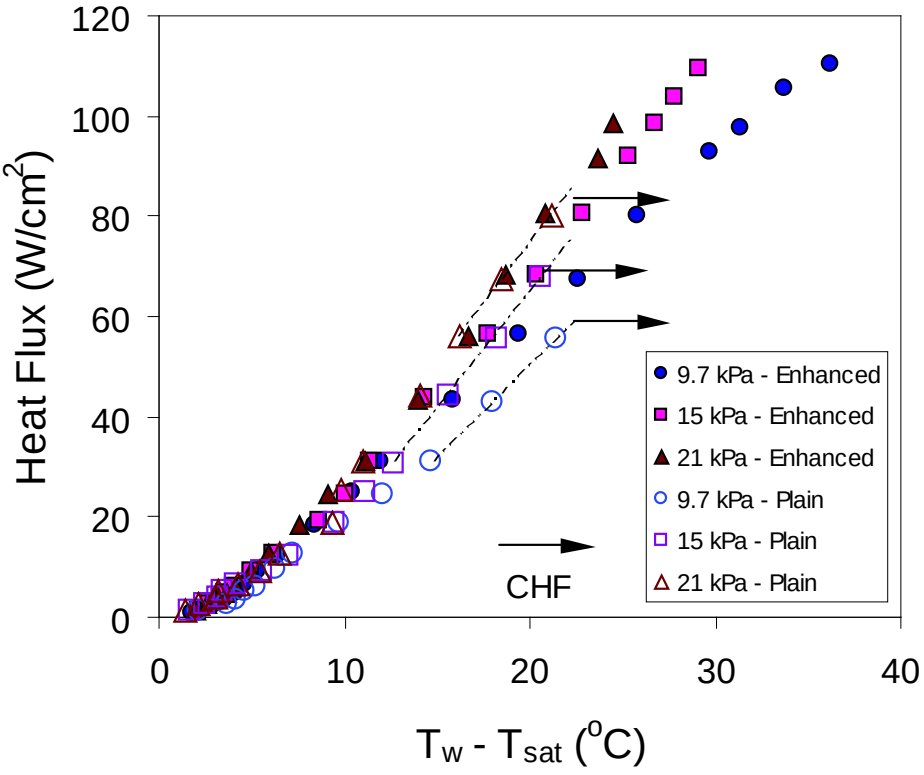

Figure 14: Effect of pressure on enhanced double layer structure and plain surface

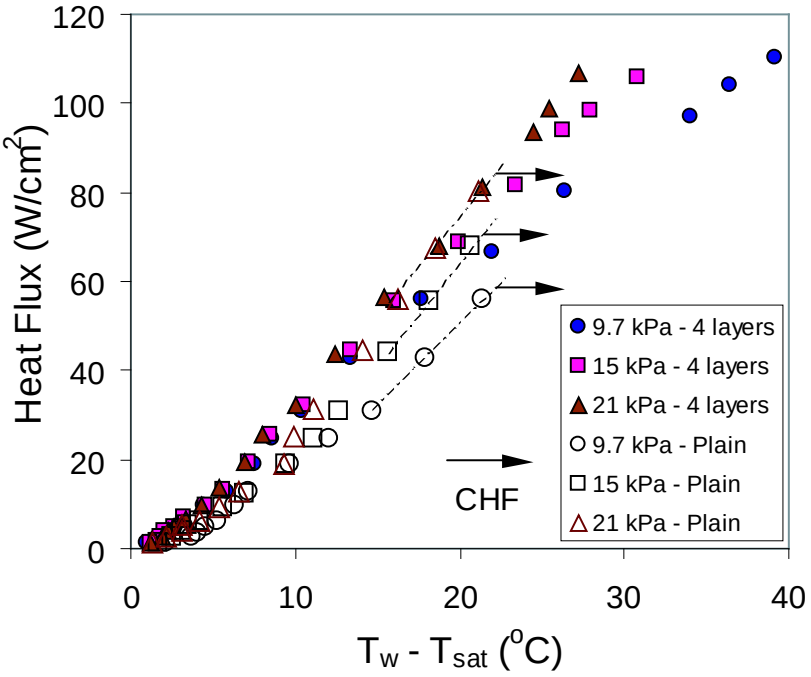

Figure 15: Effect of pressure on enhanced 4-layer structure and plain surface

particular heat flux is also apparent. For the single-layer structure at 60 W/cm^2, the wall temperature increased by 11 ^{o}C (24% increase) from 9.7 kPa to 21 kPa. With increase in heat flux to 80 W/cm^2, the difference dropped slightly to 10 ^{o}C (15% increase), while for 100 W/cm^2, the difference dropped sharply to 4 ^{o}C (8% increase). This shows that increasing saturation pressure at a particular heat flux will result in a smaller change of wall temperature. Similar trends were seen for the other structures too. This behavior can be better understood by observing the variation of heat transfer coefficient with wall superheat for single-layer structure shown in Figure 17. A significant trend of decrease in heat transfer coefficient with decrease in pressure is noticed. For 9.7 kPa, the heat transfer coefficient increases monotonically until a wall superheat of 15 ^{o}C, then slowing until 20 ^{o}C and reducing beyond that. It is interesting to note the existence of maximum heat transfer coefficient for the 9.7 kPa and 15 kPa cases. However, the heat transfer coefficient for 21 kPa increases rapidly until 10 ^{o}C and with a slightly slower rate subsequently. The bubble generation phenomena may provide an explanation for worse thermal performance at 9.7 kPa. At lower pressures,

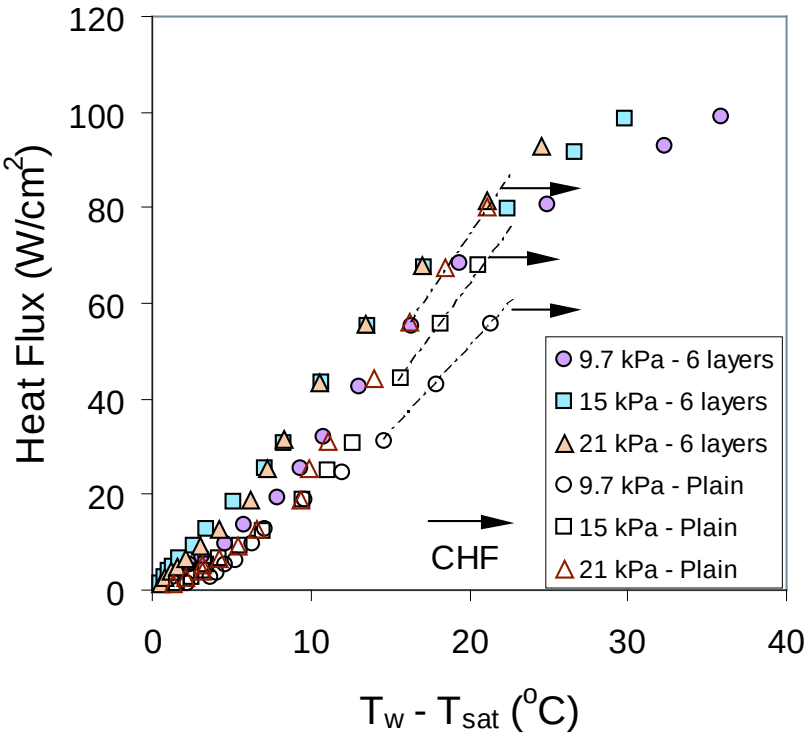

Figure 16: Effect of pressure on enhanced 6-layer structure and plain surface

the bubble sizes are large, preventing the liquid from coming in contact with the boiling surface and a resulting decrease in heat transfer coefficient. The current configuration of the boiling enhancement structure also generates bubbles from the vertical side-walls, which add to the turbulence in the pool. So the reduction in boiling surface temperatures obtained by operating the thermosyphon at low pressures is offset by the deteriorating heat transfer coefficient.

3.3 Effect of Enhancement Structure

We can see clearly from Tables 5 and 6, that the enhancement structures were able to dissipate high heat fluxes, while keeping surface temperatures very close to the threshold value of 85 ^{o}C (desired in electronics cooling applications). However, the performance became worse at 100 W/cm^2 for structures having more than 2 layers. The CHF was not reached for the enhancement structure geometries until the end of the experimental steps (usually 100 W/cm^2). A general trend is noticed towards

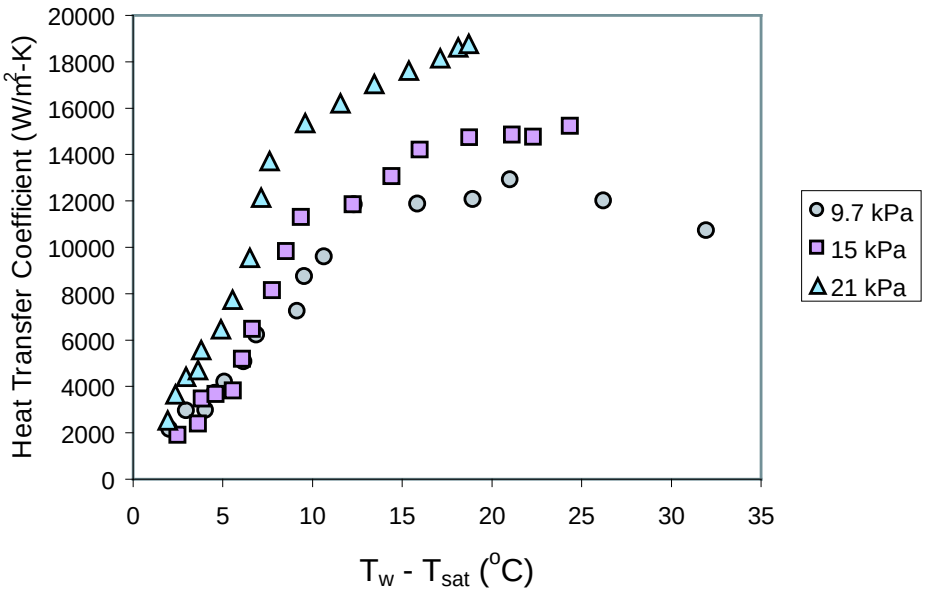

Figure 17: Heat transfer coefficient as a function of wall superheat for single-layer structure

increase in wall superheat with increase in the number of layers of the structure, which relates to a decrease in heat transfer coefficient. This trend can be noticed in Figure 18, where the effect of the stack height on the heat transfer coefficient, h, at 9.7 kPa is shown, where:

$$h_{ave} = \frac{Q'}{A_s} \cdot \Delta T \tag{1}$$

where, Q' is the heat dissipation, A_s is the surface area of the structure exposed to liquid and ΔT is the wall superheat ($= T_w$ - T_{sat}). The superior performance of the single layer structure is evident from the comparison. For the single layer structure, the heat transfer coefficient increases monotonically at low wall superheat, then slowing down in between 10 ^{o}C - 20 ^{o}C and finally decreasing monotonically at higher wall superheats. Visual observation showed that at low wall superheats, the bubbles emerged from some preferred spots, however at higher wall superheats, the bubble generation resembled that of fully developed boiling. The generation of bubbles affected the liquid movement close to the boiling structure. So at higher heat fluxes, vigorous bubble generation decreased the liquid supply close to the structure,

which decreased the heat transfer coefficient. Ramaswamy et al. [62] observed similar behavior for boiling with a single layer structure of similar geometry, using PF5060 as the working fluid. Compared to the single layer structure, the 2, 4 and 6 layer structures show a weaker change in heat transfer coefficient with wall superheat and achieve lower values of heat transfer coefficients. Increase in the stack height is also seen to limit the maximum value of the heat transfer coefficient. This implies that there exists a certain stack height, which will produce the maximum heat transfer coefficient for a particular saturation pressure. McGillis et al. [25] also observed similar optimum height with finned structures, and found that the heat transfer was insensitive to fin height beyond a certain fin height. In the current study, however, the heat transfer was influenced by the height of the structure. Following from the above discussion, this behavior can be attributed to the bubble generation dynamics from the enhancement structure used in the present study.

Table 5: Wall temperatures recorded at 80 W/cm^2

Pressure	1 layer		2 layers		4 layers		6 layers	
(kPa)	T_w	ΔT	T_w	ΔT	T_w	ΔT	T_w	ΔT
9.7	68	21.7	72	25.7	72	25.7	72	25.7
15	73	18	78	23	78	23	78	23
21	78	15.5	84	21.5	84	21.5	84	21.5

$\Delta T = T_w$ - T_{sat}, T_w and T_{sat} are in ^oC

Table 6: Wall temperatures recorded at 100 W/cm^2

Pressure	1 layer		2 layers		4 layers		6 layers	
(kPa)	T_w	ΔT	T_w	ΔT	T_w	ΔT	T_w	ΔT
9.7	77	30.7	79	32.7	82	35.7	83	36.7
15	77	22	82	27	83	28	85	30
21	81	18.5	87	24.5	89	26.5	90	27.5

$\Delta T = T_w$ - T_{sat}, T_w and T_{sat} are in ^oC

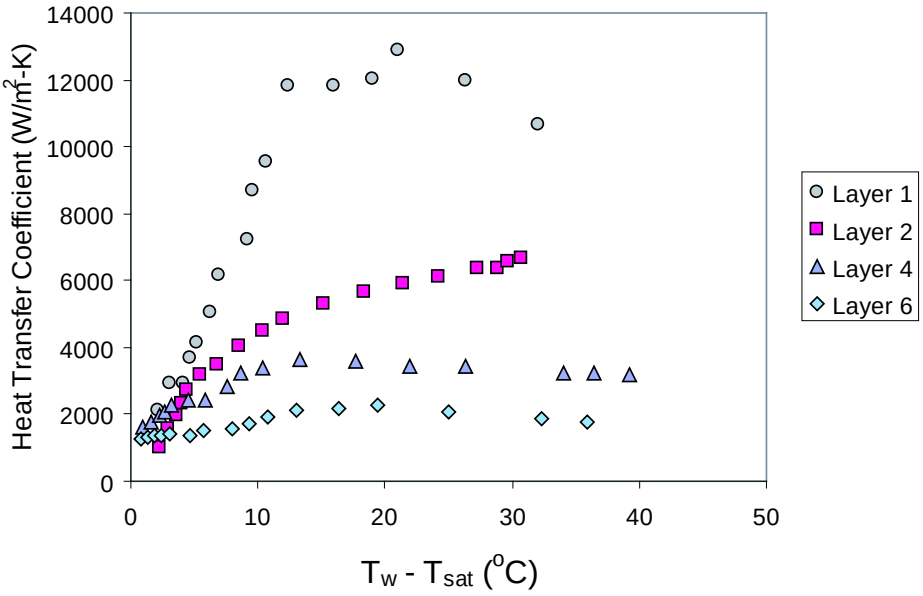

Figure 18: Heat transfer coefficient vs. wall superheat at 9.7 kPa for all layers

Increasing the number of layers increases the convection heat transfer area, however, due to the conduction thermal resistance encountered in the stack, it is hypothesized that the temperature of the top layer will be less than the base temperature, potentially resulting in a decrease in heat transfer coefficient. A similar observation was also noted by Ramaswamy and co-workers [62, 33] in their studies with dielectric fluids. Using FC-72 as the working fluid, Nakayama et al. [63] noted that for higher heat fluxes (> 15 W/cm^2), the boiling curves of porous structures closely resembled that of plain surfaces. They attributed the deterioration in heat transfer coefficient with increase in stack height of the porous structures to the "dried-up" mode of boiling. In a recent study with PF5060, Ghiu and Joshi [64] didn't observe any decrease in performance due to the "dried-up" mode, however, the maximum heat flux for their study was 35 W/cm^2. In the present study, experiments were performed beyond 100 W/cm^2, where vigorous bubble generation was observed. Moreover, compared to dielectric liquids, water has higher surface tension, so it has less wetting characteristic. Due to increased bubble generation from the side-walls (with increasing stack height) and top surface of the structure, and increased surface

tension of water, there will be less liquid coming in contact with the porous structure, which would decrease the overall heat transfer from the structure. In this regard, the current results corroborates with the previous observations of Nakayama et al. [63].

3.4 Fin Model

The enhanced structure was modeled as a fin with specified heat transfer coefficient. The following additional assumptions were made:

- Heat losses from the sides of the chamber were considered negligible.
- Uniform heat flux was assumed from the heater surface.
- The heat transfer coefficient was obtained by considering the exposed surface of the structure to be at the wall temperature.
- Uniform heat transfer coefficient was assumed over the entire exposed surface of the boiling structure.

Three-dimensional steady heat conduction was solved for the configuration shown in Figure 19, using the following boundary conditions:

Input heat flux :

$$q''_{heater} = \frac{Q'}{A_s} \tag{2}$$

Convective heat transfer:

$$k_{copper} \left.\frac{\partial T}{\partial z}\right|_s = h_{ave,ex} \left(T_{sat} - T_s\right) \tag{3}$$

where, Q' is the input power to the system, A_s is the heater surface area, which was in contact with the copper block, $h_{ave,ex}$ is the average heat transfer coefficient at the exposed surfaces of the enhanced structure (obtained from the experimental results), T_{sat} is the saturation temperature of the working fluid and T_s is the temperature at the surfaces of the enhanced structure. The solution procedure involved solving the

temperature profile throughout the assembly and then obtaining the heat flux from the base of the structure. The commercial multi-physics software package CFD-ACE+ was used to solve the temperature profile of the assembly. The q''_{heater} vs. ΔT curves for layers 1, 4 and 6 obtained from the numerical simulation are shown in Figure 20, alongside experimental data. The trends of the predicted q''_{heater} vs. ΔT curves match closely with that of the experimental results, which shows that the numerical simulation predicted the enhancement obtained from the structures. However, the numerical simulation over-predicted the surface heat flux by approximately 5% at the higher heat fluxes. One of the reasons for this over-prediction might be the assumption of uniform heat transfer coefficient throughout the exposed surface of the enhancement structure. Moreover, adiabatic conditions were assumed for all the side-walls and the bottom walls of the assembled structure shown in Figure 19. In reality, some amount of heat loss will occur through the sidewalls, which will reduce the actual heat flux through the boiling surface. Ramaswamy et al. [62] performed a two-dimensional analysis of the heat transfer through the enhanced structures using a finite volume approach. Their predicted surface heat flux values had a minimum of 10% variation with respect to their experimental results. A more realistic three-dimensional analysis in this study might be responsible for the better agreement between predicted and experimental results. This study shows that the fin-effect of the enhancement structures cannot be neglected. The combined effect of the fin-like structures and the boiling phenomena from stacked porous structures might be responsible for the observed reduction in heat transfer coefficient with increase in the layers of the enhancement structure.

Increasing the layers of the structures also affects the flow field inside the evaporator, which might also explain the deterioration of heat transfer for higher stack heights. A tall structure would create a barrier to the flow coming from the inlet. During boiling, such a structure would also generate more bubbles from the sides,

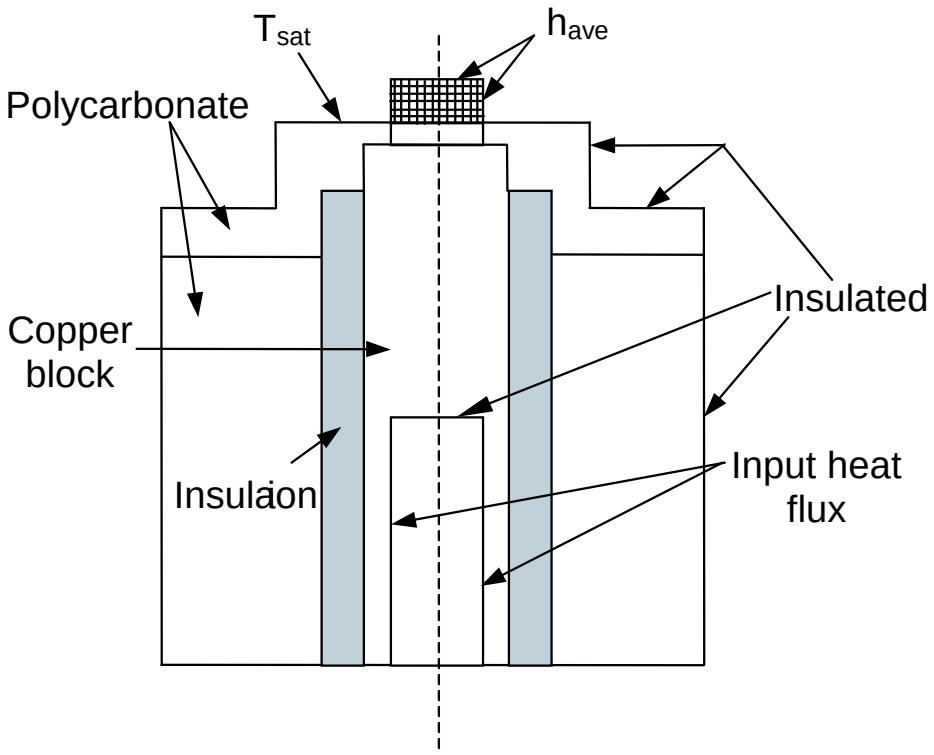

Figure 19: Model configuration for calculation of wall heat flux with enhanced structures

which would create a sweeping motion and would create resistance to the incoming liquid from coming in contact with the structure. Structures with lower heights would provide smaller resistance to the incoming flow. The top-side of the structure would be the main contributor to heat dissipation. Haider et al. [16] performed a numerical study of flow and heat transfer of a closed loop thermosyphon and observed that the heat transfer phenomena in a similar thermospyhon configuration resembled flow boiling.

3.5 Discussion

As discussed previously, an optimum height of the structure might be able to produce the maximum heat flux for a particular system pressure. One of the evaporator design parameter, that might affect the height of the structure is the vertical location of the condensate-inlet port of the evaporator. Condensate entering the evaporator will

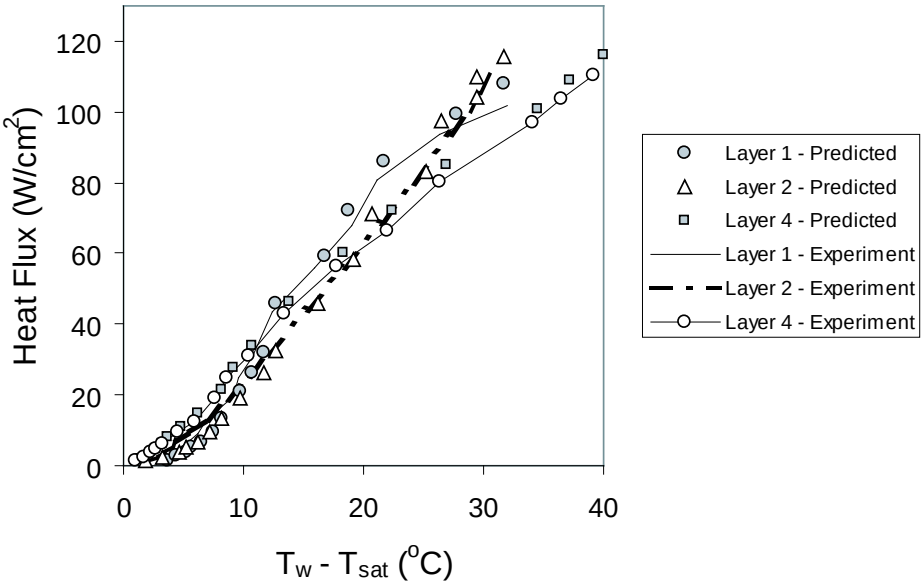

Figure 20: Effect of varying stack height on boiling heat transfer (comparison between experimental and numerically predicted results)

sweep away the bubbles and hot liquid from the faces of the structures close to the condensate inlet. The flow field of the condensate will change depending on the height of the structure and also the vertical height of the condensate inlet from the base of the evaporator cavity. A similar scenario has been described by Haider et al. [16] as "flow boiling" in their modeling of the flow and heat transfer in a dual chamber thermosyphon. Measurement of the condensate inlet velocity to the evaporator will ascertain whether the sweeping motion is tangible to affect the surface heat flux. In the current experimental study, the inlet velocity of the condensate to the evaporator was not measured. It is believed that the bubble generation from the sides of the structure

3.6 Summary

In this chapter, boiling of water at sub-atmospheric pressures in a thermosyphon, which employed enhancement structures was discussed. First the results of a baseline configuration was discussed, followed by results from boiling at various pressures and enhancement structure geometries. The relative importance of the structure geometry

and the system pressure on the thermal performance was discussed. The results were compared with existing correlations. A numerical simulation was performed on the heat transfer from the enhanced structure, whose results were used to compare the data obtained from experimental observations. The main conclusions of the study are as follows:

1. Boiling at sub-atmospheric pressures results in lowering of saturation temperature, which leads to lower wall temperatures. Heat fluxes greater than 100 W/cm^2 can be achieved through boiling at sub-atmospheric pressures, while keeping the surface temperatures below the threshold temperature of 85 ^oC.

2. Incipience superheat was found to be negligible for boiling at sub-atmospheric pressures with enhanced structures.

3. The heat transfer coefficient increased with an increase in the operating pressure. With increase in heat flux, the performance at lower pressure was worse compared to higher pressure.

4. The lowering of surface temperature with decrease in pressure is offset by the deterioration of heat flux with lowering of pressure. The bubble generation physics plays an important part in this scenario. In this respect, the current results corroborate previous investigations on boiling of water at low pressures, which concentrated on visualization of bubble generation at low pressures.

5. The enhancement structures were found to achieve increased heat flux and CHF with respect to boiling from a plain surface at sub-atmospheric pressures. The single layer structure achieved better heat flux than higher layer structures (2,4 and 6 layers). However, as the height of the structure was increased beyond single layer, the heat transfer coefficient reduced. The increased bubble generation from the sides of the higher layer structures is considered responsible

for preventing liquid from replenishing the interior pores of the structure and thus reduce surface heat flux. This implies the existence of an optimum height of the structure, which will allow replenishment of the pores of the structure with the working fluid, while achieving the maximum heat transfer corresponding to a particular saturation pressure.

6. With increase in the operating pressure, the enhancement in heat transfer achieved by the porous structure over the plain surface tends to decrease.

CHAPTER IV

EFFECT OF LIQUID FILL ON THE THERMOSYPHON PERFORMANCE

4.1 Experimental Procedure

For each boiling enhancement structure, three different liquid-fill levels were tested - 39 mm (Fill-1), 29 mm (Fill-2) and 20 mm (Fill-3), the height of the liquid column being measured from the base of the evaporator cavity at zero heat flux condition (Figure 7). Fill-1 represented a fully filled evaporator cavity, in which the gap between the top of the evaporator cavity and the top surface of the water layer was $\sim$2 mm. For each liquid-fill level, the thermosyphon was subjected to three pressures and the subsequent experimental runs were performed. Then the liquid was drained and the next structure was introduced to the system and the experimental runs were repeated for the range of pressure and liquid-fill volume. For fill-1 and fill-2 conditions, the experiments were started with an initial heat input of 2 W and then gradually increased by 2 W till 10 W, and subsequently followed the same incremental pattern as described earlier.

However, for the fill-3 experiments, the initial heat input was 10 W, as it was very difficult to maintain saturation temperature below 10 W of input power. It was observed that boiling didn't start at lower heat fluxes (< 6 W/cm^2), so the vapor generation was mostly through evaporation. Because of slow vapor generation rate at lower heat fluxes, the mass flow rate of vapor to the condenser was also low. The condensed liquid drained from the condenser periodically, which suggested that the liquid drained due to gravity only after reaching a critical buildup-volume. The condensed liquid drained periodically every 1-2 min at sub-cooled (23-25 ^{o}C)

conditions. As the volume of liquid in the evaporator at fill-3 was small, this might have reduced the bulk temperature of the liquid and consequently, the saturation temperature in the evaporator. Increasing the input power beyond 6 W/cm^2, boiling was initiated, which decreased the temperature fluctuations in the evaporator. So for the fill-3 experiments, the initial heat input was chosen as 10 W.

All the experiments were done at increasing heat flux conditions. Trial runs were performed with decreasing heat fluxes for some pressure-structure geometry combination, which produced similar boiling curves with respect to increasing heat flux cases, with a a maximum variation of 5% for heat fluxes greater than 20 W/cm^2. Similar to the present study, Nakayama et al. [27] found that hysteretic behavior is less pronounced for boiling with enhancement structures.

4.2 Baseline Study

A baseline set of experiments was performed to study the effect of liquid fill levels on boiling from a plain surface at sub-atmospheric pressures. Research on effect of liquid fill on boiling from a plain surface in a confined evaporator is nearly absent. The results from the baseline study will help in comparing the boiling performance of enhanced structures at similar liquid fill levels. The boiling curves for a plain surface at 9.7, 15 and 21 kPa pressures with fill-1, fill-2 and fill-3 levels are shown in Figure 21. The boiling curves for 9.7 kPa do not show a significant dependency on the liquid fill levels, however the inception of the CHF condition was delayed with a decrease in fill level. The influence of the fill levels are apparent for the cases of 15 and 21 kPa, where an increase in boiling performance was observed with a decrease in liquid-fill levels. The inception of CHF was similarly delayed with reduction in the liquid fill-levels for 15 and 21 kPa pressures, except for fill-3 case at 21 kPa, for which CHF was not encountered before the limiting temperature in the copper block was reached. Visual observation showed that the liquid pool in the evaporator was

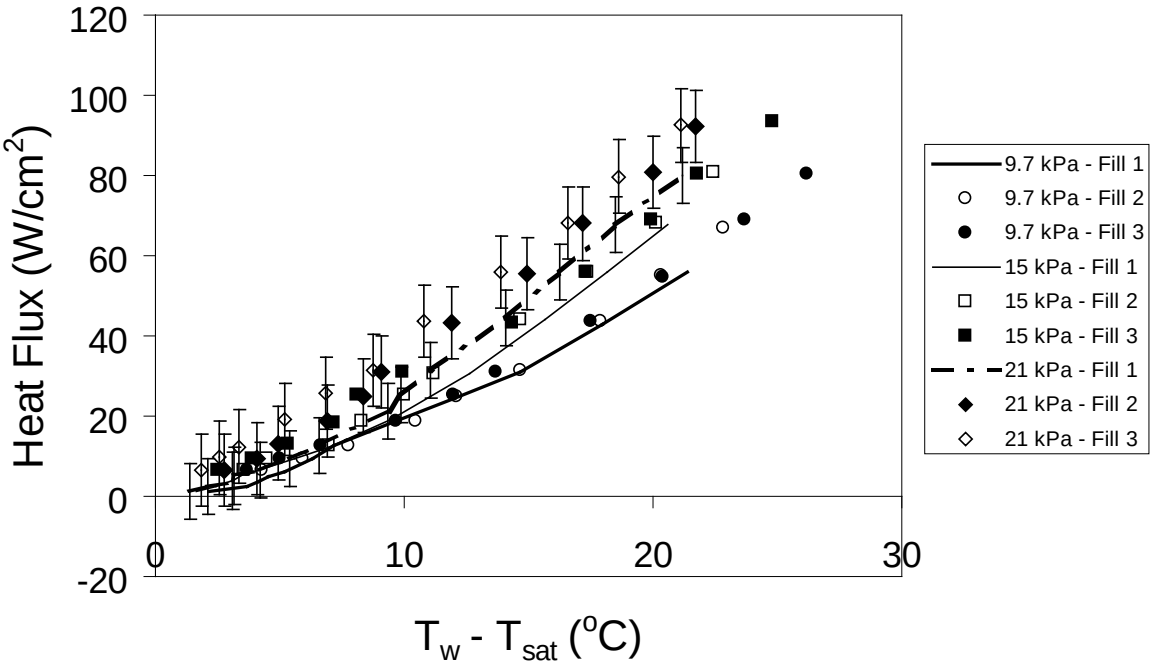

Figure 21: Effect of liquid-fill levels on boiling from a plain surface at different pressures. Results for 21 kPa shown with error bars for range of standard error.

highly agitated at 21 kPa, which forced liquid into the connecting tubing between the evaporator and condenser for fill-1 and fill-2 conditions. Shear stress from the vapor flow carried the liquid into the condenser. Since the design of the condenser allowed only periodic draining of the condensate after sufficient pressure build-up, the additional liquid from the evaporator would reduce the heat transfer coefficient in the condenser. If we assume annular flow in the condenser, the additional liquid from the evaporator would form a thin film in the condenser and would thus impede the condensation heat transfer coefficient. A reduction in condensation heat transfer coefficient would consequently reduce the heat transfer from the evaporator. For fill-3, the height difference between the liquid pool and the connecting tubing was large enough to prevent any upward liquid flow from the pool. As a result, the condensation heat transfer coefficient has higher than fill-1 and fill-2 cases.

It is also observed that the inception of CHF for each pressure is correspondingly delayed with decrease in fill levels, as shown in Table 7. For fill-3 case, most of the

Table 7: Comparison of CHF (W/cm^2) at different pressures and different fill-levels (plain surface)

Pressure (kPa)	CHF (W/cm^2)		
	Fill-1	**Fill-2**	**Fill-3**
9.7	62	81	90
15	68	93	105
21	87	105	CHF not reached

heat transfer in the evaporator was latent. The sub-cooled liquid from the condenser was heated to the saturation temperature and then vaporized, thereby transferring the energy as latent heat to the vapor, which was carried to the condenser. In case of fill-1 and fill-2, after the sub-cooled liquid was heated to saturation temperature, a portion of the liquid was carried to the condenser due to upward vapor movement, while the rest of the mass flux was vaporized. Fill-1 and fill-2 levels thus resulted in lower heat transfer in the evaporator and consequently wall temperature was higher than the fill-3 case. This might lead to increasing the CHF for lower fill conditions. Moreover, with the lower fill levels similar to fill-3, there is less chance of liquid entering the connecting tubing between evaporator and condenser. This will lead to higher heat transfer coefficients in the condenser, as the heat transfer would occur mostly through transfer of latent heat in the condenser.

The thermal resistance values before the onset of CHF are listed in Table 8. The boiling surface thermal resistance is defined as:

$$R_t = \frac{T_w - T_{sat}}{Q'} \tag{4}$$

where, R_t is the thermal resistance, T_w is the wall temperature, T_{sat} is the saturation temperature and Q' is the input power. The boiling thermal resistances showed similar trends for 9.7, 15 and 21 kPa. The thermal resistance curves at 21 kPa for all fill levels are shown as representative curves in Figure 22. The thermal resistance values for all fill levels at the initiation of each experimental run decreased with increasing pressure respectively. The improvement obtained in heat transfer coefficient with reduction

Table 8: Overall thermal resistance (^{o}C/W) at different pressures and liquid fill levels for plain surface

Pressure (kPa)	Overall Thermal Resistance (^{o}C/W)		
	Fill-1	**Fill-2**	**Fill-3**
9.7	0.24	0.21	0.20
15	0.19	0.17	0.16
21	0.16	0.15	0.14

in liquid fill-level is depicted by the lower thermal resistances obtained with decrease in fill levels. For all pressures, the fill-3 level achieved the lowest thermal resistance, before CHF was achieved. In general, the thermal resistance values approached an asymptotic value before the onset of CHF. The thermal resistance values clearly show that lowering the liquid-fill level from fill-1 to fill-3, the heat transfer coefficient increases 200% within 20 W/cm^2. However, beyond 50 W/cm^2, the effect of fill-level on the heat transfer coefficient tends to have negligible influence. From Figure 22, we can also notice the high thermal resistance for heat fluxes < 10 W/cm^2. Beyond 10 W/cm^2, the thermal resistance drops rapidly, which might signify the increase in heat transfer coefficient at the onset of boiling. It is interesting to note that the thermal resistance for fill-3 (for 21 kPa case only) showed a small change of 0.18 ^{o}C to 0.14 ^{o}C, which amounts to 22% decrease in thermal resistance throughout the entire heat flux range, as shown in Figure 22. This might suggest that the decrease in fill level generates more uniformity in surface heat transfer coefficient for a plain surface. In this respect, these results also suggest the existence of an optimum fill-level for a particular operating pressure, which will lead to a uniform heat transfer in the evaporator.

4.3 Study on Enhancement Structure

Experiments were done at pressures of 9.7, 15 and 21 kPa on three different enhanced structures - 1, 4 and 6 layer structures. The results are compared with respect to

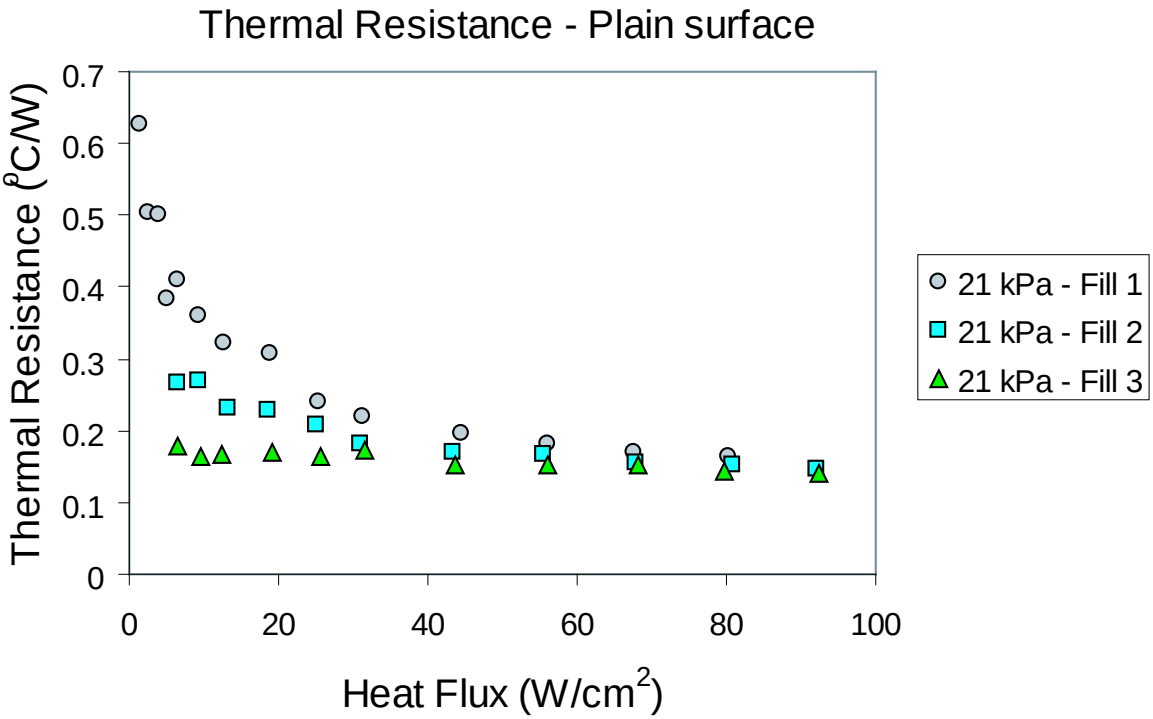

Figure 22: Effect of liquid-fill levels on thermal resistance for boiling with plain surface at 21 kPa

the baseline study. For each enhanced structure, the experiments were done for the full-fill level first. After the completion of all the experimental runs, the system valve was slowly opened to equalize the pressure inside the system with the atmospheric pressure. Then the drain valve was opened to drain the liquid. After draining, high pressure air was blown through the opening of the system valve, to remove the remaining water from the system. Trace amounts of water might have remained in the system in places where tube fittings were placed. After this step, the drain valve was closed and the system was charged to fill-2 level in the same way as described in the earlier section. This same procedure was applied for filling to fill-3 level.

4.3.1 Study on single-layer boiling enhancement structure

The effects of liquid-fill level on the single layer enhanced structure at 9.7 and 21 kPa are shown in Figure 23 and 24 respectively. The trends of the boiling curves for the 15 kPa case were similar to the 9.7 and 21 kPa cases, with wall superheat values

Table 9: Comparison of wall superheats (T_w - T_{sat}) at 80 W/cm^2 at various pressures and fill levels for 1-layer structure

Fill Level	Wall superheat (^{o}C)		
	9.7 kPa	**15 kPa**	**21 kPa**
Fill-1	21.0 [CHF]	18.5 [CHF]	15.0 [21.5]
Fill-2	21.0 [CHF]	18.5 [CHF]	16.0 [20.0]
Fill-3	20.0 [26.0]	17.0 [22.0]	16.5 [18.5]

Plain surface conditions shown within [ ]

falling in between the values achieved for 9.7 and 21 kPa. So the extreme pressure cases of 9.7 and 21 kPa are shown here. The boiling curves at different fill levels are shown with respect to the boiling curves for plain surfaces. A comparison of the wall superheat (T_w - T_{sat}) values at 80 W/cm^2 at different pressures and fill levels is also listed in Table 9.

For the case of 9.7 kPa, the boiling curves of the enhanced structure do not show significant difference with respect to the plain surface below 20 W/cm^2. Beyond 20 W/cm^2, the enhancement in heat transfer of the single layer structure is clearly visible. With increase in heat flux, enhancement structure achieves lower wall superheats than the plain surface. The wall superheat values also showed a dependency on the fill level with increase in the surface heat flux beyond 60 W/cm^2. However, beyond 100 W/cm^2, the performance for the fill-1 level started to degrade. After 60 W/cm^2, fill-3 showed marginally better thermal performance than fill-2, but after 80 W/cm^2 fill-2 showed better performance than fill-3. Beyond 100 W/cm^2, the enhancement of fill-2 with respect to fill-3 can be seen from the difference in wall superheat values, which reached a value of 6 ^{o}C. This behavior can be attributed to liquid movement to the condenser at higher heat fluxes from fill-1 level, which will in turn reduce the condensation heat transfer coefficient.

For the 21 kPa pressure case, the influence of the fill levels is observed beyond 10 W/cm^2. However, contrary to the 9.7 kPa case, degradation in thermal performance

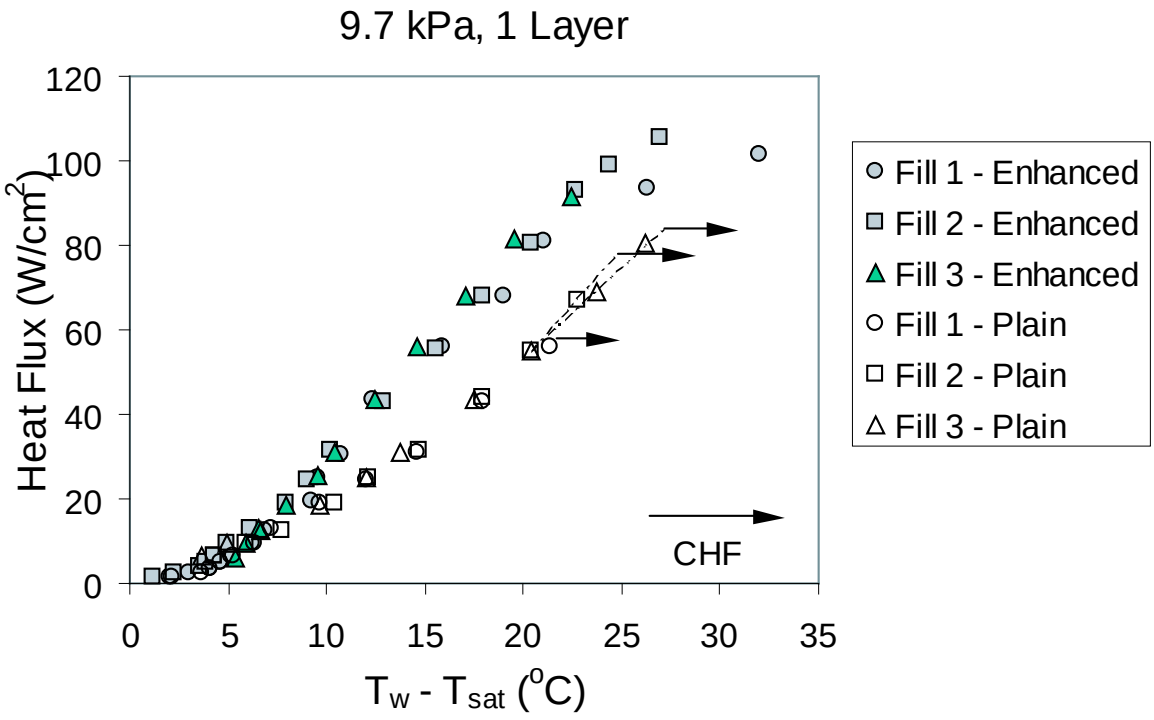

Figure 23: Effect of liquid-fill levels on boiling from a 1-layer structure at 9.7 kPa

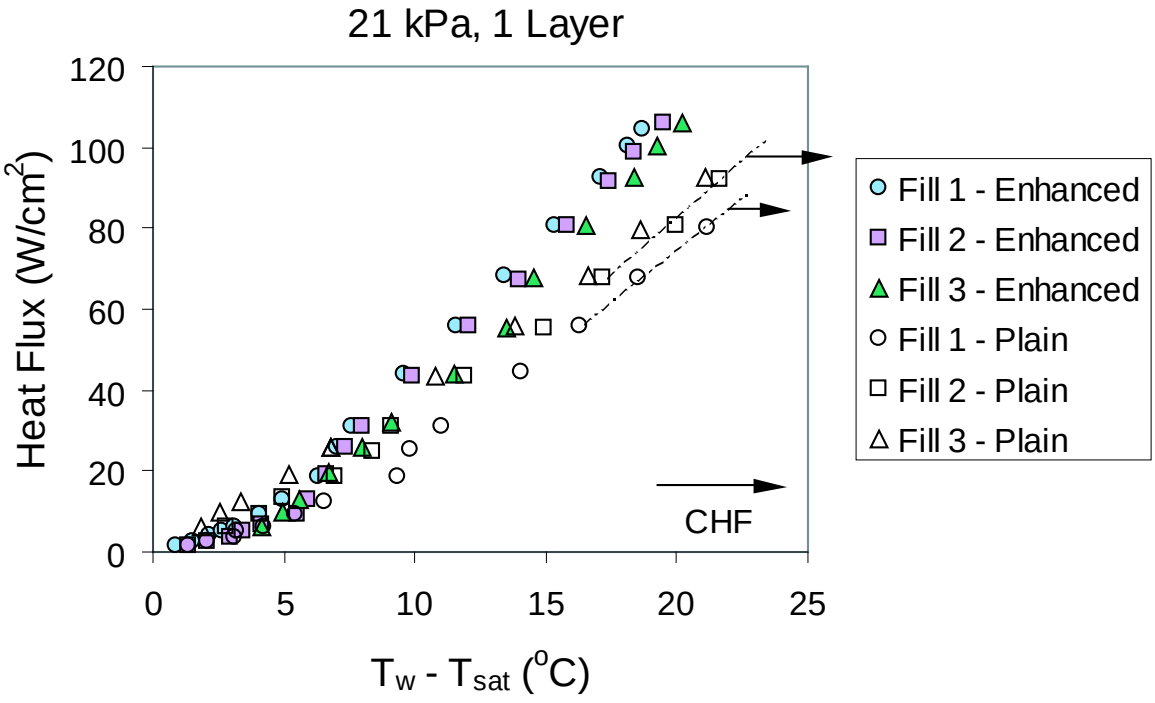

Figure 24: Effect of liquid-fill levels on boiling from a 1-layer structure at 21 kPa

Table 10: Overall thermal resistance (^{o}C/W) at different pressures and liquid fill levels for single-layer structure for the highest heat flux achieved

Pressure (kPa)	Overall thermal resistance (^{o}C/W)		
	Fill-1	**Fill-2**	**Fill-3**
9.7	0.19	0.16	0.15
15	0.14	0.13	0.13
21	0.11	0.11	0.12

is noticed for fill-3 (Figure 24). The difference in wall superheat values between fill-1 and fill-3 was 2-3 ^{o}C at the same heat flux. Recently Pal and Joshi [60] have shown that the single-layer structure (similar to the one used in the present study) achieves the best thermal performance with increase in saturation pressure. Van Stralen et al. [20] has shown that an increase in saturation pressure leads to a decrease in the radius of the bubbles dislodged from the surface. At higher heat fluxes this leads to vigorous boiling activity in the pool. From visual observation, it was observed that vigorous bubble generation generates a lot of agitation on the top surface of the liquid pool, resulting in a reduction in the effective height of the liquid pool. A reduced effective pool height would also lead to a decrease in the net buoyancy force exerted on the bubbles for dislodging from the boiling surface. This would reduce the heat flux from the surface.

The thermal resistance values for the single-layer structure at three difference fill levels are shown in Table 10. The heat transfer enhancement with increase in pressure is clearly noticed from the decreasing thermal resistance values with decreasing fill-levels. In all the cases, the thermal resistance values reach an asymptotic value beyond 80 W/cm^2. As previously mentioned, the degradation of thermal performance at fill-3 for 21 kPa is noticed with an increase in the thermal resistance values to 0.12 ^{o}C/W. The thermal resistance curves for 15 kPa pressure is shown in Figure 25. The heat transfer at lower heat fluxes (< 20 W/cm^2) is clearly visible from the thermal resistance curves.

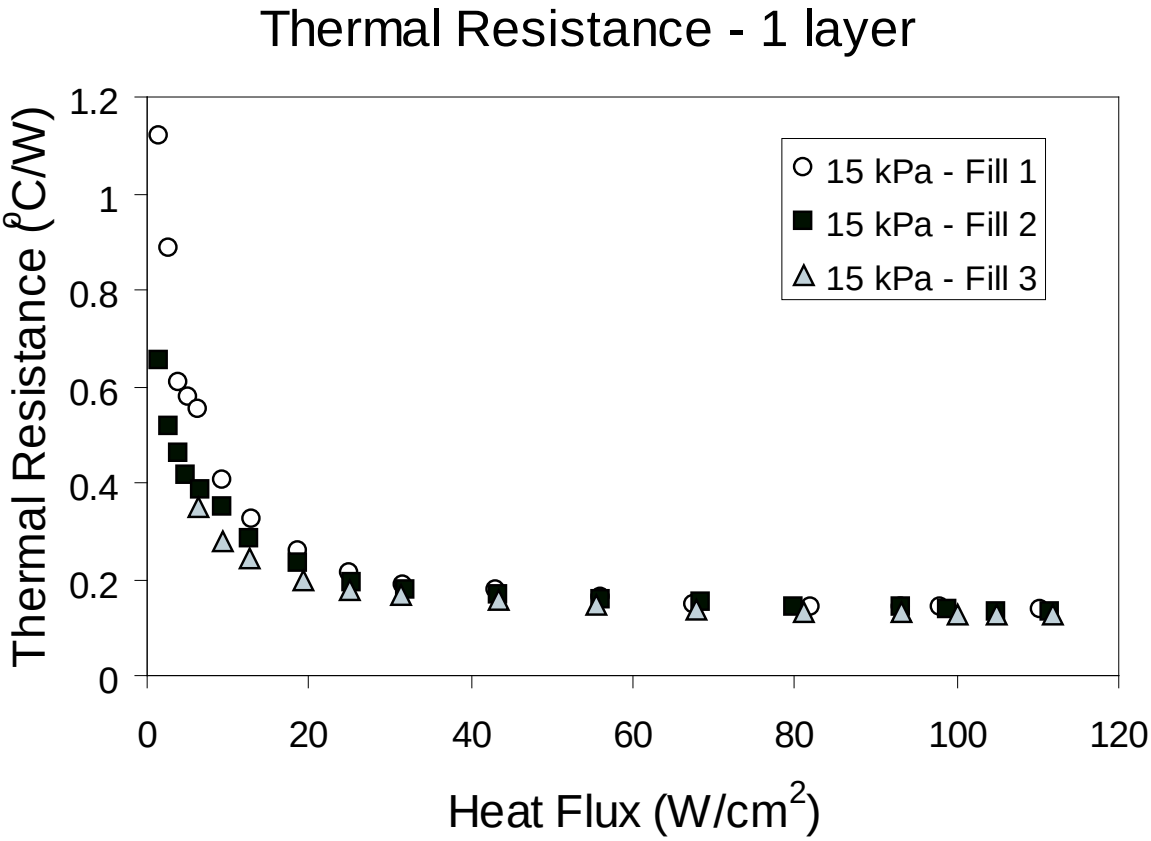

Figure 25: Effect of liquid-fill levels on thermal resistance for boiling with single-layer structure at 15 kPa

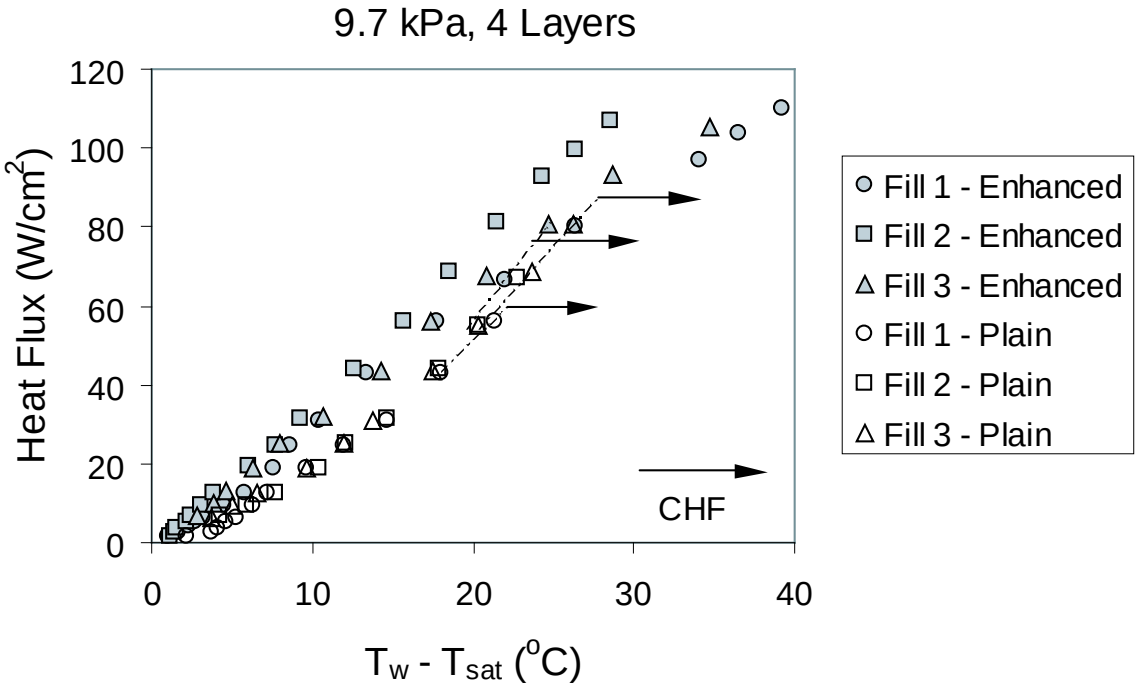

Figure 26: Effect of liquid-fill level on boiling from a 4-layer structure at 9.7 kPa

4.3.2 Study on 4-layer boiling enhancement structure

The boiling curves for 9.7, 15 and 21 kPa cases are shown in Figure 26, 27 and 28 respectively. The effectiveness of the fill levels on the heat transfer can be observed from the listing of the wall superheat values at 80 W/cm^2, as shown in Table 11. Overall fill-2 achieved the best thermal performance followed by fill-3 and fill-1. However, with increase in the saturation pressure, the difference in thermal performances decreased, evident in the decreasing difference in wall superheat values, as shown in Table 11. At 9.7 kPa, the wall superheat for fill-2 is lower by 4-5 ^{o}C with respect to fill-1 and fill-3, however, the difference reduced to 1 ^{o}C at 21 kPa. This shows that the liquid fill levels have a reducing influence on thermal performance with increase in saturation pressure. The heat flux range of 20-30 W/cm^2 can be considered as the transition zone beyond which the influence of the fill levels is seen on the heat transfer. The dependence of wall heat flux on the liquid fill-level can be explained if the effective height of the liquid column above the top surface of the

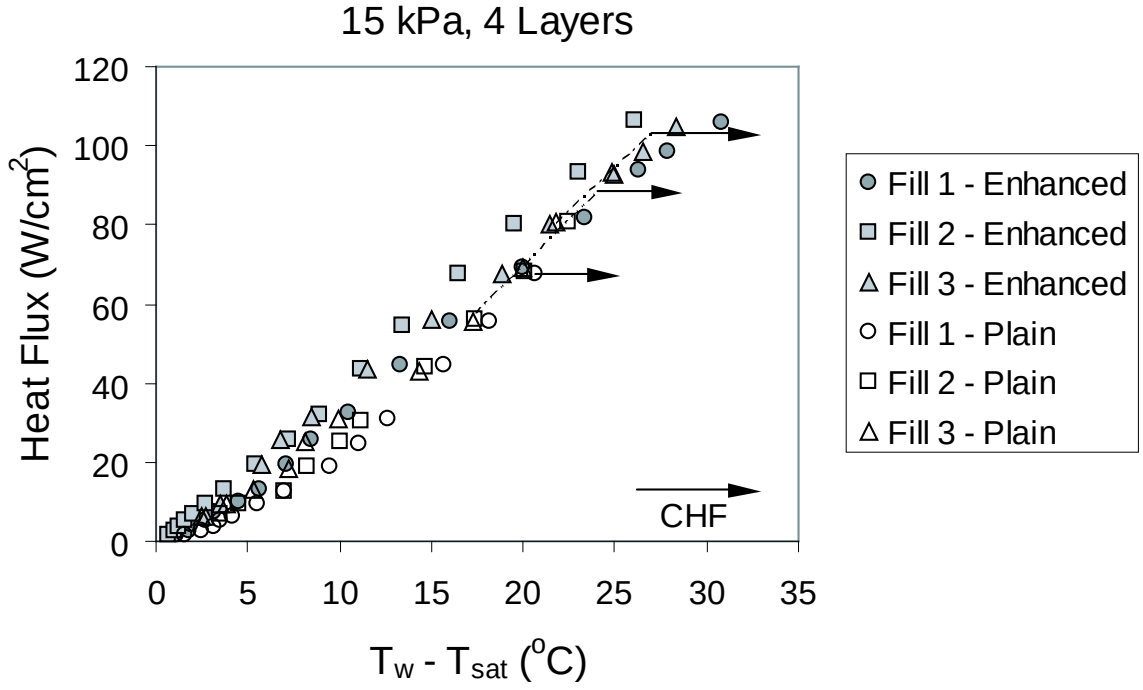

Figure 27: Effect of liquid-fill level on boiling from a 4-layer structure at 15 kPa

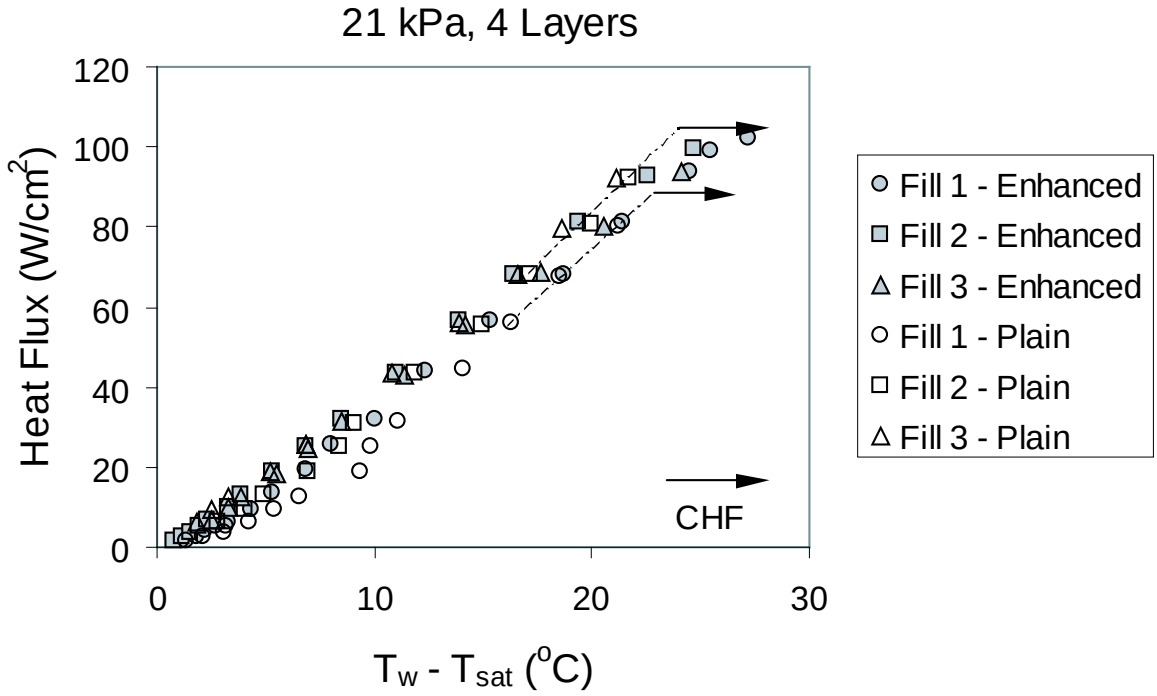

Figure 28: Effect of liquid-fill level on boiling from a 4-layer structure at 21 kPa

Table 11: Comparison of wall superheats at 80 W/cm^2 at various pressures and fill levels for 4-layer structure

Pressure (kPa)	Wall superheat (^{o}C)		
	9.7 kPa	**15 kPa**	**21 kPa**
Fill-1	26.0 [CHF]	23.5 [CHF]	21.5 [21.5]
Fill-2	21.0 [CHF]	19.0 [CHF]	19.0 [20.0]
Fill-3	25.0 [26.0]	21.5 [22.0]	20.0 [18.5]

Plain surface conditions shown within [ ]

enhanced structure is taken into account. The heights of the liquid columns for fill-1, fill-2 and fill-3 were 35 mm, 25 mm and 16 mm respectively. Visual observation showed that at higher heat fluxes, the pool was highly agitated due to vigorous boiling, which reduces the effective height of the liquid column above the boiling surface. As a result, for lower fill cases (like fill-3), the entire boiling surface might not stay fully submerged under the working fluid during vigorous boiling. So, better thermal performance is expected from higher liquid fill levels, which is corroborated by the heat fluxes achieved by fill-2 level. However, increasing the liquid level further might prove detrimental to heat transfer. The agitation of the pool sometimes forces liquid in the connecting tubing between evaporator and condenser, which is taken further downstream by the shear force from the vapor flow. As the condenser used in the experiment didn't allow continuous draining of the condensate, the liquid coming from the evaporator will provide extra thermal resistance to heat transfer from the condenser. This process will reduce the heat flux from the evaporator. The 4-layer structure also achieves higher heat flux with respect to the plain surface, however the heat transfer enhancement decreases as the saturation pressure was increased. The increase in the number of layers in the boiling structure generated more nucleation points with respect to a single-layer structure. However, increasing the layers in a stacked structure also leads to a reduction in heat transfer coefficient, due to the fin effect from the layered structure, as reported by Ramaswamy [62]. With a stacked

Table 12: Overall thermal resistance (^{o}C/W) at different pressures and liquid fill levels for 4-layer structure for the highest heat flux achieved

Pressure (kPa)	Overall thermal resistance (^{o}C/W)		
	Fill-1	**Fill-2**	**Fill-3**
9.7	0.22	0.17	0.20
15	0.18	0.15	0.17
21	0.16	0.15	0.16

structure, the bulk of the boiling takes place at the top-most layer. Due to thermal resistance encountered as a result of fin-effect in the stacked layers, the temperature of the top layer will be less than the base temperature of the structure. If we assume that the boiling from each layer is dependent on the local wall superheat, then a higher stacked structure will have lower heat transfer coefficient.

The thermal resistances at the highest heat flux for boiling with the 4-layer structure at three different liquid fill levels are shown in Table 12. The higher heat transfer coefficient achieved for the fill-2 case is also evident from the lower values of thermal resistance for fill-2, as shown in Table 12. In fill-1 and fill-3 cases at 9.7 kPa, the thermal resistance is found to increase after reaching a global minimum value of 0.19 ^{o}C/W at 50 W/cm^2, as shown in Figure 29. However, fill-2 level on the other hand, reaches for an asymptotic thermal resistance value of 0.17. For 15 and 21 kPa, the thermal resistances are found to tend towards as asymptotic value, as shown in Table 12. These results also might suggest the existence of an optimum liquid level in the evaporator. A liquid height lower than the optimum height will reduce the buoyancy force on the bubbles resulting in reduction of the bubble generation rate. On the other hand, a liquid height higher than the optimum height will result in liquid reaching the condenser, lining the walls of the condenser and thus reducing the condensation heat transfer coefficient.

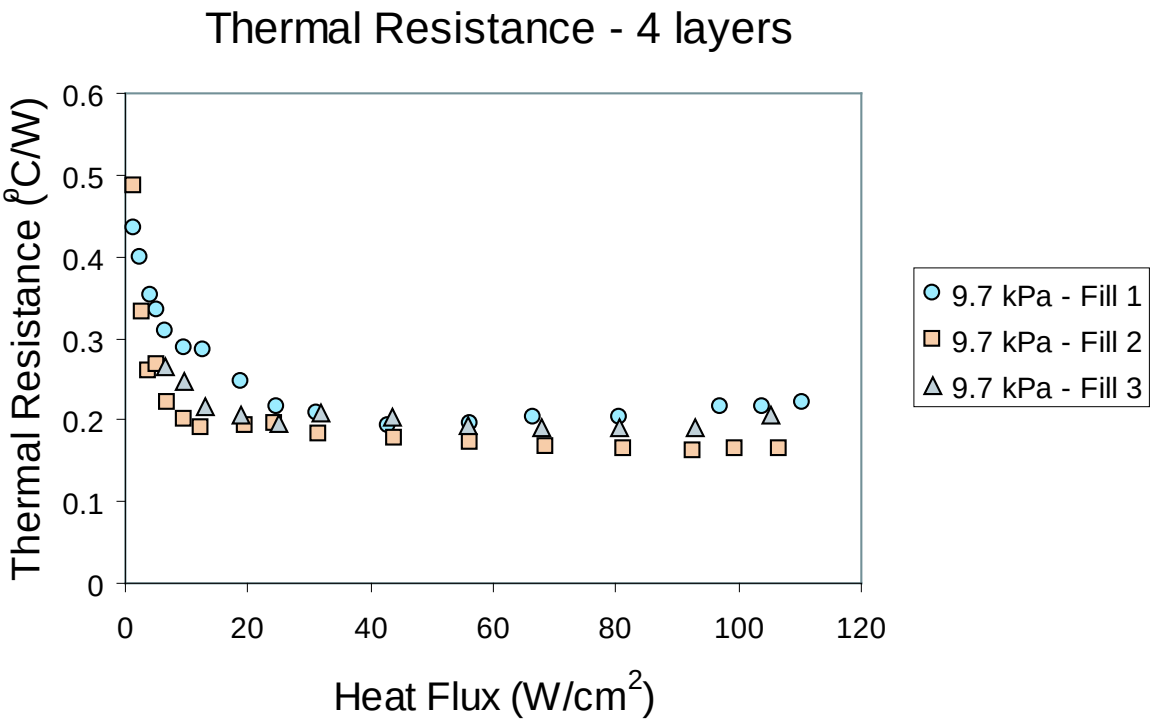

Figure 29: Effect of liquid-fill level on thermal resistance for boiling with 4-layer structure at 9.7 kPa

4.3.3 Study on 6-layer boiling enhancement structure

The boiling curves for the 6-layer structure at saturation pressures of 9.7, 15 and 21 kPa for different fill levels are shown in Figure 30, 31 and 32 respectively. The boiling curves for the plain surface at 9.7, 15 and 21 kPa pressures are also shown for comparison. At lower heat fluxes (< 40 W/cm^2), the boiling curves are closely packed, which shows negligible influence of the fill levels on the heat transfer. Beyond 40 W/cm^2, the influence of the fill levels is clearly seen and fill-1 shows the best performance for all the pressures, followed by fill-2 and fill-3 levels. For the 6-layer structure, the heights of the liquid column above the top surface of the boiling structure were 33, 23 and 14 mm for fill-1, fill-2 and fill-3 levels respectively. With a reduced liquid column height at fill-3 level, the buoyancy force acting on the bubbles will be the least of all the cases under consideration, which will result in a slow bubble dislodging process. Moreover, during vigorous boiling, the effective height of the liquid

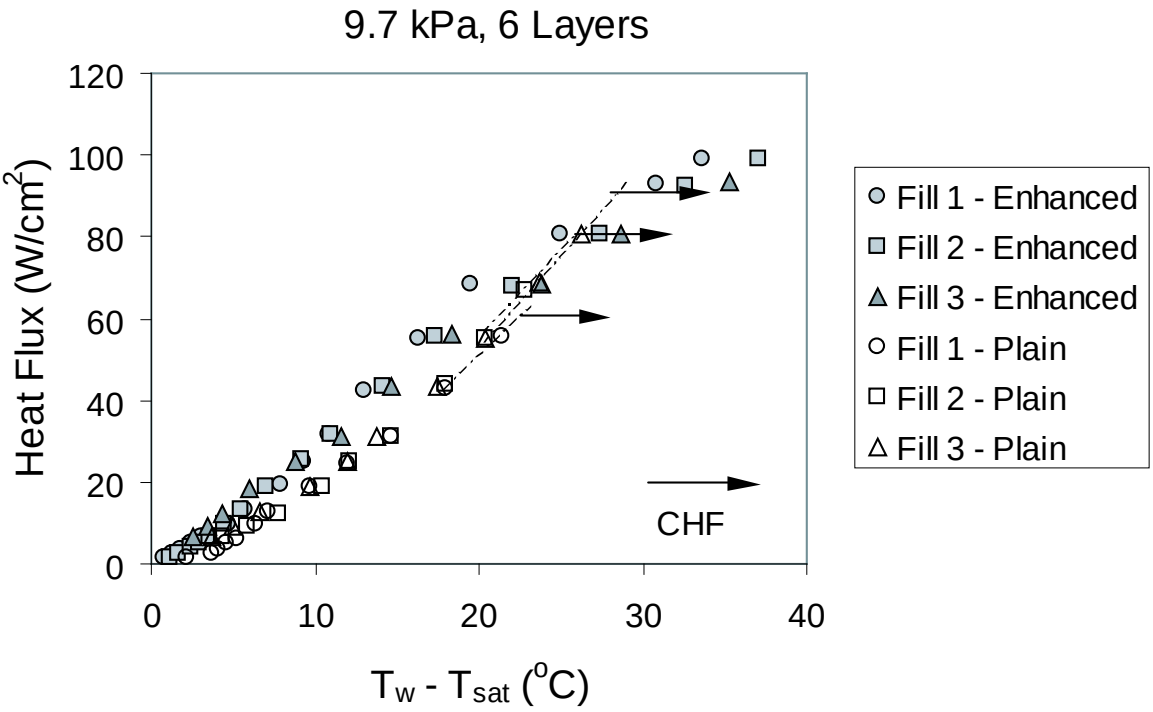

Figure 30: Effect of liquid-fill level on boiling from a 6-layer structure at 9.7 kPa

column decreases (as observed previously for other structures), which would create a situation where the liquid would not be able to keep the structure fully wetted. This situation will lead to a reduction in the heat transfer coefficient at higher heat fluxes. So with an increase in the height of the 6-layer boiling enhancement structure, a higher liquid level (fill-1) was required for improved performance. This suggests an optimum liquid fill level depending on the height of the boiling structure, where the optimum height of the liquid level increases with the height of the boiling structure.

The wall heat transfer for a 6-layer structure compared to the plain surface is worse than that of the 4-layer structure. From the curves, it is observed that the boiling performance from the 6-layer structure resembles that of boiling from a plain surface at approximately 80 W/cm^2 and gets worse with further increase in the heat flux. Though CHF was not observed in the case of 6-layer structure, the wall superheat values were more than 5 ^{o}C than the wall superheat values obtained at CHF condition for the plain surface at 21 kPa. The variation in heat flux with respect to changes

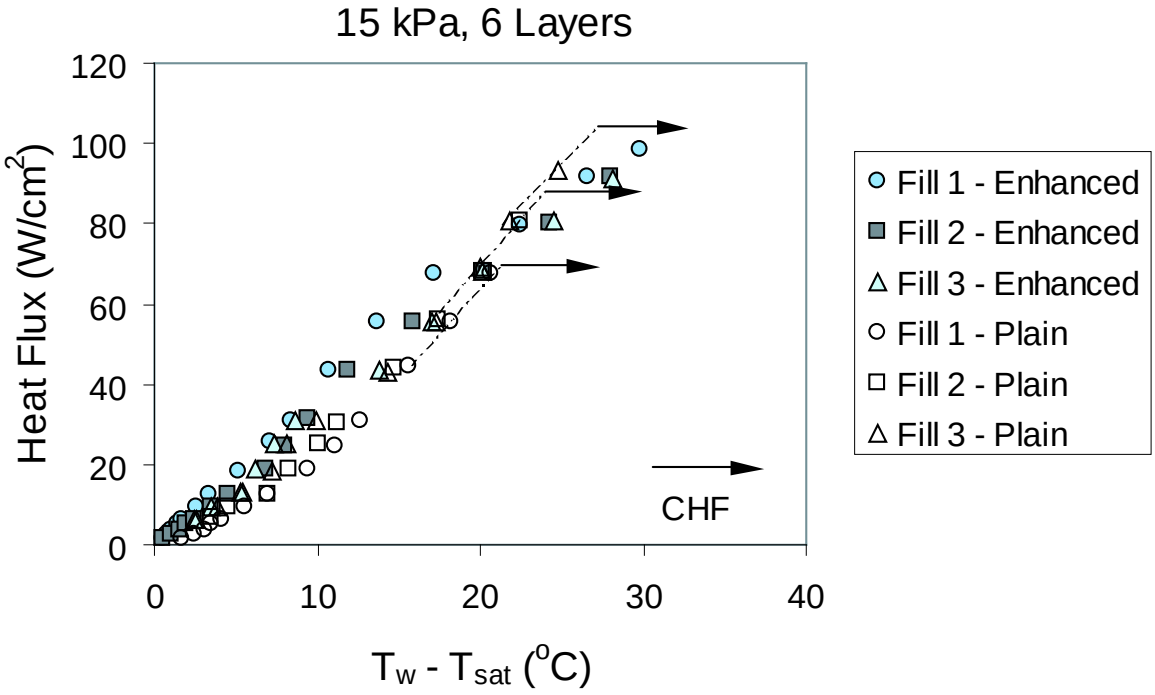

Figure 31: Effect of liquid-fill level on boiling from a 6-layer structure at 15 kPa

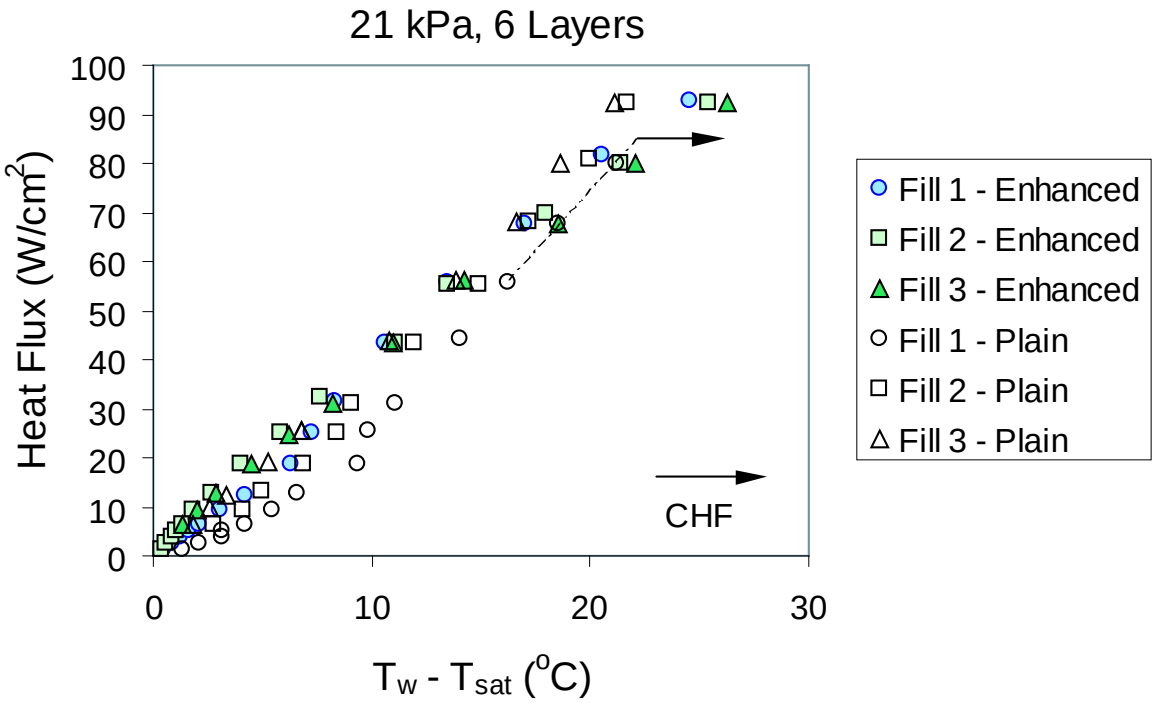

Figure 32: Effect of liquid-fill level on boiling from a 6-layer structure at 21 kPa

in liquid fill-level noticed in the present study is a marked departure from the results reported by Ramaswamy et al. [7]. They performed their experiments with PF5060 at atmospheric pressure and found that heat flux is insensitive to liquid fill level, as long as the boiling surface stays fully covered with the working fluid. The present study employs water as the working fluid, however it is apparent from the present observations that the bubble generation dynamics in a closed loop thermosyphon is responsible for this marked departure in heat transfer.

The thermal resistances for the 6-layer structure are shown in Table 13. The highest liquid level, fill-1 achieved the lowest thermal resistances for all pressures under consideration. However, an interesting observation from the thermal resistance values for the 6-layer structure is the increase of thermal resistance at higher heat fluxes. Previously, we have noted that the thermal resistance values reach an asymptotic value for the 1 and 4 layer structures as the heat flux reached 100 W/cm^2. However, for the 6-layer structure, the thermal resistances are found to increase beyond 60 W/cm^2 for all the fill levels. A typical example is shown for 9.7 kPa in Figure 33. This might be related to the height of the structure and the liquid fill levels. At higher heat fluxes, vigorous boiling generates lots of agitation in the boiling pool, and the emerging bubbles might be impeding the liquid contact of the boiling surfaces. As a result the heat transfer decreases, which is reflected in the monotonous increase of thermal resistance at higher heat fluxes. It can be concluded that increasing the layers of the enhanced structure does not aid in heat dissipation by removing higher heat flux. The effect of the liquid level, coupled with the height of the enhanced structure might create a situation detrimental to high heat flux removal.

Table 13: Overall thermal resistance (^{o}C/W) at different pressures and liquid fill levels for 6-layer structure for the highest heat flux achieved

Pressure (kPa)	Overall thermal resistance (^{o}C/W)		
	Fill-1	**Fill-2**	**Fill-3**
9.7	0.21	0.23	0.23
15	0.19	0.19	0.19
21	0.16	0.17	0.16

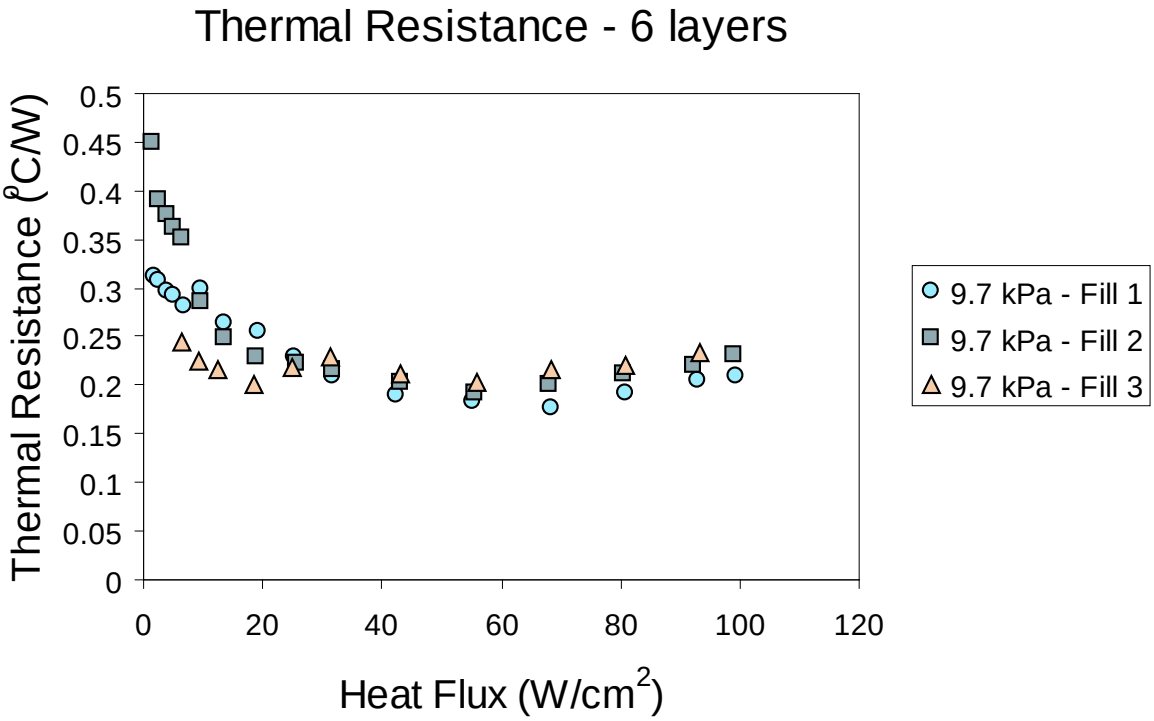

Figure 33: Effect of liquid-fill level on thermal resistance for boiling with 6-layer structure at 9.7 kPa

4.3.4 Comment

The height of the evaporator significantly contributed to the transport of working fluid from the evaporator to the condenser during vigorous boiling conditions at fill-1 and fill-2 levels. A taller evaporator would however, restrict the liquid entrainment in the condenser. In that case, the heat transfer in the condenser would be mostly latent, and thus would produce a higher heat transfer coefficient compared to the case for liquid entrainment with similar liquid levels. In the absence of liquid entrainment, the heat transfer in the evaporator would be dependent on the buoyancy force exerted on the bubble during dislodging from the surface. However, taller evaporators may not be suitable for designing compact thermosyphons required for the current and next generation thermal management systems.

4.4 Summary

In this chapter, the effect of liquid-fill volume on the heat transfer in a thermosyphon is discussed. Experiments were done with 3 different liquid levels at pressures of 9.7, 15 and 21 kPa using 1-layer, 4-layer and 6-layer structures. The results were compared with a baseline study of boiling with a plain surface, using similar liquid levels in the evaporator. The details of the experimental procedure was discussed. The study was presented with the help of boiling curves at all the heat fluxes and saturation conditions under consideration. Thermal resistance curves for all the cases were also presented. The following are the main observations from the study:

- For boiling from a plain surface, a reduction in liquid fill-levels is seen to increase the heat transfer with a corresponding increase in CHF also. It is found that the change in liquid-fill levels has a more pronounced effect for the higher pressure case (21 kPa), whereas for lower pressures (9.7 and 15 kPa), the effects are negligible.

- The heat transfer is observed to be dependent on the liquid level for boiling with enhanced structures. The height difference between the liquid level and the top of the structure influences the hydrostatic pressure head on the boiling surface and thus affect the bubble generation. Higher buoyancy force will thus aid in bubble generation and increased heat transfer.

- Results from the study on three structures suggest that an optimum liquid level might exist for each structure. With increase in the height of the structure, the liquid level producing the best performance is also seen to increase.

- For lower fill levels, vigorous boiling at higher heat fluxes (> 60 W/cm^2) might prevent the liquid from wetting the structure. As a result, the performance would be worse for such cases.

CHAPTER V

CONDENSATION MODEL

A schematic of the physical problem for a horizontal rectangular channel of height H and width W is shown in Figure 34, in which the expected profiles of liquid and vapor phases along the axial direction are shown. Saturated vapor at temperature of T_{sat}, corresponding to pressure, p_{sat}, enters the channel at $z = 0$ and gets condensed along the length of the channel as it comes in contact with the channel wall maintained at a fixed wall temperature, T_w ($< T_{sat}$). As the liquid-vapor mixture progresses along the length of the channel, thickness of the liquid film along the walls increases while the area of the vapor core decreases. The vapor pressure changes along the axial direction, which also influences the saturation temperature, T_{sat}. Considering symmetry with respect to the vertical plane passing through the axis of the channel, the liquid film is divided into five different regions - (1) top film zone, (2) top corner zone, (3) vertical film zone, (4) bottom corner zone and (5) bottom film zone, as shown in Figure 35. The configuration of the corner liquid zones and the thin film zones is similar to the configuration adopted by Zhao and Liao [52] in their model of condensation in vertical triangular channel. However, the current model analyzes condensation in a horizontal rectangular channel, which introduces additional thin liquid zones and corner zones compared to the analysis of only one thin film zone and one corner zone required for vertical triangular channel. The interaction of multiple corner zones and thin film zones with each other also add to the complexity in the analysis of condensation in horizontal rectangular channel. Wang and co-workers [53, 54, 55] considered 5 zones in describing the condensate along the walls of a rectangular channel, however, the numerical treatment adopted by them for the corner liquid zones was different

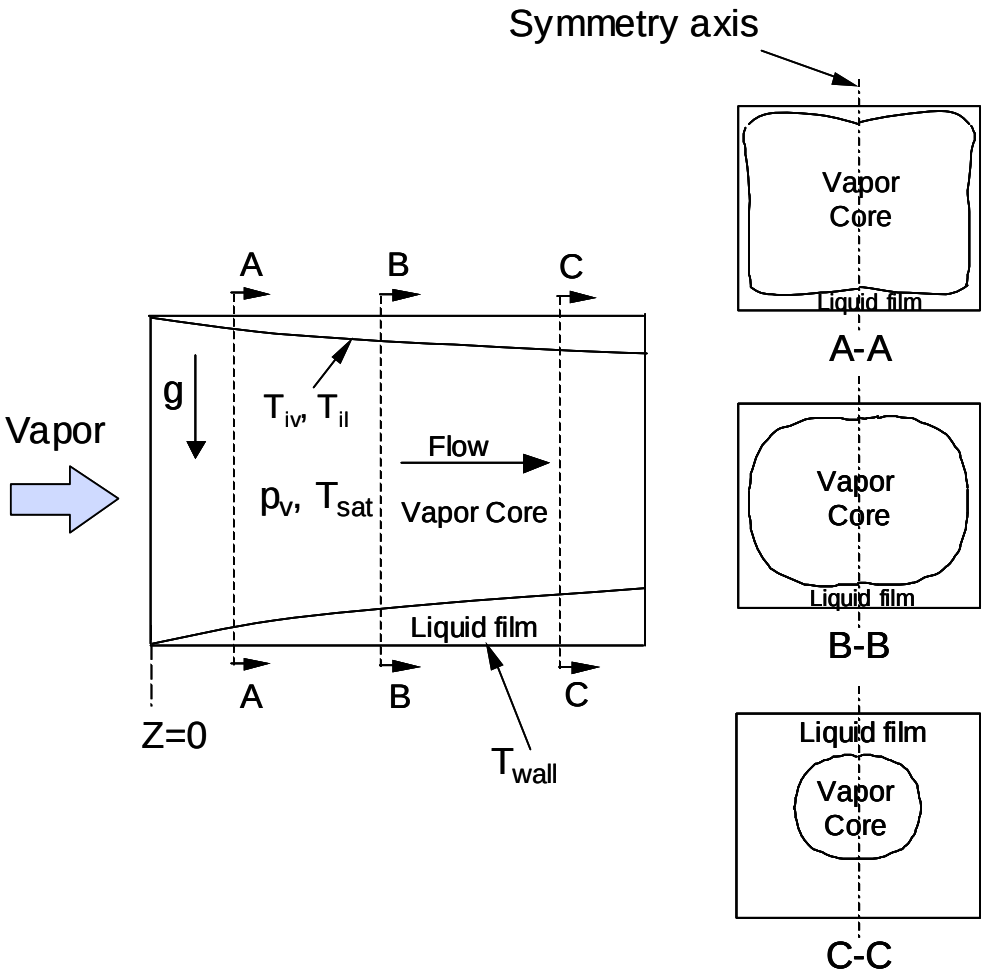

Figure 34: Schematic of the physical problem of condensation in rectangular microchannel

from the current analysis, as discussed in Section 5.3. Moreover, the mass balance of the vapor core was not analyzed in their model, compared to the current model, as discussed in Section 5.4. In the current model, it is assumed that the vapor gets condensed and forms thin films along the top, side and bottom walls. Interfacial tension in the free surface generates a pressure gradient in the liquid film, which drives liquid flow in the film zones (1, 3 and 5) towards the corners through the phenomenon, commonly known as *Gregorig effect* [4]. The current model takes into account the surface tension in the modeling of condensation along the wall, coupled with Nusselt [65] approximations. Gravity is included in the model, which allows the draining of the condensate from the vertical zone into the bottom corner zone. Because of capillary action, both the top and bottom corner zones have condensate flow interaction with the horizontal and the vertical thin film zones. Moreover, the film and the corner zones receive condensate from the vapor core. It is assumed that a portion of the condensate accumulated in the corner zones is responsible for increasing the volume of the zone along the axial direction, while the rest is carried along the axial direction because of interfacial shear stress.

The following assumptions have been incorporated in the model for simulating film condensation:

1. Steady state profile is considered
2. Heat transfer across liquid film is by conduction only
3. Gravity forces are neglected in the top and bottom thin liquid film zones
4. Axial 1-d incompressible fully developed flow exists in vapor core
5. Axial 1-d flow exists in the liquid zone at corners
6. Inertia forces are neglected in the vapor and liquid zones
7. 2-d laminar flow exists in the liquid film

8. No pressure gradient exists normal to walls

9. Thermophysical properties of liquid and vapor are constant

10. No liquid entrainment exists in the vapor core.

5.1 Geometric Parameters

The geometry of the channel and locations of the zones are shown in Figure 35. X and Y are fixed orthogonal coordinates with the origin at the top corner of the channel. The thin liquid film zones (1, 3 and 5) are shown in their respective frames (x-y, x'-y' and x"-y"), which are right-handed with the axial direction (z) along the direction of flow. This treatment allowed the representation of the governing equations in a single reference frame (x-y). The corner zones are represented by the radii of curvature of the zones ($r_{c,i}$, i = 2 and 4 representing zones 2 and 4 respectively). It is assumed that the liquid-vapor interface at the junction of the thin-liquid and corner zones is tangential to the radii of curvature of the corner-liquid zones. The liquid-vapor interface profile is defined by the film thickness parameter, δ(y,z). The thicknesses of the liquid films at the ends of zone 1, 3 and 5 are numbered in an anti-clockwise sense, with 0 and 1 representing the two ends of the zones as shown in Figure 35. Corresponding to the channel configuration, we can define the following geometrical parameters:

$$A_{ch} = \frac{1}{2} \cdot W \cdot H$$

$$A_{lf,j} = \int_0^{L_j} \delta(y,z)dy$$

where A_{ch} is the area of the channel, $A_{lf,j}$ is the area of the j^{th} liquid film zone, j = 1, 3, 5.

$$A_{lc,2} = (r_{c,2} + \delta_{1,1}) \cdot (r_{c,2} + \delta_{3,0}) - \frac{\pi}{4} r_{c,2}^2$$

$$A_{lc,4} = (r_{c,4} + \delta_{3,1}) \cdot (r_{c,4} + \delta_{5,0}) - \frac{\pi}{4} r_{c,4}^2$$

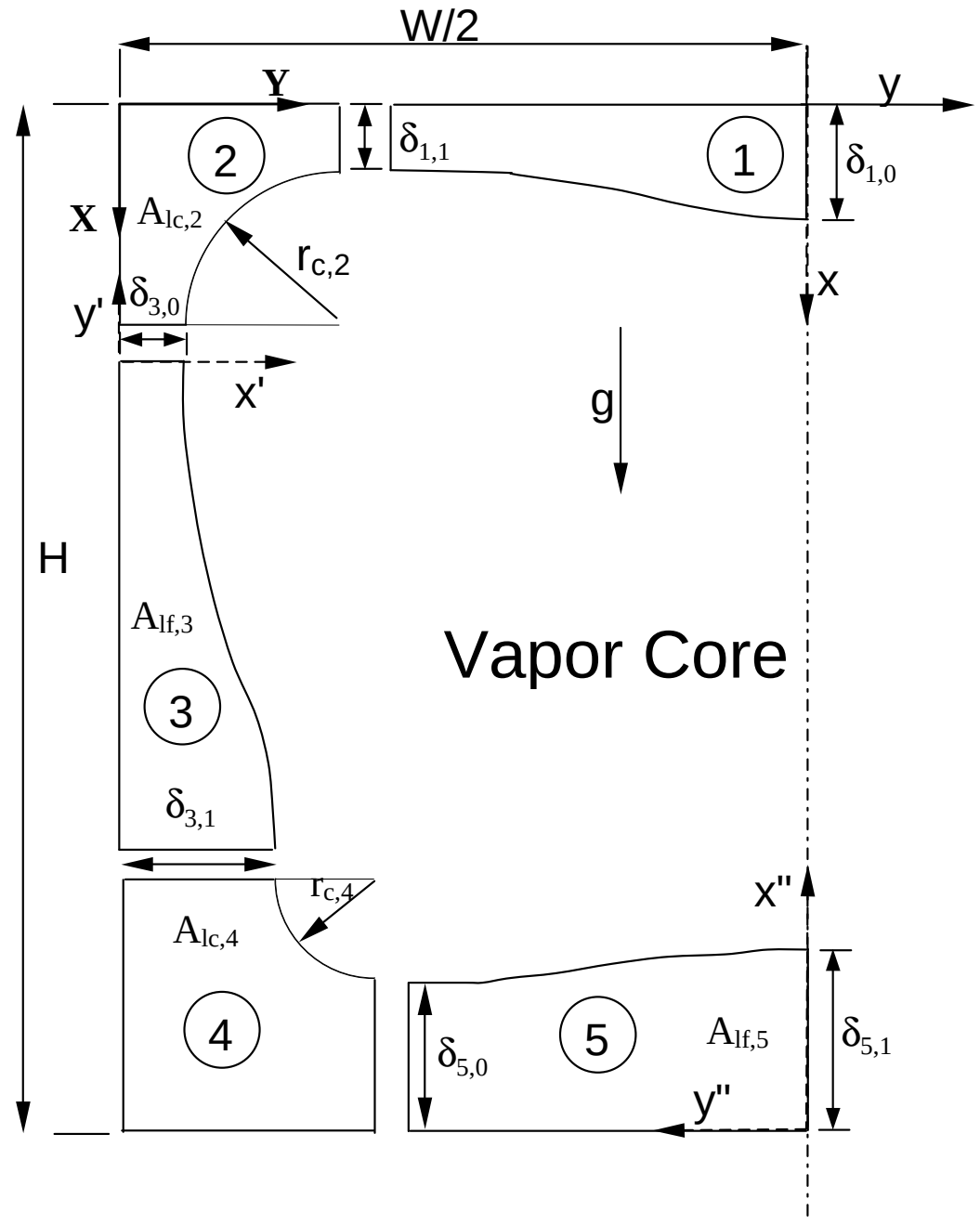

Figure 35: Cross-section of a channel showing the various liquid-vapor zones

where $A_{lc,j}$ is the area of the j^{th} corner liquid zone, j = 2, 4. Then the area of the vapor core zone, A_v, is given by,

$$A_v = A_{ch} - A_{lf,1} - A_{lc,2} - A_{lf,3} - A_{lc,4} - A_{lf,5}$$

The hydraulic diameters of the entire channel, D_h, the corner zones, $D_{lc,k}$ (k = 2, 4) and the vapor core, $D_{h,v}$ are given by,

$$D_h = \frac{4A_{ch}}{P_{ch}}$$

$$D_{lc,k} = \frac{4A_{lc,k}}{P_{lc,k}}$$

$$D_{hv} = \frac{4A_v}{P_v}$$

where P_{ch} is the perimeter of the channel, $P_{lc,k}$ (k = 2, 4) and P_v are the wetted perimeters of the k^{th} corner zone and the vapor core respectively, and defined by the following relations,

$$\begin{aligned} P_{ch} &= 2 \cdot \frac{W}{2} + H = W + H \\ P_{lc,2} &= 2 \cdot r_{c,2} + \delta_{1,1} + \delta_{3,0} \\ P_{lc,4} &= 2 \cdot r_{c,4} + \delta_{3,1} + \delta_{5,0} \\ P_v &= 2 \cdot \frac{W}{2} + H = W + H \end{aligned}$$

5.2 Thin liquid film along the wall

In the thin film zone, incompressible, two-dimensional flow is assumed (along the y and z directions). Following Zhao and Liao [52], the conservation equations for the liquid film can be written as:

Continuity:

$$\frac{\partial u_l}{\partial x} + \frac{\partial v_l}{\partial y} + \frac{\partial w_l}{\partial z} = 0 \qquad (0)$$

where u, v and w are the velocities in the x, y and z directions respectively.

y-momentum:

$$\mu_l \frac{\partial^2 v_l}{\partial x^2} - \frac{\partial p_{lf}}{\partial y} + B\rho_l g = 0 \tag{1}$$

where, $B = 1$ for vertical thin-film zone and 0 for horizontal thin film zones, μ_l is the dynamic viscosity of the liquid, ρ_l is the density of the liquid and g is the acceleration due to gravity.

z-momentum:

$$\mu_l \frac{\partial^2 w_l}{\partial x^2} - \frac{\partial p_{lf}}{\partial z} = 0 \tag{2}$$

Energy conservation:

$$\frac{\partial^2 T_{lf}}{\partial x^2} = 0 \tag{3}$$

where T_{lf} is the temperature in the liquid film.

The pressure in the liquid film, p_{lf} is related to the surface tension, σ_l, and radius of curvature of the liquid-vapor interface (r_c) in the $x-y$ plane by the Young-Laplace equation as follows:

$$\frac{\partial p_{lf}}{\partial y} = \frac{\partial}{\partial y}\left(p_v - \frac{\sigma_l}{r_c}\right) \tag{4}$$

where,

$$r_c = \frac{1}{\kappa} = \frac{\left[1 + \left(\frac{\partial \delta}{\partial y}\right)^2\right]^{3/2}}{\frac{\partial^2 \delta}{\partial y^2}}$$

where κ is the curvature at the liquid-vapor interface.

From our assumption, $\partial p_v/\partial y = 0$, and putting Eq. 4 in Eq. 1 to eliminate the liquid film pressure, p_{lf}, we get:

The modified y-momentum equation:

$$\mu_l \frac{\partial^2 v_l}{\partial x^2} = -\sigma_l \frac{\partial \kappa}{\partial y} - B\rho_l g \tag{5}$$

The velocity along y axis is governed by the following boundary conditions:

$$\begin{aligned} x = 0, \qquad & v_l = 0 \qquad && \Rightarrow C_2 = 0 \\ x = \delta, \qquad & \tfrac{\partial v_l}{\partial x} = 0 \qquad && \Rightarrow C_1 = \left(\sigma_l \tfrac{\partial \kappa}{\partial y} + B\rho_l g\right)\delta \end{aligned} \tag{6}$$

So integrating Eq. 5, we get,

$$v_l = \frac{1}{\mu_l}\left[\sigma_l \frac{\partial \kappa}{\partial y} + B\rho_l g\right]\left(x\delta - \frac{x^2}{2}\right) \tag{7}$$

Similarly, integrating Eq. 2 subjecting to the following boundary condition:

$$\begin{aligned} x = 0, \qquad & w_l = 0 \\ x = \delta, \qquad & \mu_l \tfrac{\partial w_l}{\partial x} = \tau_i \end{aligned} \tag{8}$$

we get,

$$w_l = \frac{1}{\mu_l}\left[\left(\frac{\partial p_v}{\partial z}\right)\frac{x^2}{2} + \left(\tau_i - \delta\frac{\partial p_{lf}}{\partial z}\right)x\right] \tag{9}$$

where τ_i is the interfacial shear stress.

Considering infinitesimal increment of Δz along the axial direction, the radius of curvature of the liquid film can be neglected along the z direction. Then liquid pressure gradient along the z direction, $\partial p_{lf}/\partial z$ can be expressed by the vapor pressure gradient as follows,

$$\frac{\partial p_{lf}}{\partial z} = \frac{\partial p_v}{\partial z} \tag{10}$$

Eliminating $\partial p_{lf}/\partial z$ from Eq. 9, we get,

$$w_l = \frac{1}{\mu_l}\left[\left(\frac{\partial p_{lf}}{\partial z}\right)\frac{x^2}{2} + \left(\tau_i - \delta\frac{\partial p_v}{\partial z}\right)x\right] \tag{11}$$

The boundary conditions for the energy conservation equation are given by:

$$\begin{aligned} x = 0, \qquad & T_{lf} = T_w \\ x = \delta, \qquad & T_{lf} = T_{li} \end{aligned} \tag{12}$$

where, T_{li} is the local temperature at the liquid-vapor interface.

Apart from that, the mass transfer across the liquid-vapor interface, $\dot{m}_i$, can be expressed as:

$$\dot{m}_i h_{fg} = k_l \frac{\partial T_{lf}}{\partial y} \tag{13}$$

where, k_l is the thermal conductivity of the liquid and h_{fg} is the latent heat of vaporization of the liquid.

Using the above boundary conditions and the assumption that the temperature varies linearly in the liquid layer, we can integrate Eq. 3, to get the following expression of the mass flux at the liquid-vapor interface:

$$\begin{aligned} \dot{m}_i h_{fg} &= k_l \frac{T_{li} - T_w}{\delta} \\ \Rightarrow \dot{m}_i &= \frac{k_l}{h_{fg}} \frac{T_{li} - T_w}{\delta} \end{aligned} \tag{13}$$

where T_{li} is the temperature of the liquid at the liquid-vapor interface.

The liquid-vapor interface temperature differs from the saturated bulk vapor temperature because of the interfacial resistance and effects of curvature on saturation pressure over liquid [66].

From the analysis of Stephan and Busse [67] (also employed by Zhao and Liao [52]), we get the expression of T_{li} as,

$$T_{li} = T_{vi} - \dot{m}_i h_{fg} \left[\frac{T_{sat} \sqrt{2\pi R_g T_{sat}}}{h_{fg}^2 \rho_v} \left(\frac{2 - \nu}{\nu} \right) \right] \tag{14}$$

where, R_g is the universal gas constant, ν is the accommodation coefficient and T_{vi} is the local interfacial vapor temperature, and is defined as,

$$T_{vi} = T_{sat} \left(1 + \frac{p_c}{h_{fg} \rho_l} \right) \tag{15}$$

where, p_c is the capillary pressure, and is defined as,

$$p_c = \sigma_l \kappa + \frac{\beta}{\delta^3} \tag{16}$$

where, κ is the curvature of the liquid-vapor interface and β is the dispersion constant with respect to the disjoining force [67].

The local condensate mass flux, $\dot{m}_i$, can also be obtained by integrating the continuity equation (Eq. 0) for the whole thickness of the liquid film:

$$\dot{m}_i = \rho_l \left[\frac{\partial}{\partial y} \left(\int_0^\delta v_l \cdot dx \right) + \frac{\partial}{\partial z} \left(\int_0^\delta w_l \cdot dx \right) \right] \tag{17}$$

Putting the expressions of v_l (Eq. 7) and w_l (Eq. 11) in Eq. 17, we get,

$$\dot{m}_i = \frac{\rho_l}{\mu_l} \left[\frac{\partial}{\partial y} \left\{ \frac{\delta^3}{3} \left(\sigma_l \frac{\partial \kappa}{\partial y} + B \rho_l g \right) \right\} + \frac{\partial}{\partial z} \left\{ \tau_i \frac{\delta^2}{2} - \frac{\delta^3}{3} \frac{\partial p_{lf}}{\partial z} \right\} \right] \tag{18}$$

The mass flow rate is also obtained by replacing the expressions of T_{li} (Eq. 14) in Eq. 13,

$$\dot{m}_i = \frac{\frac{k_l}{\delta \cdot h_{fg}} \left[T_{sat} \left(1 + \frac{p_c}{h_{fg} \cdot \rho_l} \right) - T_w \right]}{1 + \frac{k_l T_{sat} \sqrt{2\pi R_g T_{sat}}}{\delta \cdot h_{fg}^2 \cdot \rho_v} \left(\frac{2-\nu}{\nu} \right)} \tag{19}$$

Combining Eq. 18 and 19 and eliminating $\dot{m}_i$ between them, we get an expression for the local condensate thickness, $\delta(y, z)$, in the form of a partial differential equation as follows,

$$\frac{\partial}{\partial y} \left[\frac{\delta^3}{3} \left(\sigma_l \frac{\partial \kappa}{\partial y} + B \rho_l g \right) \right] + \frac{\partial}{\partial z} \left[\tau_i \frac{\delta^2}{2} - \frac{\delta^3}{3} \frac{\partial p_{lf}}{\partial z} \right] = \frac{\mu_l \left[T_{sat} \left(1 + \frac{p_c}{h_{fg} \cdot \rho_l} \right) - T_w \right]}{\rho_l h_{fg} \left[\frac{\delta}{k_l} + \frac{T_{sat} \sqrt{2\pi R_g T_{sat}}}{h_{fg}^2 \rho_v} \cdot \frac{2-\nu}{\nu} \right]} \tag{20}$$

The above equation is an implicit one, so the unknown parameters are to be simultaneously determined and consequently updated to get the liquid-vapor interface profile. The unknown parameters $\partial p_v / \partial z$, τ_i and T_{sat} will be determined by simultaneously solving Eq. 20 with the equations describing the mass and momentum balances in the vapor core and corner zones.

Eq. 20 is fourth-order in y, and the required boundary conditions (shown in Figure 36), are:

$$\begin{aligned} y = 0 : \quad & \frac{\partial \delta}{\partial y} = 0, \quad & \frac{\partial^3 \delta}{\partial y^3} = 0 \\ y = y_{end} : \quad & \frac{\partial \delta}{\partial y} = 0, \quad & \frac{\partial^2 \delta}{\partial y^2} = \frac{1}{r_c} \end{aligned} \tag{21}$$

where r_c is the radius of curvature of the corner zone adjacent to the thin liquid film zone. Similar boundary conditions were also applied for zone 1 and zone 3.

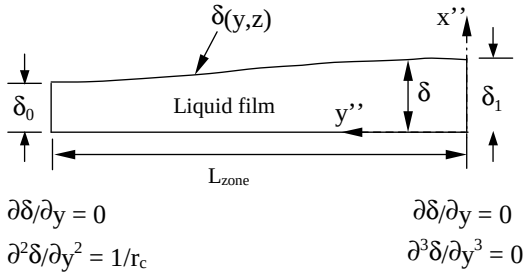

Figure 36: Geometry of the horizontal liquid film zone (Zone 5) and associated boundary conditions

At $z = 0$, the thickness of the condensate would be unaffected due to changes along the z direction, so $\delta(y, 0)$ is obtained from the following expression:

$$\frac{\partial}{\partial y}\left[\frac{\delta^3}{3}\left(\sigma_l \frac{\partial \kappa}{\partial y} + B\rho_l g\right)\right] = \frac{\mu_l\left[T_{sat}\left(1 + \frac{p_c}{h_{fg}\cdot\rho_l}\right) - T_w\right]}{\rho_l \cdot h_{fg}\left[\frac{\delta}{k_l} + \frac{T_s\sqrt{2\pi R_g T_{sat}}}{h_{fg}^2\cdot\rho_v}\cdot\frac{2-\nu}{\nu}\right]} \tag{22}$$

The above equation can be solved using similar boundary conditions as stated in Eq. 21. At $z = 0$, the corner radius (r_c) has to be provided as a boundary condition. Zhao and Liao [52] calculated the initial radius of curvature by assuming the existence of a liquid fraction permanently residing in the corners, termed as "irreducible residual saturation". Wang and Rose [55] also obtained a fourth-order non-linear equation describing the liquid-vapor interface profile, however, their handling of the radii of curvature at channel inlet was not discussed. In the current model, the formation of the condensate profile is modeled from the channel inlet, so initial values were assigned to the corner radii (10% of the width). However, the results were not dependent on the initial value, after the first few steps along z (10-15).

5.3 Condensate Flow in the Corners

The condensate flow in the corner regions is assumed to be one-dimensional, driven along the axial direction by the shear stress exerted by the flow of the vapor core. The mass transfer in the corner zones will occur with the thin liquid zones (capillary action

combined with gravity for the vertical zone) and from condensation occurring at the liquid-vapor interface. Accumulation of condensate will increase the cross-sectional area of the corner zone (A_{lc}) along the axial direction and eventually the thin liquid film zones will cease to exist. Following a similar analysis by Zhao and Liao [52], the hydrodynamics of the corner zones can be obtained through conservation of mass and momentum:

Momentum conservation equation for the corner zone can be expressed as,

$$-\frac{d}{dz}\left(p_{lc}A_{lc}\right) - \tau_{lw}P_{lc} + \tau_i P_i = \rho_l \frac{d}{dz}\left(\bar{w}_{lc}^2 A_{lc}\right) \tag{23}$$

where, p_{lc} is the pressure in the corner zone, τ_{lw} and P_{lw} are the shear stress and wetted-perimeter at the liquid-wall interface respectively, $\bar{w}_{lc}$ is the mean velocity of the corner zone, τ_i and P_i are the shear stress and perimeter at the liquid-vapor interface respectively. Neglecting the change in radius of curvature of the corner liquid zone in the axial (z) direction, we can express $p_{lc} = p_v$. Replacing p_{lc} in Eq. 23 and considering negligible change in the area of the corner zone, A_{lc}, we get the momentum equation of the corner zone as,

$$-\frac{dp_v}{dz} + \frac{d}{dz}\left(\frac{\sigma_l}{r_c}\right) - \frac{\tau_{lw}p_{lc}}{A_{lc}} + \frac{\tau_i P_i}{A_{lc}} = \rho_l \frac{d}{dz}\left(\bar{w}_{lc}^2 A_{lc}\right) \tag{24}$$

The shear stress at the liquid-wall interface can be expressed as:

$$\tau_{lw} = \frac{1}{2}\rho_l \cdot \bar{w}_{lc}^2 \cdot f_l \tag{25}$$

where, the friction factor, f_l can be expressed as follows:

$$f_l = \frac{13.3 \cdot \mu_l}{\rho_l \cdot \bar{w}_{lc} \cdot D_{lc}}$$

The mean velocity in the corner zone, $\bar{w}_{lc}$, can be obtained from a mass balance in the corner zones. This can be achieved through equating the amount of change of mass in the corner zones to the mass accumulated due to condensation ($\dot{m}''_{con}$) and

the amount of mass transfer with the neighboring liquid film zones ($\dot{m}''_{lf}$). This mass transfer interaction can be expressed as follows:

$$\rho_l \frac{d}{dz}\left(\bar{w}_{lc} A_{lc}\right) = \dot{m}''_{lf} + \dot{m}''_{con} \tag{26}$$

where,

$$\dot{m}''_{lf} = \dot{m}''_{ver} + \dot{m}''_{hor} \tag{27}$$

$$\dot{m}''_{con} = \frac{\left(r_c + \delta_1\right)\left(r_c + \delta_2\right) h_{lc}(z) \Delta T(z)}{h_{fg}} \tag{28}$$

where, r_c is the radius of curvature of the corner zone, h_{lc} is the mean condensation heat transfer coefficient of the corner zone (discussed in a later section), $\Delta T(z)$ is the temperature difference between the saturation temperature and wall temperature $(T_{sat} - T_w)$ at each axial location z, δ_1 and δ_2 are the thicknesses at the two ends of the corner zones interfacing with the vertical and horizontal thin liquid film zones respectively and $\dot{m}''_{ver}$, $\dot{m}''_{hor}$ are the mass fluxes entering the corner zones from the vertical and horizontal thin-film liquid zones respectively, and are expressed as:

$$\begin{aligned} \dot{m}''_{ver} &= \left[\int_0^{\delta_1} \rho_l \cdot v_l \cdot dx\right]_{y=y_{end}} \\ &= \frac{\rho_l \cdot \delta_1^3}{3\mu_l}\left[\sigma_l \frac{\partial \kappa}{\partial y} + B\rho_l g\right]_{y=y_{end}} \end{aligned} \tag{28}$$

$$\begin{aligned} \dot{m}''_{hor} &= \left[\int_0^{\delta_2} \rho_l \cdot v_l \cdot dx\right]_{y=y_{end}} \\ &= \frac{\rho_l \cdot \delta_2^3}{3\mu_l}\left[\sigma_l \frac{\partial \kappa}{\partial y}\right]_{y=y_{end}} \end{aligned} \tag{28}$$

The analysis of mass transfer to the corner zones from two adjacent dissimilar thin film zones is a unique aspect of the current model. Zhao and Liao [52] were able to use the symmetry of a vertical channel leading to mass transfer interaction between similar thin films. Wang and Rose [55], on the other hand treated the corner zone by applying a circumferential pressure gradient through the use of polar coordinates. This approach, however, required that liquid thickness be measured in the radial

direction, resulting in thicknesses being measured oblique to the channel walls. As a result, the profiles of the condensate thickness and heat transfer coefficient along the walls showed discontinuity. In the present study, a bulk flow model is adopted for the corner zone (similar to Zhao and Liao [52]), where the radius of curvature is obtained from the momentum conservation equation. This analysis also allows the inclusion of mass flow from the neighboring thin film zones.

5.4 Vapor Core Flow

The flow in the vapor core is considered to be one-dimensional and along the axial direction, driven by the combined interaction of the vapor pressure gradient and the vapor-liquid interfacial shear stress. The change in vapor momentum due to the condensation is assumed to be negligible. Along the axial direction, the cross-sectional area of the vapor core will decrease due to continuous condensation, till the channel is flooded after complete condensation. With these assumptions and following the analysis of Zhao and Liao [52], the momentum conservation equation for the vapor core can be obtained as follows:

$$-\frac{dp_v}{dz} - \frac{\tau_i P_i}{A_v} = \frac{\rho_v}{A_v}\frac{d}{dz}\left(\bar{w}_v^2 A_v\right) \tag{29}$$

where p_v is the pressure in the vapor core, P_i is the perimeter of the liquid-vapor interface, A_v is the area of the vapor core, $\bar{w}$ is the mean velocity of the vapor core and τ_i is the shear stress at the liquid-vapor interface and expressed as,

$$\tau_i = \frac{1}{2}\rho_v \cdot \bar{w}_v^2 \cdot f_v$$

where, f_v is the friction factor and is expressed as

$$f_v = c \cdot Re_v^{-m}$$

with c and m being empirical constants. The values of c and m are taken as, c = 16 and m = 1 for laminar vapor flow, and c = 0.046 and m = 0.2 for turbulent vapor

flow. Re_v is the Reynolds number for the vapor flow, and expressed as

$$Re_v = \frac{\rho_v \cdot \bar{w}_v \cdot D_{hv}}{\mu_v}$$

The mean vapor velocity, $\bar{w}$, can be obtained from the energy conservation of the vapor flow. The energy balance can be obtained by equating the energy lost from the vapor core through condensation to the energy dissipated through the channel perimeter and can be expressed as,

$$\rho_v h_{fg} \frac{d}{dz}(\bar{w}_v A_v) = -h(z)(T_{sat} - T_w)[H + W] \tag{29}$$

where, ρ_v is the density of the vapor, $h(z)$ is the cross-sectional average heat transfer coefficient. The negative sign in Eq. 29 is applied to accommodate the reduction in the mass flow rate of the vapor flow ($\dot{m}_v$) along the axial direction ($\dot{m}_v|_{z_i} < \dot{m}_v|_{z_{i-1}}$). Wang and Rose [55] obtained the mean vapor velocity at each cross-section by subtracting the condensed mass flow rate from the inlet mass flow rate.

5.5 Heat Transfer Coefficients

The heat transfer coefficients are divided into three categories - the local average, the zone average and the overall cross-sectional average values. The local heat transfer coefficients are obtained for the thin film zone ($h_{lf}(y, z)$) with the following expression:

$$h_{lf}(y, z) = \frac{q_c''(y, z)}{T_{sat} - T_w} = \frac{\dot{m}_i h_{fg}}{T_{sat} - T_w} \tag{30}$$

where, $q_c''(y, z)$ is the local condensation heat flux at the liquid-vapor interface and $\dot{m}_i$ is the mass flow rate through the liquid-vapor interface. Replacing the mass flow rate at the liquid-vapor interface, $\dot{m}_i$ from Eq. 19 in Eq. 30, we get

$$h_{lf}(y, z) = \frac{(T_{iv} - T_w)/(T_{sat} - T_w)}{\frac{\delta}{k_l} + \frac{T_{sat}\sqrt{2\pi R_g T_{sat}}}{h_{fg}^2 \rho_v}\left(\frac{2-\nu}{\nu}\right)} \tag{31}$$

Then zone average heat transfer coefficient for the thin film zone, $\bar{h}_{lf}(z)$, can be obtained by integrating the local heat transfer coefficient for the length of the thin

film zone and can be written as,

$$\bar{h}_{lf}(z) = \frac{1}{L_j}\int_0^{L_j} h_{lf}(y,z)dy \tag{32}$$

where L_j is the length of the j^{th} liquid film zone (j = 1, 3, 5). In the corner zones, there will be a net mass flow of the condensate along the axial direction along with accumulation of the condensate from the neighboring zones due to capillary forces. In the absence of a suitable expression for heat transfer coefficient, the correlation of heat transfer coefficient around the perimeter for flow in the bottom portion of a horizontal tube, suggested by Rosson and Meyers [68], is applied to obtain the zone average heat transfer coefficient of the corner zone as:

$$h_{lc}(z) = \frac{\phi_{l,vt}(k_l/D_h)\cdot(8Re_{ls})^{1/2}}{5+5\left[ln(5Pr_l+1)\right]Pr_l^{-1}} \tag{33}$$

where, $\phi_{l,vt}$ is the two-phase multiplier for viscous (laminar) liquid flow and turbulent vapor flow, Re_{ls} is the superficial Reynolds number of the condensate flow in the channel, Pr_l is the Prandtl number of the liquid. Following Zhao and Liao [52], the parameters are expressed as follows,

$$\begin{aligned} Re_{ls} &= \frac{\rho_l \bar{w}_{ls} D_h}{\mu_l} \\ \phi_{l,vt} &= \sqrt{\frac{\Delta p_{lv}}{\Delta p_l}} = \sqrt{\frac{dp_v/dz}{dp_l/dz}} \end{aligned}$$

where, $\bar{w}_{ls}$ is the mean superficial liquid velocity, Δp_{lv} is the pressure drop of the two-phase flow and Δp_l represents the pressure drop of the liquid flowing alone in a rectangular channel, which can be expressed as:

$$\frac{dp_l}{dz} = \frac{P_{ch}}{A_{ch}}\tau_l$$

where τ_l represents the shear stress of the liquid flowing alone in the rectangular channel and is defined as:

$$\tau_l = \frac{6.65\mu_l \bar{w}_{ls}}{D_h}$$

Finally the cross-sectional average heat transfer coefficient, $h(z)$, is obtained by averaging the heat transfer coefficients of the liquid-film and corner-liquid zones with the following relationship,

$$h(z) = \frac{\bar{h}_{lf,1}.L_1 + h_{lc,2}.P_{c,2} + \bar{h}_{lf,3}.L_3 + h_{lc,4}.P_{c,4} + \bar{h}_{lf,5}.L_5}{H + W} \tag{32}$$

5.6 Numerical Solution

The mass, momentum and energy conservation equations are implicit in nature, as all the parameters are not known in a particular step in z. As such an iterative approach is adopted, which obtains the process parameters initially with respect to previous axial position values and then with subsequent iterations, the converged values of the process parameters are arrived for the next axial position. This process is repeated until the convergence criterion is satisfied at each step in the axial direction. In the present model, the liquid and vapor phases are treated separately and the respective conservation equations of the two phases are coupled with respect to common system parameters like heat transfer coefficient and interfacial parameters like saturation temperature, shear stress etc. In every step along the axial direction, conservation is sought in the mass, momentum and energy equations of respective phases.

The variation in the axial direction (z) is expressed by discretizing the variation using forward finite difference method with an increment of Δz. Eq. 20 describes the profile of the liquid-vapor interface for the thin liquid zones. However, at each axial location, the analysis is done with parameter values from the previous axial step. So at each axial location, the profile is defined by a fourth order ordinary differential equation.

5.6.1 Solution Procedure

The mass, momentum and energy conservation equations of the liquid and vapor core are inter-dependent. A unique solution procedure has been adopted, which calculates

the process parameters at z_i step through an iterative approach by simultaneous solving of the governing equations, initializing with the process parameters from previous axial position, z_{i-1}. The iterative approach is continued until the convergence criterion is satisfied at each step in the axial direction. The profiles of the liquid-vapor interface for zones 1, 3 and 5 are expressed by Eq. 20, which is a non-linear fourth order ordinary differential equation (as parameter values are known at previous z_{i-1} step) and represents a boundary value problem (BVP). Eq. 20 is expressed as a series of linear ordinary differential equations and then solved using non-linear Newton-Raphson method.

The vapor is considered to be at saturated condition at the inlet of the channel. The saturation temperature of the vapor is interpolated from standard steam tables. The solution procedure is as follows:

1. $z = \mathbf{0}$: Initial conditions at the inlet of the condenser are utilized to obtain the liquid-vapor interfacial profile for the thin liquid zones 1, 3 and 5.

   - The initial vapor pressure gradient at $z = 0$ is obtained from the following relation:

     $$\frac{dp_v}{dz} = -f_v \frac{2G^2\chi^2}{\rho_v D_h}$$

     where, χ is the vapor quality, and

     $$f_v = cRe_v^{-m} \begin{cases} \text{c} = 16 & \text{m} = 1 & \text{laminar flow} \\ \text{c} = 0.046 & \text{m} = 0.2 & \text{turbulent flow} \end{cases}$$

   - Next the liquid-vapor profiles of zone 1 and 5 are solved. The radii of curvature, $r_{c,2}$ and $r_{c,4}$ are assumed to be 10% of the channel width. According to the assumptions, $\delta_{3,0} = \delta_{1,1} = 0$. Then liquid-vapor profiles of zone 1 and 5 are obtained from Eq. 22.

   - The length of zone 3 is obtained and the interface profile is solved using the boundary conditions described earlier.

- After obtaining the liquid-vapor interface profile, the following parameters are obtained: $A_{lc,2}$, $A_{lc,4}$, A_v, dp_v/dz, Re_v, τ_i, χ and α.
- $\bar{w}_{lc}$ obtained from continuity:

$$\bar{w}_{lc}A_{lc}\rho_l + \bar{w}_v A_v \rho_v = \dot{m}_v$$

- Finally, the local averaged heat transfer coefficients, $h_{lf}(z), h_{lc}(z)$ and $h(z)$ are obtained using the above parameters.

2. $z = z + \Delta z$: Next axial vapor pressure gradient is obtained from the guessed vapor pressure.

3. Areas of the corner zones are obtained by simultaneously solving Eq. 24 and Eq. 26. The new radii of curvature ($r_{c,2}$ and $r_{c,4}$) are obtained from the corner areas, $A_{lc,2}$ and $A_{lc,4}$ respectively. .

4. The profiles of the thin liquid zones (1, 3 and 5) are solved using $r_{c,2}$, $r_{c,4}$.

5. The local and overall average heat transfer coefficients are then obtained. $D_{lc,2}$, $D_{lc,4}$, D_{hv} are updated. Subsequently, the average vapor velocity, w_v is obtained from Eq. 29. Re_v, τ_i, χ and α are updated.

6. Finally the vapor pressure gradient for the current axial location is obtained using Eq. 29. If the value didn't match with dp_v/dz obtained from the guessed pressure at step 2 or from previous iteration within a specified tolerance (10^{-5}), process is repeated from step 3.

7. The solution is then taken to the next axial location and the steps are repeated along the axis.

5.7 Summary

In this chapter, a detailed analytical model was developed for simulating condensation in a rectangular microchannel. The model describes an iterative approach

incorporating successive solution of mass, momentum and energy balance equations for both liquid and vapor phases. The condensate layer along the wall is divided into five distinct regions - thin liquid layers along top, vertical and bottom wall, and the corner zones at the top and bottom. The liquid-vapor interface profile is expressed as a 4th order non-linear differential equations, which was solved using non-linear Newton-Raphson technique by discretizing the equations using finite difference method. The basic features of the condensation model are as follows:

1. The effect of surface tension and gravity is incorporated in describing the transport of the condensate film.

2. The heat and mass transfer in the corner zones takes into account the mass transfer between the film zones and the corner zones and also the mass transport occurring through the liquid-vapor interface due to condensation.

3. The heat transfer in the film zone along the wall is considered to be conduction dominated.

CHAPTER VI

RESULTS OF CONDENSATION MODELING

Five different geometries were considered - square section of 300 μm (300W $\times$ 300H, $D_h = 300\ \mu m$) and rectangular sections of 300 $\times$ 500 μm (300W $\times$ 500H, $D_h = 375\ \mu m$), 500 $\times$ 300 μm (500W $\times$ 300H, $D_h = 375\ \mu m$), 100 $\times$ 300 μm (100W $\times$ 300H, $D_h = 150\ \mu m$) and 300 $\times$ 200 μm (300W $\times$ 200H, $D_h = 240\ \mu m$). Saturated steam at 100 ^{o}C temperature is introduced at the inlet of the channel (Figure 34) for uniform wall temperatures of 92 and 96 ^{o}C. The thermophysical properties of water necessary for calculation are listed in Table 14.

6.1 Thin liquid film profiles

Figure 37 shows the liquid film profiles of zone 1 at five different locations (z = 1 mm, 8 mm, 16 mm, 24 mm and 32 mm from the inlet of the channel) along the axial length of a square channel (300 $\times$ 300 μm). Zone 1 occupies most of the length of the top wall near the channel inlet, and gradually decreases along the axial length. The thickness of the liquid film increases along the axial direction due to accumulation of the condensate. Similar phenomenon also happens for the bottom wall. Eventually, the thin film zones end and the corner zones occupy all the surfaces of the channel. Apparently, in Figure 37 the profiles of the thin film zone appear parallel to the horizontal wall. However, a closeup in Figure 38 reveals a curve whose curvature changes sign in the middle of the zone (profile shown at inlet). The surface tension force acting parallel to the wall, which draws in liquid towards the corner zone is considered to be responsible for this profile. Similar kind of profile is also seen in [52], where triangular channels of dimensions 1-2 mm were used to model the condensate profile. The axial variation of the profile for the half-section of the channel is shown in

Table 14: Thermophysical properties of water

Gas constant, R_g	462 (J/kg-K)
Dispersion constant, β	2.0×10^{-21} (J)
Accommodation coefficient, γ	0.03
Surface tension, σ_l	0.05886 (N/m)
Latent heat of vaporization, h_{fg}	2257.1×10^3 (J/kg)
Liquid specific heat, c_{pl}	4220 (J/kg-K)
Density of liquid, ρ_l	958.4 (kg/m^3)
Density of vapor, ρ_v	0.5977 (kg/m^3)
Dynamic viscosity of liquid, μ_l	2.825×10^{-4} (N-s/m^2)
Dynamic viscosity of vapor, μ_v	1.202×10^{-5} (N-s/m^2)
Thermal conductivity of liquid, k_l	0.683 (W/m-K)
Prandtl number of liquid, Pr_l	1.75

Figure 39. The increase in the radii of the corner zones is visible, with corresponding decrease in length of the thin film zones. The thicknesses of the top and bottom layers are nearly identical. This shows that the effect of gravity is almost negligible in condensation in rectangular microchannels, and the liquid movement is entirely driven by surface tension.

6.2 Heat transfer coefficients

As seen in Figure 40, the local heat transfer coefficient of the thin film zone is inversely proportional to the thickness of the condensate layer, and is seen to decrease along the axial length. Correspondingly, the corner liquid zone increases in area through mass accumulation from condensation and mass transfer from the thin film zones due to surface tension driven flow lateral to the channel cross-section, which reduces the heat transfer coefficient along the length of the channel (represented by the lines at the bottom of the graph). The enhancement of the thin film zone is clearly seen by comparing with the heat transfer coefficient of the corner zone at each axial location. The discontinuity (sudden drop in heat transfer coefficient values) noticed at the interface of the film zone and corner zone is due to the difference in

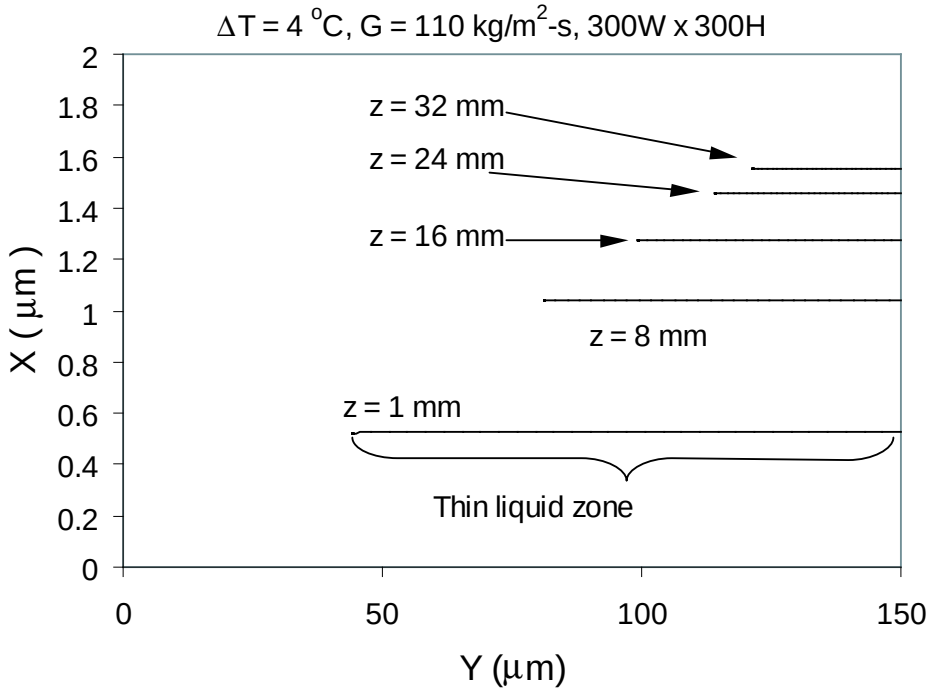

Figure 37: Thickness of condensate in Zone 1 at various axial locations

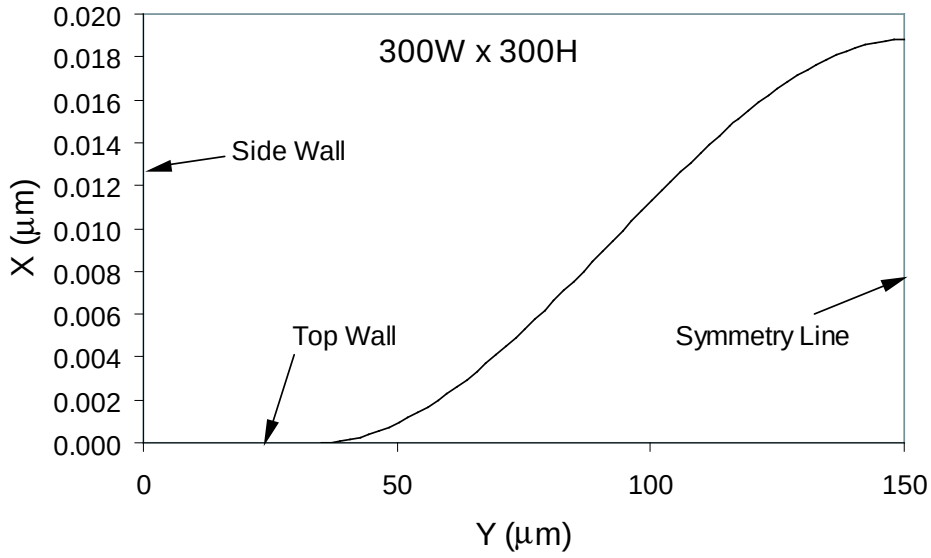

Figure 38: Close-up of the thin film profile in Zone 1

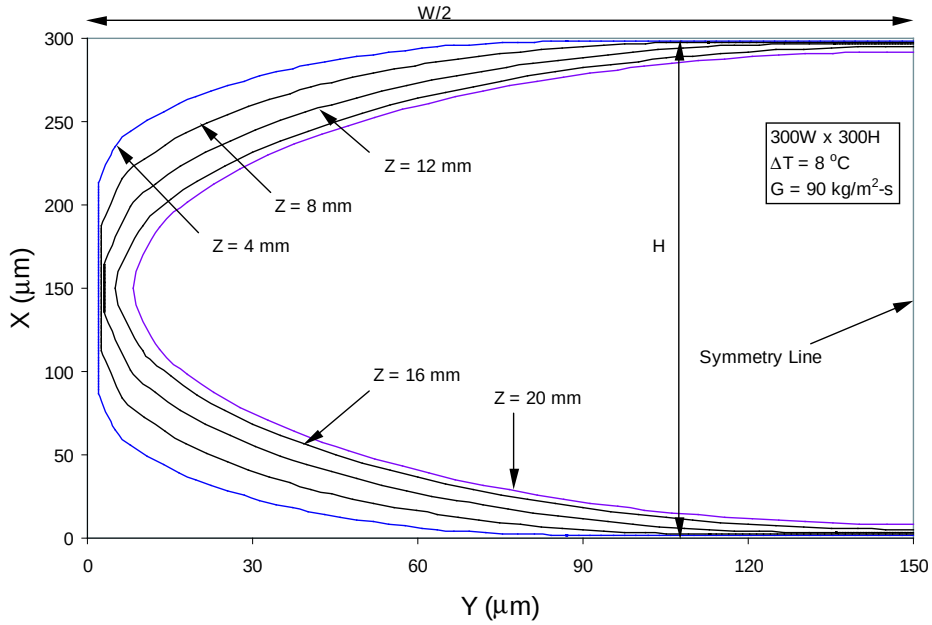

Figure 39: Condensate profiles for half-section channel along axial length

numerical treatments of an one-dimensional analysis for the corner zones compared to a two-dimensional analysis for the thin film zones. The calculation of heat transfer coefficients of the thin film zone and the corner liquid zone from two separate analysis is similar to the analysis done by Zhao and Liao [52], who also noticed a similar discontinuity in heat transfer coefficients of the separate zones. However, Wang et al. [53] used polar coordinates in the corner region to obtain a continuous profile of the heat transfer coefficient, which has the drawback of defining thickness oblique to the corner walls.

In Figure 41 the variation of the average heat transfer coefficient for the thin-film ($h_{lf,1}$) and corner liquid zone ($h_{lc,2}$) of the square-section channel are shown for the case of G = 90 kg/m^2-s and $\Delta T_i = 8\ ^o$C. Correspondingly, on the secondary axis, the radius of curvature ($r_{c,2}$) and the length of zone 1 (L_1) are shown. Along the axial direction, we can see that the length of the thin film zone is decreasing, along with a corresponding increase in the radius of curvature of the adjacent corner liquid zone.

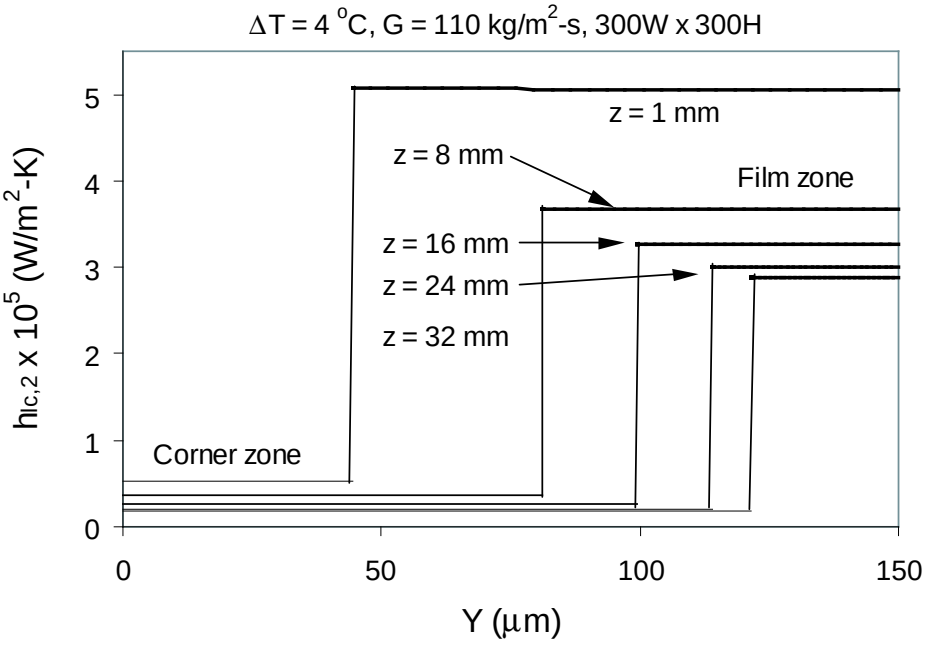

Figure 40: Local heat transfer coefficient in Zone 1 and 2 at various axial locations

Similar behavior is also noticed for the other thin liquid zones (zone 2 and 4) and the corner liquid zone 4. This is due to the condensation of vapor along the axial length, which gets drained into the corner zones. From the figure, we also observe the monotonic decrease of the heat transfer coefficients of the thin liquid zone ($h_{lf,1}(z)$) and the corner liquid zone ($h_{lc,2}(z)$). The effect of surface tension is clearly visible in the attainment of high values of heat transfer coefficient in the thin film zone. As the two-phase mixture moves downstream, the enhancement seems to fade away with gradual thickening of the film, which is visible from the gradual decrease of slope of the heat transfer coefficient. Along the axial direction, the gradual thickening of the corner liquid zone is also reflected in the monotonic decrease of the heat transfer coefficient, $h_{lc,2}(z)$.

The enhancement in heat transfer achieved due to the thin film formation in the square channel can be better noticed through a comparison with a heat transfer correlation for a circular tube having same hydraulic diameter (300 μm) as the square

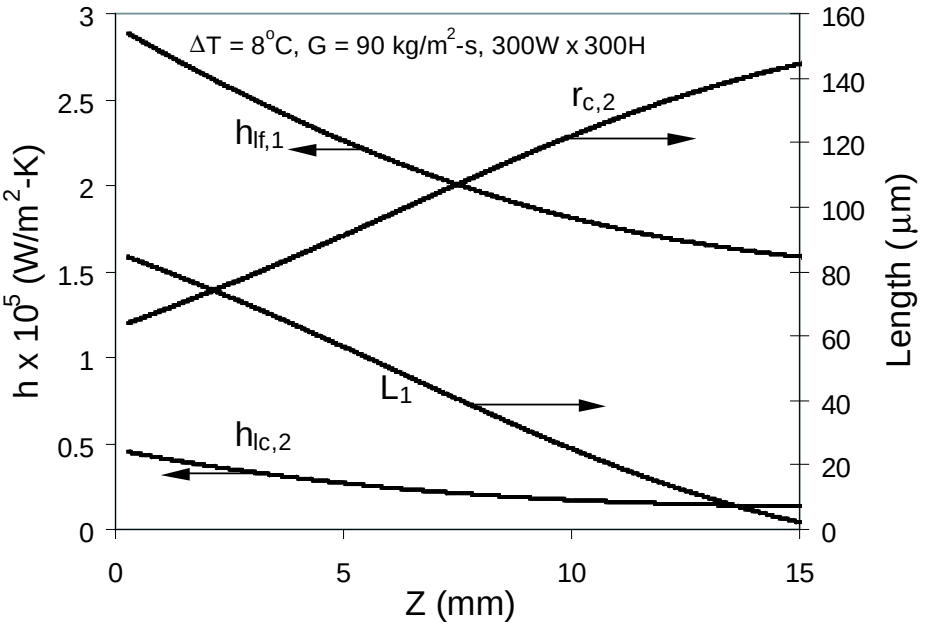

Figure 41: Variation of average heat transfer coefficients ($h_{lf,1}$ and $h_{lc,2}$), corner radius ($r_{c,2}$) and length of film zone (L_1) at various axial locations

channel (Figure 42). The Shah correlation [69] is used for the comparison at an inlet subcooling of 8 ^oC and inlet mass flow rate of G = 70 kg/m^2-s. The heat transfer coefficient for the square-section channel is significantly higher compared to the circular channel in the initial section of the channel (until 12 mm from the inlet). This enhancement in the initial length is primarily due to the presence of thin film zones. With continuous accumulation of condensation along the axial length, the film zones end, and the channel gets flooded with the corner zones occupying all the surfaces of the channel. This change is reflected in the flattened profile of the heat transfer coefficient after z = 12 mm. From this point onwards, the order of the heat transfer coefficient for the square channel is similar to that of the circular channel. This shows the influence of surface tension in shaping the interface profile through the formation of the thin film zone and thus achieving a very high heat transfer coefficient, compared to the continuous annular profile of the bulk condensate flow obtained in a circular channel.

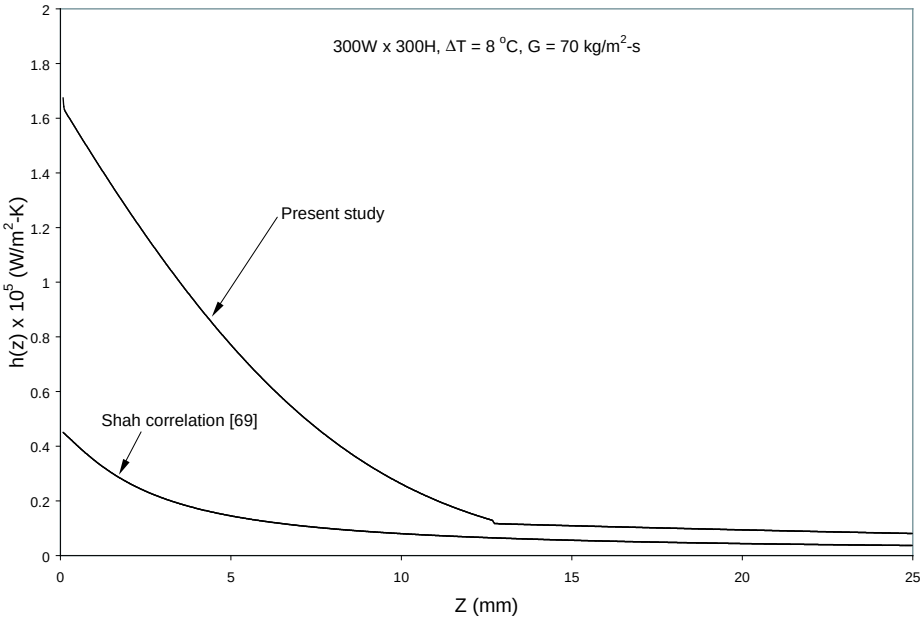

Figure 42: Comparison of cross-sectional average heat transfer coefficient

The effect of inlet mass flow rate and inlet subcooling on the profile of the liquid-vapor interface of zone 1 for a square channel (300 μm $\times$ 300 μm) is shown in Figure 43. Two inlet flow-rates of 70 kg/m^2-s and 90 kg/m^2-s, which correspond to Reynolds number of 1500 and 1950 respectively, and inlet subcooling of 4 ^{o}C and 8 ^{o}C are imposed at the inlet of the channel. The profiles are obtained at $z = 10$ mm from the inlet of the channel. With an increase in mass flow rate (keeping inlet subcooling constant), the thickness of the condensate in the thin film region decreases. The length of the thin film zone also increases with an increase in mass flow rate, with a corresponding decrease in the area of the corner zone. The higher vapor velocity associated with a higher inlet mass flow rate, will exert more shear stress on the liquid-vapor interface, resulting in more liquid being carried downstream with a decrease in the condensate layer thickness. The thinner liquid film at higher mass flow rate produces a higher heat transfer coefficient, as shown in Figure 44. On the other hand, an increase in inlet subcooling (keeping inlet mass flow rate constant) is associated

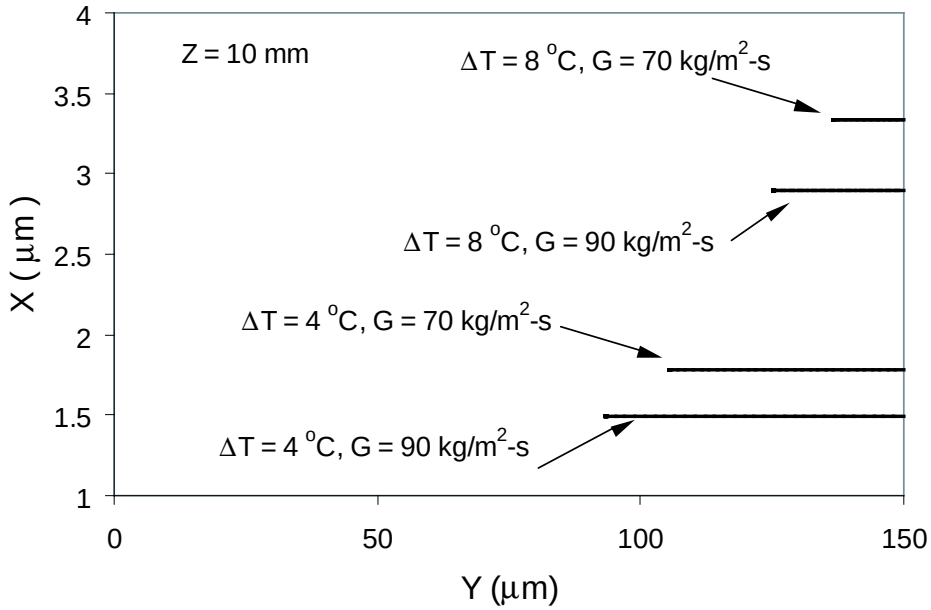

Figure 43: Effect of inlet mass flow rate and inlet subcooling on thickness of condensate

with an increase of film thickness along the axial direction. Higher inlet subcooling induces more condensation, which increases the condensate thickness, resulting in a decrease in heat transfer coefficient, as seen in Figure 44. Zhao and Liao [52] also obtained higher heat transfer coefficient for higher inlet Reynolds number, which they attributed to the longer thin film zone obtained at higher Reynolds number. Similar to the present results, they also found that a decrease in the inlet subcooling (keeping inlet Reynolds number constant) resulted in a higher heat transfer coefficient compared to a larger inlet subcooling.

Figure 45 depicts the effect of inlet mass flow rate (G = 70 kg/m^2-s and 90 kg/m^2-s) and inlet subcooling (ΔT = 4 ^{o}C and 8 ^{o}C) on the cross-sectional average heat transfer coefficient for a square channel (300 μm × 300 μm). An increase in the inlet mass flow rate (keeping inlet subcooling constant) shows an increased average heat transfer coefficient in the channel. The higher mass flow rate generates a thinner condensate layer in the channel, due to the higher shear stress applied on the liquid

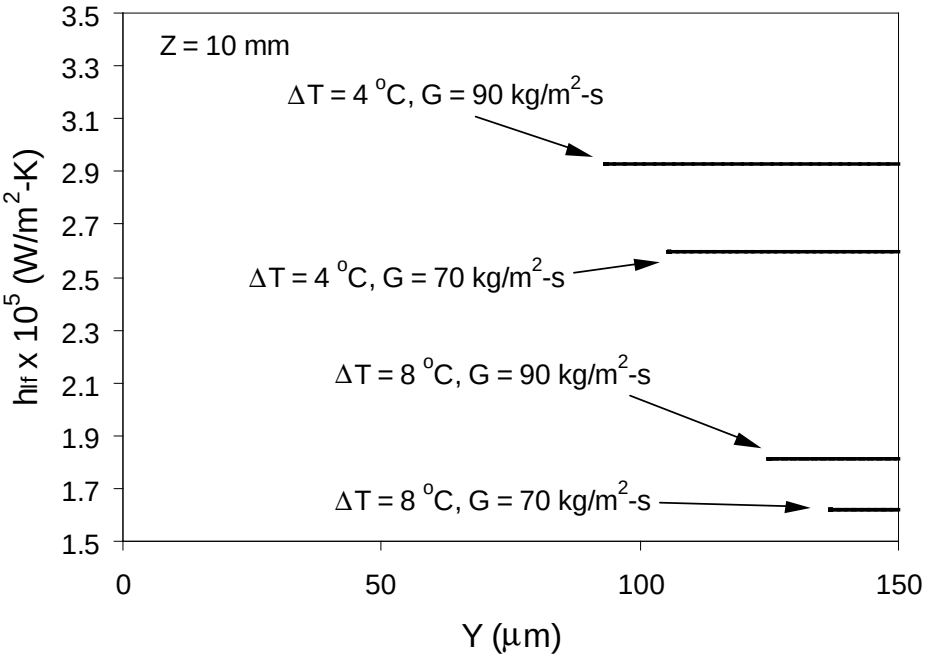

Figure 44: Effect of inlet mass flow rate and inlet subcooling on local heat transfer coefficient

by the vapor core, resulting in higher heat transfer coefficient. However, with gradual build-up of condensate causes a gradual decline in the average heat transfer coefficient. This behavior is common for both the inlet subcooling of 4 ^{o}C and 8 ^{o}C. On the other hand, with an increase in inlet subcooling (keeping inlet flow rate constant), the average heat transfer coefficient is found to decrease. A larger subcooling leads to a thicker condensate layer (Figure 43) resulting in lower local heat transfer coefficient (Figure 44). Along the axial direction, the rate of decrease in heat transfer coefficient monotonically decreases, as the flow regime transfers from film based to annular flow. A similar decline in average heat transfer coefficient with increased inlet subcooling was reported by Zhao and Liao [52]. They found that the increase in inlet flow rate (higher Reynolds number) exerted higher shear stress on the liquid layer and extended the length of the condensate layer along the axial direction. Wang and Rose [55] also reported a decline in mean heat transfer coefficient with increasing "vapor-to-surface"

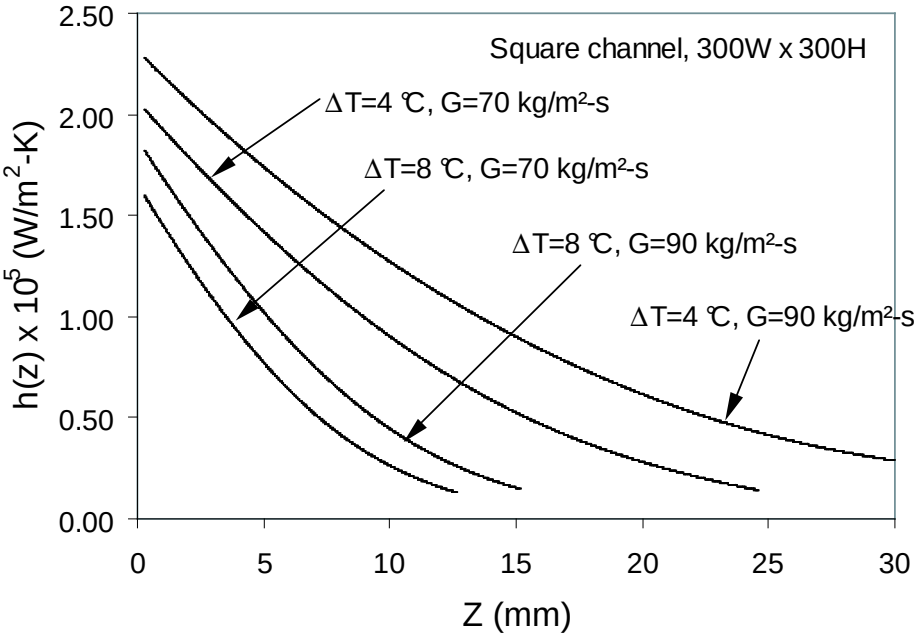

Figure 45: Effect of inlet mass flow rate on cross-sectional average heat transfer coefficient

temperature difference.

The effect of channel sizes on the cross-sectional average heat transfer coefficient is shown in Figure 46 for three channel dimensions (300 μm × 300 μm, 300 μm × 500 μm and 500 μm × 300 μm) for a subcooling of ΔT = 4 ^{o}C at mass flow rate, G = 90 kg/m^2-s. The graphs depict the values before the end of the thin film zones and beginning of the annular flow regime, where the top and bottom walls get "flooded" by the gradual increase in the corner zones. The thin film zones (top and bottom walls) of the wider channel and the taller channel (vertical wall) are extended beyond that available in the square-section channel, which delays the flooding of the channel (end of thin film zones) for the wider and taller channel. As a result, the average heat transfer coefficient is higher for both the wider and taller channel with respect to the square-section channel. The enhancement in heat transfer is approximately 1.5 times, which starts to decrease beyond 20 mm from the inlet. The taller channel (300 μm × 300 μm) shows slightly higher heat transfer coefficient than

the wider channel (500 μm × 300 μm) till 15 mm from the inlet, after which the behavior reverses. Similar behavior is also noted for an lower mass flow rate of G = 70 kg/m^2-s. This behavior can be explained by studying the local condensate thickness and heat transfer coefficients, as shown in Figure 47 and Figure 48. For a larger channel, because of higher surface area, the condensate thickness will be less compared to a smaller channel. This behavior is seen in Figure 47 from the thickness profiles as the height of the channel is increased. Similar decrease in condensate thickness and corresponding increase in local heat transfer coefficient is also noticed for the wider channel. Zhao and Liao [52] also noted a similar decline in the cross-sectional average heat transfer coefficient along the axial direction with reduction in the channel dimensions, however in the initial region of the channel, they found that surface tension plays a role in increasing the heat transfer coefficient for the smaller sized channel (equilateral triangular channel with dimension of 1 mm compared to a 2 mm channel).

6.3 Two-phase pressure drops

Figure 49 presents the variations of two-phase pressure drops in the square-section horizontal microchannel along the axial distance for mass fluxes of 70 kg/m^2-s, 90 kg/m^2-s and 110 kg/m^2-s, at inlet subcooling of 4 ^{o}C. With increase in the mass flow rate, the shear stress experienced at the liquid-vapor interface also increases, which leads to a higher two-phase pressure drop. Moreover, higher inlet mass flow rate allows faster heat transfer in the axial direction from the vapor to the channel walls (Figure 44), which leads to quicker condensation of the vapor flow. This leads to a quicker reduction in the velocity of the vapor, and thus the pressure drop in the channels decreases more rapidly.

In Figure 50 the effect of channel geometry on the two-phase pressure drop is shown for a mass flux of G = 70 kg/m^2-s at an inlet subcooling of 4 ^{o}C. A decrease in

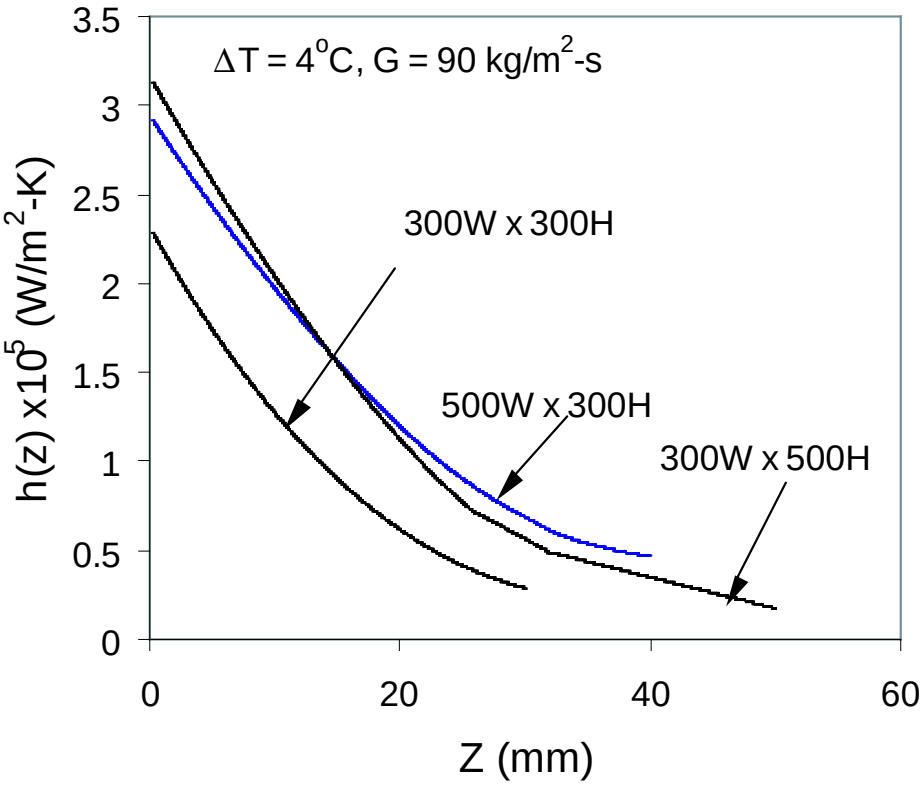

Figure 46: Effect of channel geometry on cross-sectional average heat transfer coefficient

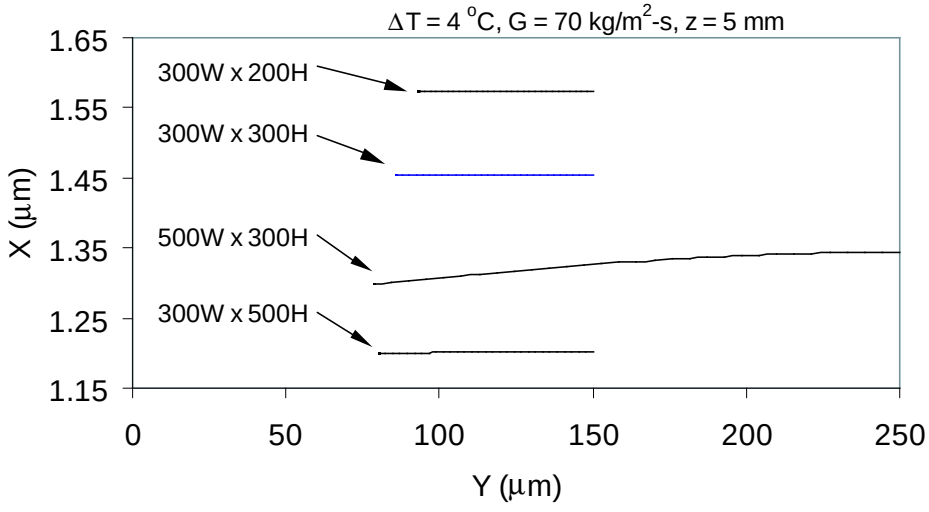

Figure 47: Effect of channel geometry on thin film zone thickness

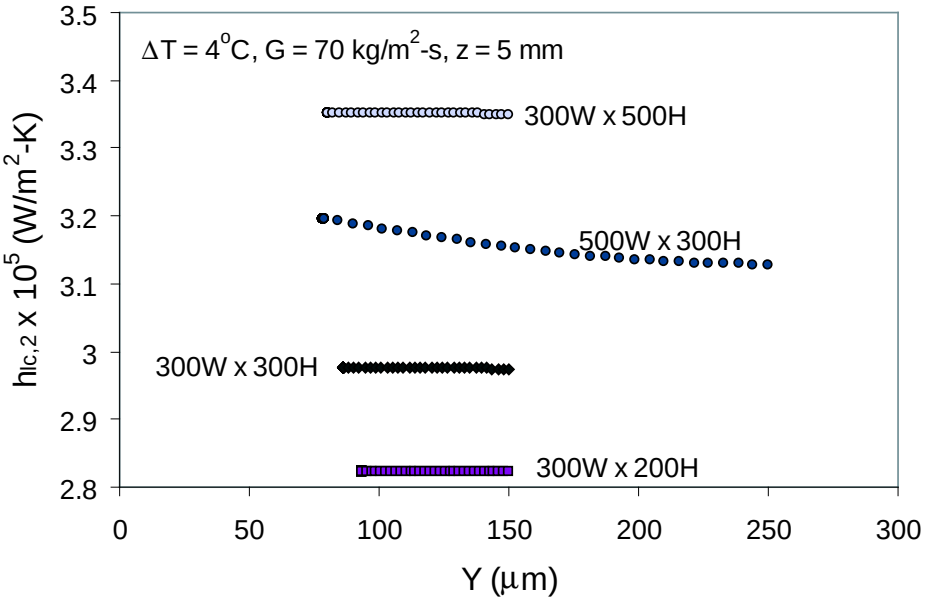

Figure 48: Effect of channel geometry on local heat transfer coefficient

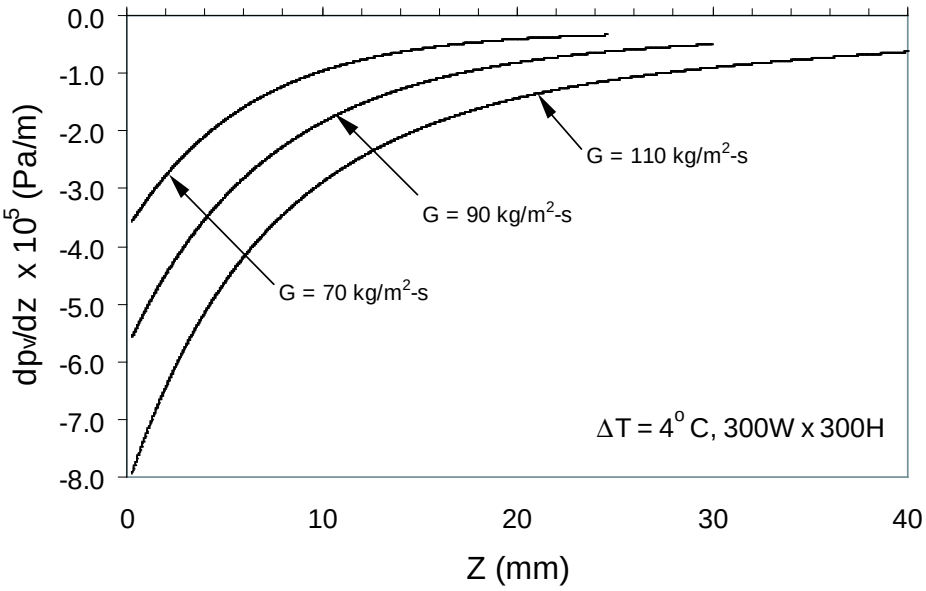

Figure 49: Effect of inlet mass flow rate on pressure drop across the channel

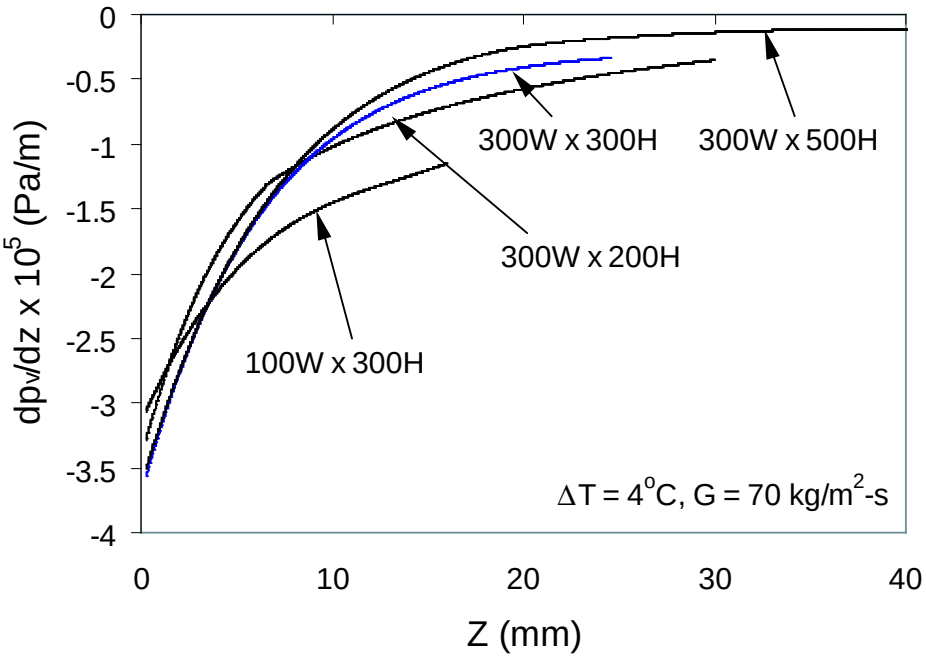

Figure 50: Effect of channel geometry on pressure drop across the channel

the height of the channel from 500 μm to 200 μm increased the pressure drop roughly two times after 10 mm from the inlet. For a particular mass flux, velocity of the vapor core will be more in the case of smaller cross-section channel, which will induce higher interfacial shear stress resulting in higher pressure drop. The observed trend in the pressure drop shows that the model have been able to capture the physics of the condensation properly.

6.4 Comparison with existing literature

In the absence of a suitable empirical correlation describing condensation in rectangular microchannels, the current model is compared with the condensation model of Wang and Rose [55] and with the experimental results of Garimella and Bandhauer [70], Shin and Kim [71] and Cavallini et al. [72]. A baseline case is considered with a 1 mm $\times$ 1 mm square cross-section horizontal channel, with R134a as the working fluid for G = 500 kg/m^2-s, $\Delta T = 4$ ^{o}C and $T_{sat} = 50$ ^{o}C. In Figure 51,

the axial variation of overall heat transfer coefficient and quality is shown. Wang and Rose [55] noticed a sharp decline in the heat transfer coefficient until 50 mm from the channel inlet and then a constant value until 200 mm along the axial direction. They believed that surface tension might be responsible for producing a uniform heat transfer coefficient between 50 mm-200 mm. However, the current model predicts a gradual decline in heat transfer coefficient along the channel length. A similar trend as the present study is also noticed by Lu and Suryanarayana [73]. Continuous condensation along the channel length will increase the cross-sectional area of the corner liquid zone, as well as increase the thicknesses of the thin film zones, thus decreasing the heat transfer coefficient. In this respect, it is believed that the current study depicts a more realistic variation of heat transfer coefficient. The variation in quality shows similar trend for both the studies. Since quality is related to the mass of liquid, the above results might suggest that the mathematical treatment of the different zones is responsible for different distribution of liquid along the wall, thus affecting the overall heat transfer coefficient.

In Figure 52 the variation of Nu with quality is shown. The Nu predictions from the current model are seen to follow the trend shown by Garimella and Bandhauer [70] and Shin and Kim [71]. Within a quality range of 0.2-0.8, current results show similar variation with respect to Garimella and Bandhauer [70]. However, the Nusselt number variation at the entry region of the channel cannot be compared as the experiments were conducted with partially condensed vapor at the inlet. The current model under-predicts the heat transfer coefficient data of Cavallini et al. [72], who used a multi-port channel condenser. This result corroborates with the numerical simulation of Cavallini et al. [72], who observed similar behavior for G $>$ 600 kg/m^2-s. Moreover, the unknown mass flow rate through each channel may also contribute to the discrepancy in the measured and predicted heat transfer coefficient values.

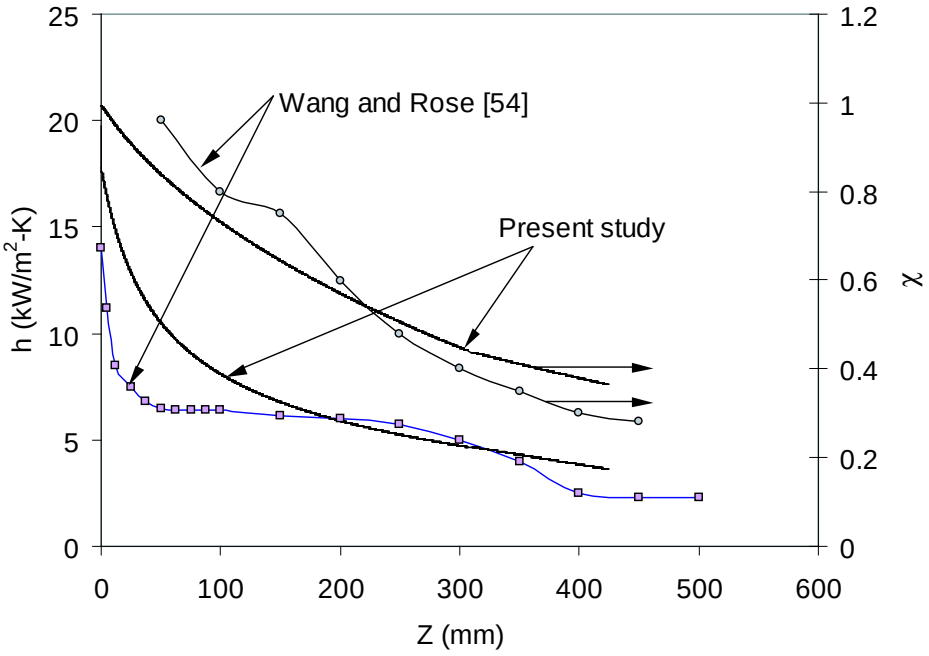

Figure 51: Comparison of heat transfer coefficient and quality vs. axial channel length

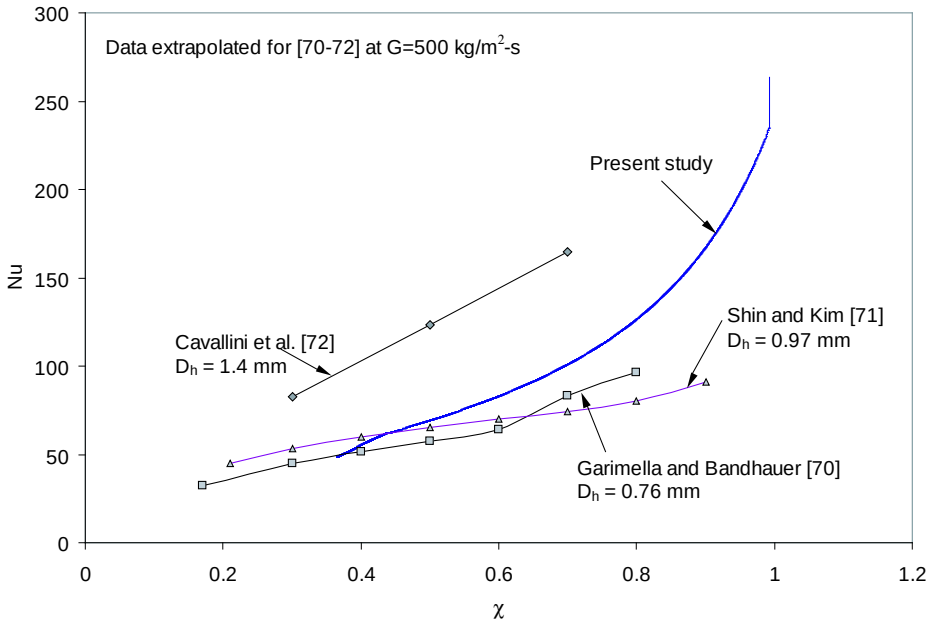

Figure 52: Comparison of Nusselt number vs. quality

6.5 Summary

A detailed analytical study on the condensation in rectangular microchannel has been discussed in this chapter. The present model takes into account the effect of surface tension, gravity, vapor pressure gradient, interfacial shear stress, saturation temperatures and interfacial thermal resistance. The primary findings from the study are as follows:

1. Significantly higher heat transfer coefficient is obtained for the rectangular channel compared to condensation in a circular channel, as long as thin film zones are sustained along the walls.

2. Increase in the mass flow rate at the channel inlet is associated with higher interfacial shear stress on the liquid-vapor interface, which results in sustaining thin film zones in the early part of the channel, which leads to a higher condensation heat transfer coefficient and thus a thicker film in the later part of the channel. This also results in a higher vapor pressure drop.

3. Increasing the inlet subcooling results in a thicker film in the channel, which is responsible for a gradually decreasing heat transfer coefficient along the channel.

4. Increasing the channel dimensions is responsible for increasing the length of the thin film zones, which also results in increased heat transfer coefficient.

5. Increase in channel dimensions is related to lower vapor pressure drop. This is attributed to the higher Reynolds number achieved in a smaller channel at similar inlet flow rate. As a result, a channel of smaller cross-section will experience a higher pressure drop.

CHAPTER VII

CONCLUSIONS, UNIQUE CONTRIBUTIONS AND RECOMMENDATIONS FOR FUTURE WORK

A dual chamber thermosyphon is a compact device, which incorporates boiling and condensation and can dissipate high heat fluxes. A fundamental understanding of the boiling and condensation phenomena in confined regions is required for designing such systems. The present work identified the boiling of water at sub-atmospheric pressures and condensation in microchannels as two important areas needing detailed study to aid in designing evaporator and condenser for optimized performance (Chapter 1).

A detailed test setup was designed and assembled for carrying out experiments on boiling with water at sub-atmospheric pressures using boiling enhancement structures. The pressure was varied from 9.7 kPa to 21 kPa, with heat fluxes varying from 0-105 W/cm^2. A porous boiling enhancement structure (12.7 mm $\times$ 12.7 mm) was used, whose height was varied from 1-6 mm. The initial height of the working fluid in the evaporator was also varied from 20-39 mm, corresponding to fill-ratios of 0.5-0.9 respectively (Chapter 2). The effect of the sub-atmospheric pressures and the enhancement structure geometry on the boiling heat flux was studied for varying heat fluxes, and compared with the boiling heat transfer from a plain surface. The results were also compared with existing literature and the observations from the comparison are discussed. A model was also developed for the surface heat flux, based on the experimental heat transfer coefficient and the numerical results were compared with the experimental results (Chapter 3). The effect of the liquid-fill level on the boiling heat transfer at varying pressures and geometries of the enhancement structure is discussed and compared with existing literature (Chapter 4).

A detailed analytical study on the condensation in rectangular microchannel (D_h = 150 μm to 375 μm) has been undertaken, which involved an iterative solution approach of the mass, momentum and energy equations of liquid and vapor phases. The present model takes into account the effect of surface tension, gravity, vapor pressure gradient, interfacial shear stress, saturation temperatures and interfacial thermal resistance (Chapter 5). The effect of the inlet flow rate, channel dimensions and inlet subcooling were investigated and the results were also compared with existing models and correlations on condensation (Chapter 6).

7.1 Conclusions

7.1.1 Effect of enhancement structure and sub-atmospheric pressures on the thermal performance

The current study showed that boiling enhancement structure geometry plays an important part in influencing the thermal performance of a thermosyphon. The operating system pressure also influences the thermal performance. The following conclusions can be drawn from the experimental results:

1. Boiling at sub-atmospheric pressures results in lowering of saturation temperature, which leads to lower wall temperatures. Heat fluxes greater than 100 W/cm^2 can be achieved through boiling at sub-atmospheric pressures, while keeping the surface temperatures below the threshold temperature of 85 ^{o}C.

2. Incipience superheat was found to be negligible for boiling at sub-atmospheric pressures with enhanced structures. All the boiling curves exhibited monotonic behavior throughout the range of heat fluxes for all the experimental runs.

3. The heat transfer coefficient increased with an increase in the operating pressure. This behavior is more apparent at the higher heat flux range (> 50 W/cm^2), where increased heat transfer coefficient was noticed with a slower rate of change in wall superheat.

4. The lowering of surface temperature with decrease in pressure is offset by the deterioration of heat flux with lowering of pressure. The bubble generation physics plays an important part in this scenario. In this respect, the current results corroborate previous investigations on boiling of water at low pressures, which concentrated on visualization of bubble generation at low pressures.

5. The enhancement structure is found to increase the heat flux with respect to boiling from a plain surface at sub-atmospheric pressures. However, as the height of the structure was increased beyond single layer, the heat transfer coefficient reduced. This implies the existence of an optimum height of the structure, which will achieve the maximum heat transfer corresponding to a particular saturation pressure.

6. The enhanced structure achieved improved performance with respect to the plain surface and also increased the CHF.

7. With increase in the operating pressure, the enhancement in heat transfer achieved by the porous structure over the plain surface tends to decrease.

7.1.2 Effect of liquid-fill level on the thermal performance

Contrary to existing literature, in the present study, the liquid fill-level is found to influence the heat transfer characteristics. The following conclusions can be drawn from the experimental results:

1. For boiling from a plain surface, a reduction in liquid fill-levels increases the heat transfer with a corresponding increase in CHF also. It is found that the change in liquid-fill levels has a more pronounced effect for the higher pressure case (21 kPa), whereas for lower pressures (9.7 and 15 kPa), the effects are negligible.

2. The heat transfer is observed to be dependent on the liquid level for boiling with enhanced structures. At 21 kPa pressures, vigorous boiling activity was noticed in the evaporator, which generated a lot of agitation in the top surface of the pool, resulting in the reduction of the effective height of the pool. The height difference between the liquid level and the top of the structure influences the hydrostatic pressure head on the boiling surface and thus affect the bubble generation. A reduced effective pool height would also lead to a decrease in the net buoyancy force exerted on the bubbles for dislodging from the boiling surface. This would reduce the heat flux from the surface. On the other hand, higher buoyancy force will thus aid in bubble generation and increased heat transfer.

3. Results from the study on structures having 1, 4 and 6 layers suggest that an optimum liquid level might exist for each structure. With increase in the height of the structure, the liquid level producing the best performance is also seen to increase.

4. For lower fill levels, vigorous boiling at higher heat fluxes (> 60 W/cm^2) might prevent the liquid from wetting the structure. As a result, the performance would be worse for such cases.

5. The height of the evaporator significantly contributes to the transport of working fluid from the evaporator to the condenser through entrainment in the connecting tubing. For high liquid fill levels, the entrained liquid will reach the condenser resulting in reduction of condensation heat transfer. This result also suggests an optimum liquid fill level for the structure-evaporator configuration.

7.1.3 Condensation in rectangular microchannels

The principal conclusions from the study of condensation in rectangular microchannels are:

1. Significantly higher overall heat transfer coefficient is obtained for the rectangular channel compared to condensation in a circular channel of similar hydraulic diameter, as long as thin film zones are sustained along the walls. After the rectangular channel gets "flooded" (no thin film zone exists along the walls), the order of magnitude of the heat transfer coefficient for the rectangular and circular channels are approximately similar.

2. With increase in the thickness of the condensate along the channel, the local heat transfer coefficients of the thin film zone (along the walls) and the corner liquid zones decreases monotonically.

3. Increase in the mass flow rate at the channel inlet is associated with higher interfacial shear stress on the liquid-vapor interface, which results in sustaining thin film zones in the channel. As a result, higher inlet mass flow rate results in higher overall heat transfer coefficient.

4. Increasing the inlet subcooling results in a thicker film, which is responsible for a lower heat transfer coefficient compared to the case with lower inlet subcooling.

5. Increasing the channel dimensions is responsible for increasing the length of the thin film zones, which also results in increased overall heat transfer coefficient, compared to a square cross-section channel.

6. Increased inlet flow rate results in a higher interfacial shear stress at the liquid-vapor interface, which leads to higher vapor pressure drop. This can be attributed to the higher Reynolds number flow associated with higher inlet flow rate.

7.2 Unique Contributions

The unique contributions of the current work are as follows:

7.2.1 Experimental work on boiling

1. Providing a better understanding of the thermal performance of a thermosyphon at varying sub-atmospheric pressures, enhancement structure geometries and liquid-fill levels.

2. Identifying the presence of optimum geometrical, system and design parameters for improved thermal performance.

3. Demonstration of the effectiveness of system parameters with respect to baseline configuration.

7.2.2 Numerical work on condensation

1. Development of a condensation model, which includes the detailed analysis of the liquid and vapor phases combined through an iterative non-linear approach for obtaining condensate profiles in rectangular microchannels.

2. Demonstration of model validation through comparison with existing correlations and model.

7.3 Recommendations for future work

The current study presents a detailed analysis of boiling under sub-atmospheric pressures for varying conditions of liquid fill levels and boiling enhancement structure geometry. The study on condensation in rectangular microchannels was done for various channel geometries, inlet flow rates and inlet subcooling. However, further studies are required to complement the present study for comprehensive understanding of boiling and condensation in a thermosyphon. The recommended research works are as follows:

7.3.1 Study on boiling

1. A study on the effects of geometrical parameters of the enhancement structure including pore size, pore pitch and thickness of individual layers on the thermal performance of the thermosyphon at sub-atmospheric pressures can provide a more comprehensive understanding and help in the design of an optimized structure.

2. A visualization study on boiling of water at sub-atmospheric pressures will help in understanding the bubble dynamics at low pressures in compact boiling chambers. This will also help in observing the initiation of boiling and also the frequency of bubble generation.

3. The pressure inside the thermosyphon is dependent on the height difference between the boiling surface and the condenser. A study on the effect of height on thermosyphon performance would help in optimizing the size of the thermosyphon for designing a more compact device.

4. Due to the cooling of the vapor in the condenser, the condensed liquid entering the evaporator can be subcooled. In the present study the subcooling was dependent on the heat transfer coefficient achieved in the condenser. However, a lower subcooling might increase the boiling heat transfer coefficient, as most of the heat transfer then will be latent. A subcooling study with water at subatmospheric pressures will complement the present work towards achieving more control on the heat transfer coefficient achieved in the evaporator.

7.3.2 Study on condensation

1. The condensation model can be improved with a better treatment of the corner zones. The current treatment of the corner zone is based on the assumption of one-dimensional flow in the corner zone. A finite volume based numerical

model for the corner zone would be able to accurately simulate the flow field and temperature profile.

2. The current model needs to be extended to solve for condensation in a series of parallel microchannels. In this regard, external air-side simulation needs to be integrated, which will also incorporate varying outside wall temperature of the condenser.

APPENDIX A

UNCERTAINTY CALCULATIONS

The uncertainty of the surface heat flux is calculated in the following way:

$$q'' = \frac{V^2}{RA} \tag{32}$$

where, q'' is the surface heat flux, V is the input voltage to the heater, R is the resistance of the precision resistor placed in parallel connection with the heater in the circuit and A is the surface area of the plain boiling surface. Then following Kline and McClintok [74], the uncertainty of q'' can be written as,

$$\Delta q'' = \left\{ \left(\frac{\partial q''}{\partial V} \Delta V \right)^2 + \left(\frac{\partial q''}{\partial R} \Delta R \right)^2 + \left(\frac{\partial q''}{\partial A} \Delta A \right)^2 \right\}^{\frac{1}{2}} \tag{33}$$

where,

$$\frac{\partial q''}{\partial V} = \frac{2V}{RA} = \frac{2q''}{V} \tag{34}$$

$$\frac{\partial q''}{\partial R} = -\frac{V^2}{R^2 A} = -\frac{q''}{R} \tag{35}$$

$$\frac{\partial q''}{\partial A} = -\frac{V^2}{RA^2} = -\frac{q''}{A} \tag{36}$$

Therefore

$$\Delta q'' = q'' \left\{ 4 \left(\frac{\Delta V}{V} \right)^2 + \left(\frac{\Delta R}{R} \right)^2 + \left(\frac{\Delta A}{A} \right)^2 \right\}^{\frac{1}{2}} \tag{37}$$

The voltage measurement uncertainty is specified by the manufacturer as 0.045%of the reading. The uncertainty in the precision resistor was ± 0.01. The uncertainty in the calculation of the area of the boiling surface was ± 0.1. The uncertainties can be

expressed as:

$$\frac{\Delta V}{V} = 0.00045 \tag{38}$$

$$\frac{\Delta R}{R} = 0.01 \tag{39}$$

$$\frac{\Delta A}{A} = 0.1 \tag{40}$$

Substituting these values in Eq. 37, we get,

$$\frac{\Delta q''}{q''} = \left\{4 \cdot (0.00045)^2 + (0.01)^2 + (0.06)^2\right\}^{\frac{1}{2}} \tag{41}$$

which is equal to 0.10. So the uncertainty in heat flux measurement is 10.0%.

Bibliography

[1] "Executive summary - Overview and working group summaries", 2006 Update, *International Technology Roadmap for Semiconductors*, 2006, pp. 15.

[2] Viswanath, R., Wakharkar, V., Watwe, A. and Lebonheur, V., 2006, "Performance challenges from silicon to systems", *Intel Quarterly Journal, Q3, 2000.*

[3] Pal, A., Joshi, Y., Beitelmal, M. H., Patel, C. D. and Wenger, T., 2002, "Design and performance evaluation of a compact thermosyphon", *IEEE Transactions on Components and Packaging Technologies*, 25(4), pp. 601-607.

[4] Gregorig, R., 1954, "Film Condensation on Finely Rippled Surface With Condensation of Surface Tension", *Zeitschrift Fr Angewandte Mathematik Und Physik*, Vol. 5, pp. 36-49.

[5] Palm, B. and Tengblad, N., 1996, "Cooling of electronics by heat pipes and thermosyphons - A review of methods and possibilities", *National Heat Transfer Conference*, HTD-Vol 329, Volume 7, pp. 97-108.

[6] Tengblad, N. and Palm, B., 1996, "External two phase thermosiphons for cooling of electronic components" *International Journal of Microcircuits and Electronic Packaging*, 19(1), pp. 22-29.

[7] Ramaswamy, C., Joshi, Y., Nakayama, W. and Johnson, W. B., 1998, "Performance of a compact two-phase thermosyphon: Effect of evaporator inclination, liquid fill volume and contact resistance", *Proceedings of the 11th International Heat Transfer Conference, Vol. 2, Kyongju, Korea*, pp. 127-132.

[8] Ramaswamy, C., Joshi, Y., Nakayama, W. and Johnson, W. B., 1999, "Compact thermosyphons employing microfabricated components", *Microscale Thermophysical Engineering*, 3, pp. 273-282.

[9] Nakayama, W., Nakajima, T. and Hirasawa, S., 1984, "Heat sink studs having enhanced boiling surfaces for cooling of microelectronic components", *ASME Paper No. 84-WA/HT-89.*

[10] Ramaswamy, C., Joshi, Y., Nakayama, W. and Johnson, W. B., 1999, "Thermal Performance of a Compact Two-Phase Thermosyphon: Response to Evaporator Confinement and Transient Loads", *Journal of Enhanced Heat Transfer*, 6, pp. 279-288.

[11] Ramaswamy, C., Joshi, Y., Nakayama, W. and Johnson, W. B., 2000, "Combined effects of sub-cooling and operating pressure on the performance of a two-chamber thermosyphon", *IEEE Transactions on Components and Packaging Technologies*, 61-69, March 2000.

[12] Webb, R. L. and Yamauchi, S., 2001, "Thermosyphon concept to cool desktop computers and servers", *Proceedings of the International Electronic Packaging Technical Conference and Exhibition, 2001, Kauai, Hawaii.*

[13] Garner, S. D. and Patel, C. D., 2001, "Loop thermosyphons and their applications to high density electronics cooling", *Proceedings of the International Electronic Packaging Technical Conference and Exhibition, 2001, Kauai, Hawaii.*

[14] Yuan, L., Joshi, Y. K. and Nakayama, W., 2000, "Effect of condenser location and imposed circulation on the performance of a compact two-phase thermosyphon", *Proceedings of the International Conference on Heat Transfer and Transport Phenomena in Microscale, Banff, Canada, 2000*, pp. 304-311.

[15] Yuan, L., Joshi, Y. and Nakayama, W., 2001, "Effect of condenser location and tubing length on the performance of a compact two-phase thermosyphon", *Proceedings of 2001 International Mechanical Engineering Congress and Exposition, ASME, November 11-16, New York, NY.*

[16] Haider, S. I., Joshi, Y. K. and Nakayama, W., 2002, "A natural circulation model of the closed loop, two-phase thermosyphon for electronics cooling", *Journal of Heat Transfer*, 124, pp. 881-890.

[17] Van Stralen, S. J. D., 1956, "Heat transfer to boiling binary liquid mixtures at atmospheric and subatmospheric pressures", *Chemical Engineering Science*, 5, pp. 290-296.

[18] Ponter, A. B. and Haigh, C. P., 1969, "The boiling crisis in saturated and subcooled pool boiling at reduced pressures", *International Journal of Heat and Mass Transfer*, 12, pp. 429-437.

[19] Miyauchi, T. and Yokura, M., 1972, "The mechanism of nucleate boiling heat transfer", *Heat Transfer - Japanese Research*, vol. 1, No. 2, pp. 109-118.

[20] Van Stralen, S. J. D., Cole, R., Sluyter, W. M. and Sohal, M. S., 1975, "Bubble growth rates in nucleate boiling of water at subatmospheric pressures", *International Journal of Heat and Mass Transfer*, 18, pp. 655-669.

[21] Joudi, K. A. and James, D. D., 1977, "Incipient boiling characteristics at atmospheric and subatmospheric pressures", *Journal of Heat Transfer*, 99, pp. 398-403.

[22] Fath, H. S. and Judd, R. L., 1978, "Influence of system pressureon microlayer evaporation heat transfer", *Journal of Heat Transfer*, 100, pp. 49-55.

[23] Latsch, K., Morell, F. and Rampf, H., 1978, "Subcooled forced convection boiling heat transfer at substmospheric pressure", *Proceedings of the Sixth International Heat Transfer Conference*, pp. 287-292.

[24] Tewari, P. K., Verma, R. K., Ramani, M. P. S., Chatterjee, A. and Mahajan, S. P., 1989, "Nucleate boiling in a thin film on a horizontal tube at atmospheric and subatmospheric pressures", *International Journal of Heat and Mass Transfer*, 32(4), pp. 723-728.

[25] McGillis, W. R., Carey, V. P., Fitch, J. S. and Hamburgen, W. R., 1991, "Pool boiling enhancement techniques for water at low pressure", *Proceedings of the Seventh IEEE SEMI-THERM Symposium*, pp. 64-72.

[26] Rainey, K. N., You, S. M. and Lee, S., 2003, "Effect of pressure, subcooling and

dissolved gas on pool boiling heat transfer from microporous surfaces in FC-72", *Journal of Heat Transfer*, 125, pp. 75-83.

[27] Nakayama, W., Daikoku, T., Kuwahara, H. and Nakajima, T., 1980, "Dynamic model of enhanced boiling heat transfer on porous surfaces, Part I: Experimental Investigation", *Journal of Heat Transfer*, 102, pp. 445-450.

[28] Oktay, S., 1982, "Departure from natural convection (DNC) in low-temperature boiling heat transfer encountered in cooling micro-electronic LSI devices", *Heat Transfer - 1982*, vol. 4, pp. 113-118.

[29] Bergles, A. E. and Chyu, M. C., 1982, "Characteristics of nucleate pool boiling from porous metallic coatings", *Journal of Heat Transfer*, 104, pp. 279-285.

[30] Marto, P. J. and Lepere, V. J., 1982, "Pool boiling heat transfer from enhanced surfaces to dielectric fluids", *Journal of Heat Transfer*, 104, pp. 292-299.

[31] Anderson, T. M. and Mudawar, I., 1989, "Microelectronic cooling by enhanced pool boiling of a dielectric fluorocarbon liquid", *Journal of Heat Transfer*, 111, pp. 752-759.

[32] Nowell, R. M., Bhavnani, S. H. and Jaeger, R. C., 1995, "Effect of channel width on pool boiling from a microconfigured heat sink", *IEEE Transactions on Components, Packaging and Manufacturing Technology-Part A, Vol. 18, No.3*, pp. 534-539.

[33] Ramaswamy, C., Joshi, Y., Nakayama, W. and Johnson, W. B., 2003, "Effects of varying geometrical parameters on boiling from microfabricated enhanced structures", *Journal of Heat Transfer*, 125, pp. 103-109.

[34] Abou-Ziyan, H. Z., Helali, A., Fatouh, M. and Abo El-Nasr, M. M., 2001, "Performance of stationary and vibrated thermosyphon working with water and R134a", Applied Thermal Engineering, 21, pp. 813-830.

[35] Zuo, Z. J., North, M. T. and Wert, K. L., 2001, "High heat flux heat pipe mechanism for cooling of electronics", IEEE Transactions of Components abd Packaging Technologies, June 2001, 24 (2), pp. 220-225.

[36] Ong, K. S. and Haider-E-Alahi, Md., 2003, "Performance of a R-134a filled thermosyphon", Applied Thermal Engineering, 23, pp. 2373-2381.

[37] Park, Y. J., Kang, H. K. and Kim, C. J., 2002, "Heat transfer characteristics of a two-phase closed thermosyphon to the fill charge ratio", International Journal of Heat and Mass Transfer, 45, pp. 4655-4661.

[38] Carey, V. P., "Pool Boiling", *Liquid-vapor phase change phenomenon*, Hemisphere Publishing Corporation, New York, NY, February, 1992, pp. 250.

[39] Rose, J. W., 2004, "Surface tension effects and enhancement of condensation heat transfer", *Transactions of the IChemE, Part A, Chemical Engineering Research and Design*, 82(A4), pp. 419-429.

[40] Koh, J. C. Y., Sparrow, E. M. and Hartnett, J. P., 1961, "The two-phase boundary layer in laminar film condensation", *International Journal of Heat*

and Mass Transfer, vol. 2, pp. 69-82.

[41] Liao, N. S. and Wang, C. C., 1990, "Transient response characteristics of two-phase condensing flows", *International Journal of Heat and Mass Transfer*, 16(1), pp. 139-151.

[42] Yao, G. F., Ghiaasiaan, S. M. and Eghbali, D. A., 1996, "Semi-implicit modeling of condensation in the presence of non-condensables in the RELAP5/MOD3 computer code", *Nuclear Engineering and Design*, 166, pp. 277-291.

[43] Mitrovic, J., 2000, "Effects of vapor superheat and condensate subcooling on laminar film condensation", *ASME Journal of Heat Transfer*, 122, pp. 192-196.

[44] Chitti, M. S. and Anand, N. K., 1995, "An analytical model for local heat transfer coefficients for forced convective condensation inside smooth horizontal tubes", *International Journal of Heat and Mass Transfer*, 38(4), pp. 615-627.

[45] Hirasawa, S., Hijikata, K., Mori, Y. and Nakayama, W., 1980, "Effect of surface tension on condensate motion in laminar film condensation (study of liquid film in small trough)", *International Journal of Heat and Mass Transfer*, vol. 23, pp. 1471-1478.

[46] Suzuki, K., Hagiwara, Y. and Izumi, H., 1990, "A numerical study of forced-convective filmwise condenstion in a vertical tube", *JSME International Journal, Series II*, 33(1), pp. 134-141.

[47] Shekriladze, I. J. and Gomelauri, V. I., 1966, Theoretical study of laminar film condensation of flowing vapor", *International Journal of Heat and Mass Transfer*, 9, pp. 581-589.

[48] Wang, B.-X. and Du, X.-Z., 2000, "Study on laminar film-wise condensation for vapor flow in an inclined small/mini-diameter tube", *International Journal of Heat and Mass Transfer*, 43, pp. 1859-1868.

[49] Chiou, J.-S., Yang, S.-A. and Chen, C.-K., 1994, "Laminar film condensation inside a horizontal elliptical tube", *Applied Mathematical Modelling*, vol. 18, June, pp. 340-346.

[50] Guo, Z. and Anand, N. K., 2000, "An analytical model to predict condensation of R-410A in a horizontal rectangular channel", *ASME Journal of Heat Transfer*, 122, pp. 613-620.

[51] Riehl, R. R., Ochterbeck, J. M. and Seleghim Jr, P., 2002, "Effects of condensation in microchannels with a porous boundary: analytical investigation on heat transfer and meniscus shape", *Journal of the Brazilian Society of Mechanical Sciences*, 24(3), pp. 186-194.

[52] Zhao, T. S. and Liao, Q., 2002, "Theoretical analysis of film condensation heat transfer inside vertical mini triangular channels", *International Journal of Heat and Mass Transfer*, 45, pp. 2829-2842.

[53] Wang, H. S., Rose, J. W. and Honda, H., 2004, "A theoretical model of film condensation in square section horizontal microchannels", *Transactions of the*

IChemE, Part A, Chemical Engineering Research and Design, 82(A4), pp. 430-434.

[54] Wang, H. S. and Rose, J. W., 2004, "Film condensation in horizontal triangular section microchannels: A theoretical model", *Proceedings of the 2nd International Conference on Microchannels and Minichannels, ICMM2004, June 17-19, 2004, Rochester, New York, USA*, pp. 661-666.

[55] Wang, H. S. and Rose, J. W., 2005, "Film condensation in horizontal microchannels: Effect of channel shape", *Proceedings of the 3rd International Conference on Microchannels and Minichannels, ICMM2005, June 13-15, 2005, Toronto, Ontario, Canada.*

[56] Launay, S., Federov, A., Joshi, Y., Cao, A. and Ajayan, P. M., "Hybrid micro-nano structured thermal interfaces for pool boiling heat transfer enhancement", *Proceedings of THERMINIC 2004*, Sophia Antipolis, Cote d'Azur, France, Sep 29-Oct 1, 2004, 2004, pp. 299-304.

[57] Gebhart, B. and Wright N., "Boiling enhancement of microconfigured surfaces", *International Communications of Heat and Mass Transfer*, 15, 1988, pp. 141-149.

[58] Wright, N. and Gebhart, B, "Enhanced boiling on microconfigured surfaces", *Journal of Electronic Packaging*, 111, 1989, pp. 112-120.

[59] Gorodov, A. K., Kaban'kov, O. N., Komov, A. T. and Yagov, V. V., 1979, "Critical boiling heat fluxes to liquids at subatmospheric pressures", *Heat Transfer - Soviet Research*, 11(3), May-June, 53-61.

[60] Pal, A. and Joshi, Y., 2006, "Boiling of water at sub-atmospheric conditions with enhanced structures - effect of liquid fill volume", *Proceedings of the IMECE 2006*, November 5-10, Chicago, Illinois, USA, 2006.

[61] Lienhard, J. H. and Dhir, V. K., 1973, "Extended hydrodynamic theory of the peak and minimum pool boiling heat fluxes", *NASA CR-2270, July 1973.*

[62] Ramaswamy, C., "A compact two-phase thermosyphon employing microfabricated boiling enhancement structures", *Ph.D. Dissertation*, University of Maryland, College Park, 1999.

[63] Nakayama, W., Daikoku, T. and Nakajima, T., "Effects of pore diameter and system pressure on saturated pool nucleate boiling heat transfer from porous surfaces", *Journal of Heat Transfer*, 104, 1982, pp. 286-291.

[64] Ghiu, C.-D. and Joshi, Y., 2005, "Boiling performance of single-layered enhanced structures", *Journal of Heat Transfer*, 127, 675-683.

[65] Nusselt, W., 1916, "Die Oberflachenkondensation des Wasserdampfes", *Z. Vereins Deutsch. Ing.*, 60, pp. 541-557.

[66] Faghri, A., 1995, "Heat Pipe Science and Technology", *Taylor and Francis, Washington, D.C.*.

[67] Stephan, P. C. and Busse, C. A., 1992, "Analysis of the heat transfer coefficient of grooved pipe evaporator walls", *International Journal of Heat and Mass*

Transfer, 35(2), pp. 383-391.

[68] Rosson, H. F. and Meyers, J. A, 1965, "Point values of condensing film coefficients inside a horizontal tube", *Chem. Eng. Prog. Symp. Ser.*, Vol. 3, pp. 304-308.

[69] Shah, M. M., 1989, "A general correlation for heat transfer during film condensation inside pipes", *International Journal of Heat and Mass Transfer*, 22, pp. 547-556.

[70] Garimella, S. and Bandhauer, T. M., 2001, "Measurement of condensation heat transfer coefficients in microchannel tubes", *2001 ASME International Mechanical Engineering Congress and Exposition, November 11-16, New York, NY.*

[71] Shin, J. S. and Kim, M. H., 2004, "An experimental study of flow condenation heat transfer inside circular and rectangular mini-channels", *Second International Conference on Microchanels and Minichannels, ICMM2004, June 17-19, 2004, Rochester, New York, NY*, pp. 633-640.

[72] Cavallini, A., Del Col, D., Doretti, L., Matkovic, M., Rossetto, L. and Zilio, C., 2004, "Condensation heat transfer inside multi-port multichannels", *Second International Conference on Microchanels and Minichannels, ICMM2004, June 17-19, 2004, Rochester, New York, NY*, pp. 625-632.

[73] Lu, Q. and Suryanarayana, N. V., 1995, "Condensation of a vapor flowing inside a horizontal rectangular duct", *ASME Journal of Heat Transfer*, 117, pp. 418-424.

[74] Kline, S. J. and McClintock, F. A., 1953, "Describing Uncertainties in Single-Sample Experiments", *Mechanical Engineering*, 1, pp. 3-8.